

UNIVERSIDADE DE SÃO PAULO
FACULDADE DE ZOOTECNIA E ENGENHARIA DE ALIMENTOS

GONZALO MÁRMOL DE LOS DOLORES

**Low-alkalinity matrix composites based on magnesium oxide cement
reinforced with cellulose fibres**

Pirassununga

2017

GONZALO MÁRMOL DE LOS DOLORES

**Low-alkalinity matrix composites based on magnesium oxide cement
reinforced with cellulose fibres**

Corrected Version

Thesis presented to obtain the degree of Doctor of Science.

Área: Development, Characterization and Application of Materials for Agribusiness.

Supervisor: Holmer Savastano Junior

Pirassununga

2017

Ficha catalográfica elaborada pelo
Serviço de Biblioteca e Informação, FZEA/USP, com os
dados fornecidos pelo(a) autor(a)

M3511 Mármol, Gonzalo
Low-alkalinity matrix composites based on
magnesium oxide cement reinforced with cellulose
fibers / Gonzalo Mármol ; orientador Holmer
Savastano Junior. -- Pirassununga, 2017.
160 f.

Tese (Doutorado - Programa de Pós-Graduação em
Engenharia e Ciência de Materiais) -- Faculdade de
Zootecnia e Engenharia de Alimentos, Universidade
de São Paulo.

1. MgO-SiO₂ binder. 2. low-alkalinity
cementitious composite. 3. cellulose. 4.
durability. 5. carbonation. I. Savastano Junior,
Holmer, orient. II. Título.

DEDICATION

Andar
de chinelo. Garoa.
Partiu. Açai na tigela.
Carona. Já viu? A turma. Mangueira. Arara. Pois não. Ladrão! Pão
de queijo. Engraçado. Fechou. Carioca. Mineiro. Baiano. Paulista.
Sobrado. Altas ondas. Pessoa. Está certo. Valeu. Cachoeira. Passeio de
bike. Meu filho. Você. Laranjinha. Ipê. Pelada no Metze. Corrida a pé. Vinicius e
Tom. Busão. Pesquisa. Igreja. Minha magrela. Tucano. O lab. Gramado. Rodoviária.
Quintal. Churras. Escondidinho. Cervejada. Chuveiro. Cheiro. Feijoada. As vacas e os bois. Nós dois.
Saudade. Beleza. Natureza. A praia. O mato. Carnaval. Tiradentes. Pantanal. Acerola. Fruta do conde. Vixe!
Maria. Forró. Duque de Caxias. Caldo de cana. Tomara. Amazônia. Imagina! Abacate. Vitamina. Bolo de fubá. Pagode. A Copa.
Caipirinha. Balada. Varal. Vaquinha. Trilha. XV de novembro. Paraty e Ubatuba. Anhanguera. Rua do Porto. Capivara. Bar da
Maria. Coxinha de frango. Maracujá. Pipoca. Favela. Café da manhã. Sinuca. Vôlei de areia. Copa Cabana. Pão de açúcar. Pão de
mel. Cerrado. Salgado. Bandeirão! Coração. O gado. Resistência a flexão. Testado. Os colegas: parceiros. Verão em janeiro.
Águas de março. Samba. Queijo mineiro. Sertanejo. Iguaçu. Luz. Orla do Guaíba. CNPq. Aniversário. O som. Jeitinho. Meu
Deus. Quadra ou campo? Constrambi. Funcionário. Motorista. Microscopia. Alojamento.
Canto coral. Florianópolis. Cananeia. Mormaço. Bloco dos
Sujos. Edison. Legal. Canarinha. Goiaba. Cochilada. Garoto ou rapaz.
Vai em paz. Sossegado. Joia. Espetinho. Sanfona. Grato. Aedis aegypty.
Batuque. Dendrogeomorfologia. Rua. Festa junina. Celulose.
Pernambuco com o violão. Criança. Rua. Alcatra e maminha. Raio
e trovão. Brigadeiro. Caipira na roça. Água de coco. Calcanhar.
Chuva. Torneira. Caixa postal. Carteirinha. Tapioca. Sol. Gaúcho.
Palmeira. Vinagrete e maionese com pão francês. Guarulhos.
Independência. Vovó de camarão. Skype e família. Final
de semana. Nordeste. Piracicaba. Segunda-feira. Força
aérea. Pirassununga. Garças no campus. Sorvete. Café de
meia suja. Saúde. Jequitibá. Minha menininha.. Feriado.
Quarteirão. Bandinha. Capoeira. Irmão. Jura?
Certeza. Chimarrão. Bomba e cuja.
Sabonete. Amizade. Amor.
Acarajé. Floresta.
Compromisso.
Mistura. Memória
Expressão. Floresta.
Que foi?. Amor. Nossa
Senhora. Eterno. Olá.
Gratidão. Sim.
Tchau!

Brasil

Muito obrigado. Des res. Hasta siempre.

ABSTRACT

MÁRMOL, G. **Low-alkalinity matrix composites based on magnesium oxide cement reinforced with cellulose fibers.** 2017. 160 p. Thesis (Doctorate) - Faculdade de Zootecnia e Engenharia de Alimentos, Universidade de São Paulo, Pirassununga, 2017.

A lower-alkalinity cement based on MgO and SiO₂ blends is analysed to develop clinker-free Fibre Reinforced Cementitious Composites (FRCC) with cellulosic fibres in order to solve the durability problems of this type of fibres when used in FRCC with Portland cement. Hydration evolution from 7 to 28 days of different MgO-SiO₂ formulations is assessed. The main hydration products are Mg(OH)₂ and M-S-H gels for all the formulations studied regardless of age. Hardened pastes are obtained with pH values < 11 and good mechanical properties compared to conventional Portland cement. 60% MgO-40% SiO₂ system is chosen as optimal for the development FRCC since is the most mechanical resistant and is less alkaline compared with 70% MgO-30% SiO₂. FRCC based on magnesium oxide and silica (MgO-SiO₂) cement with cellulose fibres are produced to study the durability of lignocellulosic fibres in a lower pH environment than the ordinary Portland cement (PC). Flexural performance and physical tests (apparent porosity, bulk density and water absorption) of samples at 28 days and after 200 accelerated ageing cycles (aac) are compared. Two types of vegetable fibres are utilised: eucalyptus and pine pulps. MgO-SiO₂ cement preserves cellulosic fibres integrity after ageing, so composites made out of MgO-SiO₂ exhibit significant higher performance after 200 cycles of accelerated ageing than Portland cement composites. High CO₂ concentration environment is evaluated as a curing treatment in order to optimise MgO- SiO₂ matrices in FRCC. Samples are cured under two different conditions: 1) steam water curing at 55°C and 2) a complementary high CO₂ concentration (20% by volume). In carbonated samples, Mg(OH)₂ content is clearly lowered while new crystals of hydromagnesite [Mg₅(CO₃)₄·(OH)₂·4H₂O] are produced. After carbonation, M-S-H gel content is also reduced, suggesting that this phase is also carbonated. Carbonation affects positively to the composite mechanical strength and physical properties with no deleterious effects after ageing since it increases matrix rigidity. The addition of sepiolite in FRCC is studied as a possible additive constituent of the binding matrix. Small cement replacement (1 and 2% wt.) by sepiolite is introduced and studied in hardened cement pastes and, later, in FRCC systems. When used only in cement pastes, it improves Dynamic Modulus of Elasticity over time. Bending tests prove the outcome of this additive on the mechanical performance of the composite: it improves composite homogeneity. Ageing effects are reported after embedding sisal fibres in MgO-SiO₂ and PC systems and submitting them to different ageing conditions. This comparative study of fibre degradation applied in different cementitious

matrices reveals the real compatibility of lignocellulosic fibres and Mg-based cements. Sisal fibres, even after accelerated ageing, do neither suffer a significant reduction in cellulose content nor in cellulose crystallinity and crystallite size, when exposed to MgO-SiO₂ cement. Fibre integrity is preserved and no deposition of cement phases is produced in MgO-SiO₂ environment.

Keywords: MgO-SiO₂ binder; Low-alkalinity cementitious composite; Cellulose; Durability; Carbonation.

RESUMO

MÁRMOL, G. **Compósitos de baixa alcalinidade à base de óxido de magnésio reforçados com fibras de celulose**. 2017. 160 p. Tese (Doutorado) - Faculdade de Zootecnia e Engenharia de Alimentos, Universidade de São Paulo, Pirassununga, 2017.

Um cimento de baixa alcalinidade à base de blendas de MgO e SiO₂ é analisado para o desenvolvimento de Compósitos Cimentícios Reforçados com Fibras (CCRF) celulósicas sem clínquer para resolver os problemas de durabilidade de este tipo de fibras quando são usadas em CCRF com cimento Portland. A evolução da hidratação, desde 7 aos 28 dias, das diferentes formulações é avaliada. Os principais produtos hidratados são o Mg(OH)₂ e o gel M-S-H para todas as formulações independentemente da idade estudada. As pastas endurecidas apresentam valores de pH < 11 e bom desempenho mecânico comparado com o cimento Portland convencional. O sistema 60% MgO-40% SiO₂ é escolhido como a formulação ótima para o desenvolvimento de CCRF já que é a mais resistente e menos alcalina comparada com 70% MgO-30% SiO₂. CCRF com cimento à base de óxido de magnésio e sílica (MgO-SiO₂) e fibras celulósicas são produzidos para a análise da durabilidade das fibras lignocelulósicas em ambientes com valores de pH mais baixos comparados com o cimento Portland (PC). O desempenho mecânico a flexão e os ensaios físicos (porosidade aparente, densidade aparente e absorção de água) são comparados aos 28 dias e após de 200 ciclos de envelhecimento acelerado. O cimento à base de MgO-SiO₂ preserva a integridade das fibras após o envelhecimento. Os compósitos produzidos com este cimento exibem melhores propriedades após 200 ciclos de envelhecimento acelerado que os compósitos produzidos com cimento Portland. Ambientes com alta concentração de CO₂ são avaliados como tratamento de cura para otimizar as matrizes MgO- SiO₂ nos CCRF. As amostras são curadas sob 2 condições diferenciadas: 1) cura com vapor de água a 55°C e 2) cura com alta concentração de CO₂ (20% do volume). As amostras carbonatadas apresentam teores reduzidos de Mg(OH)₂ enquanto é produzida uma nova fase cristalina: hidromagnesita [Mg₅(CO₃)₄·(OH)₂·4H₂O]. Após a carbonatação, o conteúdo de gel M-S-H é reduzido também, indicando uma carbonatação desta fase. A carbonatação aumenta a rigidez da matriz o que influi positivamente no desempenho mecânico e as propriedades físicas dos compósitos sem efeitos prejudiciais ao longo prazo. A adição de sepiolita em CCRF é estudada como possível adição na composição da matriz aglomerante. Baixos teores (1 e 2% em massa) de cimento são substituídos por sepiolita para o estudo das pastas de cimento hidratado e, posteriormente, dos compósitos. O Módulo Elástico Dinâmico das pastas é incrementado com o tempo pela adição de sepiolita. Os ensaios a flexão demonstram que a adição de sepiolita melhora a homogeneidade dos compósitos. Reportam-se os efeitos das fibras de sisal após da exposição a sistemas

MgO-SiO₂ e PC e submetidas a diferentes condições de envelhecimento. Este estudo comparativo da degradação das fibras expostas a diferentes matrizes cimentícias mostra a compatibilidade das fibras lignocelulósicas com os cimentos à base de Mg. As fibras de sisal, inclusive após o envelhecimento acelerado, não apresentam nem redução significativa no conteúdo de celulose nem na cristalinidade da celulose assim como do tamanho de cristalito, quando expostas a cimentos MgO-SiO₂.

Palavras-chave: Cimento MgO-SiO₂; Compósitos cimentícios de baixa alcalinidade; Celulose; Durabilidade; Carbonatação.

LIST OF FIGURES

Figure 1- Schematic cross section (a) and representation of the structure (b) of a sisal fibre	23
Figure 2- Schematic representation of a cross section of any composite reinforced with an indeterminate fibre	25
Figure 3- Schematic representation of the mechanisms of degradation of a sisal fibre	27
Figure 4- Schematic representation of alkaline hydrolysis on sisal fibre	27
Figure 5- Diagram of a pozzolanic reaction in conventional Portland cement	32
Figure 6- Diagram of the process for magnesium oxide production according to (LACKNER et al., 1995).....	40
Figure 7- Summarized process of $MgCO_3$ production according to (VLASOPOULOS; BERNEBEU, 2014).....	41
Figure 8- Scheme of laboratory scale of DPM process. (a) slurry stirring, mixture of cement, fibres and aggregates in water; (b) transfer to a moulding chamber; (c) composite casting; (d) dewatering by vacuum and tamping by low hydraulic pressing ; (e) finished upper surface and (f) composite compaction by high hydraulic pressing	43
Figure 9- Flowchart representing the workflow of the thesis according the work carried out in the different chapters.....	45
Figure 10- Histogram of the length (a) and width (b) distribution for both types of pulp reinforcement. Grey bars stand for pine and black bars stand for eucalyptus	59
Figure 11- Curing conditions diagram for non-carbonated and carbonated samples.....	63
Figure 12- XRD diffractograms of the different $MgO-SiO_2$ samples at 7 days (left) and at 28 days (right). Peaks marked are brucite (■), periclase (○), calcite (C) and magnesite (M).....	72
Figure 13- Enlarged view of the XRD spectra of the regions where gel bumps are present	73
Figure 14- TG and DTG graphs of the hydrated MgO (AR200) and M-S-H gel with a 0.5 Mg/Si ratio	74
Figure 15- TG (left) and DTG (right) graphs of the of the different $MgO-SiO_2$ samples at 7 days and at 28 days.....	75
Figure 16- FT-IR spectra of the different $MgO-SiO_2$ and 100% MgO samples at 7 days (left) and at 28 days (right).....	77
Figure 17- Mass fraction distribution of all the components of $MgO-SiO_2$ pastes, determined from different tests results	79
Figure 18- (a) SEM image of the polished surface of a 60% MgO – 40% SiO_2 paste at 28 days. (b) Treated SEM image of a 60% MgO - 40% SiO_2 at 28 days. Yellow particles are $Mg(OH)_2$, blue regions are M-S-H gels and white particles are unreacted SiO_2	80
Figure 19- pH evolution over time of different $MgO-SiO_2$ blended systems and control samples (100% Portland cement).....	81
Figure 20- Compressive axial strength of different $MgO-SiO_2$ pastes and control samples (100% Portland cement) at 7 and 28 days	82
Figure 21- (a) Trends in double Y-axis of the compressive axial strength (left axis) and free water content (right axis). (b) Trends in double Y-axis of the compressive axial strength (left axis) and total hydrated phases content (right axis)	84
Figure 22- Trends in double Y-axis of the compressive axial strength (left axis) and Mg/Si ratio (right axis).....	85

Figure 23- Tension-deflection curves of the composites reinforced with pine (a) and eucalyptus (b) pulps for both types of binders, MgO-SiO ₂ (MS) and Portland (OPC), at 28 days and after 200 cycles of accelerated ageing.....	87
Figure 24- Average values of modulus of elasticity (MOE) vs. apparent porosity (AP) of samples at 28 days and after 200 accelerated ageing cycles for both types of cement: MgO-SiO ₂ (MS) and Portland cement (OPC). Horizontal and vertical lines indicate the standard deviation of every sample	91
Figure 25- SEM images of polished surfaces of a composite made out of Portland cement and reinforced with eucalyptus microfibres after 200 cycles of accelerated ageing. In (a), white dashed lines encircle microfibres with the lumen filled with hydration products. Black square stands for a zoomed region depicted in (b). (b) represents a zoomed region of (a), where the lumens of the fibres are clearly mineralized and filled with hydration products after 200 cycles of accelerated ageing	93
Figure 26- EDS mapping of a composite made out of Portland cement and reinforced with eucalyptus (a) and pine (b) microfibres after 200 cycles of accelerated ageing. Green dots represent Ca mapping. Blue dots represent Si mapping.....	93
Figure 27- SEM image of a polished surface of a composite made out of Portland cement and reinforced with pine microfibres after 200 cycles of accelerated ageing. In (a), white dashed lines encircle microfibres surrounded by hydration products. Black square stands for a zoomed region depicted in (b). (b) represents a zoomed region of (a), where black arrows are pointing to the fibre-matrix interface where higher concentrations of Ca(OH) ₂ are present (light grey areas surrounding the fibres) after 200 cycles of accelerated ageing.....	94
Figure 28- SEM images of polished surfaces of composites made out of MgO-SiO ₂ cement and reinforced with pine microfibres at 28 days (a) and after 200 accelerated ageing cycles (b) and eucalyptus microfibres at 28 days (c) and after 200 accelerated ageing cycles (d). White dashed lines encircle brucite crystals. Black arrows point to debonded regions of fibre-matrix interface	95
Figure 29- Surface of fracture of composites made out of MgO-SiO ₂ cement and reinforced with pine microfibres at 28 days (a) and after 200 accelerated ageing cycles (b) and eucalyptus microfibres at 28 days (c) and after 200 accelerated ageing cycles (d). Black arrows point to the fibre-matrix interface	96
Figure 30- SEM image of a polished surface of a composite made out of MgO-SiO ₂ cement and reinforced with pine (a) and eucalyptus (b) microfibres.....	97
Figure 31- XRD diffractograms of the different formulations studied: Uncarbonated-Unaged (NC+NA), Uncarbonated-Aged (NC+A), Carbonated-Unaged (C+NA) and Carbonated-Aged (C+A). Peaks marked are brucite (B), calcite (C), quartz (Q), Dolomite (D) and hydromagnesite (H). Smaller peaks are not marked since they correspond to traces of reinforcing elements.....	98
Figure 32- XRD diffractograms of the different formulations studied: Uncarbonated-Unaged (NC+NA), Uncarbonated-Aged (NC+A), Carbonated-Unaged (C+NA) and Carbonated-Aged (C+A) for the regions where broad bumps due to M-S-H gels are expected to appear. Dotted curves in black represent the gel bumps.....	99
Figure 33- TG curves of the different formulations studied: Uncarbonated-Unaged (NC+NA), Uncarbonated-Aged (NC+A), Carbonated-Unaged (C+NA) and Carbonated-Aged (C+A)	101

Figure 34- DTG curves of the different formulations studied: Uncarbonated-Unaged (NC+NA), Uncarbonated-Aged (NC+A), Carbonated-Unaged (C+NA) and Carbonated-Aged (C+A)	102
Figure 35- (a) is a SEM of a fractured surface of uncarbonated samples. The white dashed line square is the zoomed area depicted in (b). MH, L and PP stand for Mg(OH) ₂ , limestone and polypropylene respectively. The white dashed lines show M-S-H gels. All images are for aged composites after accelerated aging test	103
Figure 36- (a) SEM of a fractured surface of carbonated samples. The white dashed line squares the zoomed are depicted in (b). The white dashed lines show crystals produced after M-S-H carbonation. The yellow dashed line is the zoomed area depicted in (c), exhibiting hydromagnesite crystals. All images are for aged composites after accelerated aging test.....	104
Figure 37- SEM image of a polished surface of a Carbonated composite after accelerated ageing with the different analyzed spectra. In (a), white dashed lines encircle zoomed in (b). (b) represents a zoomed region of (a), where different types of M-S-H gels are shown.....	105
Figure 38- SEM image of a polished surface of a Non-carbonated composite after accelerated ageing with the different analyzed spectra.....	106
Figure 39- DTG peak analysis of carbonated samples after ageing (C+A) and non-aged (C+NA) on the specific regions where HMC dehydration and decarbonation occur	108
Figure 40- Evolution of hydrated pastes Dynamic Flexural Young Modulus over time with a steam curing at 55oC depending on the sepiolite replacement. 0% stands for MgO-SiO ₂ samples with no sepiolite replacement. PC stands for PC cement samples used as a control samples. The rest of the samples indicate the percentage and type of sepiolite replacement.	114
Figure 41- TG and DTG results of the hydrated pastes depending on the type of sepiolite addition used: (a) CIMSIL (b) PANGEL. 0% stands for MgO-SiO ₂ samples with no sepiolite replacement. The rest of the samples indicate the percentage and type of sepiolite replacement	116
Figure 42- XRD diffractograms of the hydrated pastes depending on the type of sepiolite addition used: (a) CIMSIL (b) PANGEL. 0% stands for MgO-SiO ₂ samples with no sepiolite replacement. The rest of the samples indicate the percentage and type of sepiolite replacement	116
Figure 43- SEM images of hydrated MgO-SiO ₂ systems without sepiolite addition (a), with 1% of CIMSIL sepiolite (b), with 1% PANGEL sepiolite and 2% PANGEL sepiolite.....	117
Figure 44- Evolution of the mean chord size of 18.4 g of powder suspensions in 400 mL of water according to Table 11. Flocculation evolution is displayed in (a) for MgO-SiO ₂ powder is displayed with and without filler addition, in (b) for MgO-SiO ₂ powder with filler addition and undelaminated sepiolite replacements, in (c) for MgO-SiO ₂ powder with filler addition and delaminated sepiolite replacements, (d) for PC is displayed with and without filler addition, in (e) for PC with filler addition and undelaminated sepiolite replacements and in (f) for PC with filler addition and delaminated sepiolite replacements	118
Figure 45- Evolution of the mean chord size of 18.4 g of powder + 1.6 g of pine pulp suspensions in 400 mL of water according to Table 11. Flocculation evolution is displayed in (a) in for MgO-SiO ₂ powder with filler addition, undelaminated sepiolite replacements and cellulose pupl , in (b) for MgO-SiO ₂ powder with filler addition and delaminated sepiolite replacements and cellulose pulp, in (c) for PC with filler addition, undelaminated sepiolite replacements and cellulose pulp and in (d) for PC with filler addition, delaminated sepiolite replacements and cellulose pulp...	120
Figure 46- Drainage curves displayed by the different fibre–cement slurries: (a) using MgO-SiO ₂ powder and (b) using Ordinary Portland cement (PC)	121

Figure 47- Stress-deflection curves of the most representative sample of each composite composition. 0% stands for MgO-SiO ₂ samples with no sepiolite replacement. PC stands for PC cement samples used as a control samples. The rest of the samples indicate the percentage and type of sepiolite replacement	124
Figure 48- SEM images of the surroundings of reinforcing fibres for each composition with sepiolite: (a) CIMSIL 1%, (b) CIMSIL 2%, (c) PANGEL 1% and (d) PANGEL 2%.....	125
Figure 49- TG/DTG thermograms of sisal fibres both unaged and aged, both in MgO-SiO ₂ (MS) and Portland cement (PC), for 5 months. Circles match the different peaks obtained in DTG curves	127
Figure 50- TG/DTG thermograms of MgO-SiO ₂ (MS) and Portland cement (PC) after 5 months	129
Figure 51- TG/DTG thermograms of sisal fibres both unaged and after 400 accelerated ageing cycles in, both MgO-SiO ₂ (MS) and Portland cement (PC). Circles match the different peaks obtained in DTG curves	129
Figure 52- Mass loss of each component of sisal fibres both unaged and after ageing (5 months and 400 accelerated ageing cycles) in MgO-SiO ₂ (MS) and Portland cement (PC). Circles match the different peaks obtained in DTG curves.....	130
Figure 53- Quadruple axis diagram with activation energy results according to the different methods used in thermograms (left axis) and mass loss fraction of cellulose and holo-cellulose (right axis).....	131
Figure 54- X-ray diffraction patterns of untreated and aged sisal fibres, after 5 months and 400 accelerated ageing cycles, in both MgO-SiO ₂ (MS) and Portland cement (PC)	132
Figure 55- DSC curves of sisal fibres both unaged and after 5 months ageing and 400 accelerated ageing cycles in both MgO-SiO ₂ (MS) and Portland cement (PC)	134
Figure 56- SEM images of sisal fibres embedded in epoxy resin after ageing. (a) 5 months in MgO-SiO ₂ aged fibre backscattered secondary electrons (BSE) SEM, (b) 5 months in PC aged fibre BSE SEM, (c) enlarged view of sisal fibre in the same conditions as (b), (d) unaged fibre BSE SEM, (e) 400 aac in PC aged fibre BSE SEM and (f) SEM image from (c).....	136
Figure 57- SEM images and EDS mapping of sisal fibres embedded in epoxy resin at different ageing times exposed to PC. (a) SEM of samples after 5 months in PC, (b) EDS mapping of samples after 5 months in PC, (c) SEM of samples after 400 accelerated ageing cycles in PC and (d) EDS mapping of samples after 400 accelerated ageing cycles in PC	138
Figure 58- SEM images and EDS mapping of sisal fibres embedded in epoxy resin at different ageing times exposed to MgO-SiO ₂ cement. (a) SEM of samples after 5 months in MgO-SiO ₂ cement, (b) EDS mapping of samples after 5 months in MgO-SiO ₂ cement, (c) SEM of samples after 400 accelerated ageing cycles in MgO-SiO ₂ cement and (d) EDS mapping of samples after 400 accelerated ageing cycles in MgO-SiO ₂ cement	139

LIST OF TABLES

Table 1- Mechanical properties of different fibres used in composites application.	21
Table 2-Advantages and disadvantages of using cellulosic-based fibres as reinforcement in FRCC.	22
Table 3- Properties of the raw materials used to produce the blended samples.....	55
Table 4- Different MgO and SiO ₂ blends analysed in this block.....	55
Table 5- Chemical characterization and particle size parameters of the raw materials used for the matrix formulation of the composites.	58
Table 6- Chemical composition of the cellulosic pulps.	58
Table 7- Formulation of the FRCC samples used in Block 2 tests.....	59
Table 8- Water to matrix ratio and water to binder ratio after pressing process of every formulation for both types of reinforcement.	60
Table 9- Formulation of the FRCC samples used in Block 3 tests.....	62
Table 10- Properties of the two types of sepiolite used in the study: CIMSIL and PANGEL	64
Table 11- Composition of the suspensions used for the assessment of fibre-cement flocculation.	66
Table 12- Method to assess pure powder and fibre-cement suspensions flocculation: adding sequence and stirring rate variations (meeting the process used by Fuente et al. (FUENTE et al., 2010))......	67
Table 13- Weight loss according to TG results of the different MgO-SiO ₂ samples at different temperatures ranges.	76
Table 14- Hydration reaction of the different formulations studied at 7 and 28 days.....	78
Table 15- Mg/Si ratio for the different MgO-SiO ₂ systems according EDS results.	79
Table 16- Compressive strength results of the different MgO-SiO ₂ systems and control samples (100% Portland cement). Tukey test (0.05 confidence) are represented next to the numeric value. Compressive strength at 28 days to compressive strength at 7 days ratio is on the right column.	83
Table 17- MOR, LOP and MOE results of every formulation at 28 days and after 200 cycles of accelerated ageing.....	86
Table 18- SE and SD results of every formulation at 28 days and after 200 cycles of accelerated ageing.	88
Table 19- BD, WA and AP results of every formulation at 28 days and after 200 cycles of accelerated ageing.....	89
Table 20-Average EDS values of the amorphous phases for the Uncarbonated and Carbonated samples after ageing. For Carbonated samples, EDS values are grouped considering the different compound sizes. 50 spectrums are considered for each average values.	107
Table 21- Parameters of the different Gaussian curves obtained to quantify the mass loss from dehydration and decarbonation processes of the HMC in both peaks. Xc, w, A and AT stand for center of the curve, full width at half maximum, area and total area. C+A and C+NA are the aged and unaged carbonated samples respectively.	109
Table 22- Modulus of rupture, specific energy (at MOR) and specific deflection (at MOR) values for the different studied formulations. $MOR = P_{m\acute{a}x} \cdot L_b \cdot h^2$. $SE = F \cdot d\epsilon_b \cdot h$ and $= \epsilon_L$; where	

P_{max} is the maximum load applied on the material, L is the major span between supports, b is the width of the sample, h is the thickness of the sample and ϵ is the registered deformation

111 Table 23- Modulus of elasticity and limit of proportionality for the different studied formulations. $MOE = 276 \cdot L^3 \cdot 1296 \cdot b \cdot h^3 \cdot m$ and $= PLOP \cdot Lb \cdot h^2$; where $PLOP$ is the maximum load applied in the elastic region, L is the major span between supports, b is the width of the sample, h is the thickness of the sample and m is the tangent of the curve (load vs. deflection) in the elastic region..... 112

Table 24- Apparent porosity (AP), bulk density (BD) and water absorption (WA) values for the different formulations. 113

Table 25. Flexural results of every formulation after 5 days curing at 55°C. Modulus of rupture, limit of proportionality, specific energy (at MOR and 50% MOR), specific deflection (at MOR and 50% MOR) and modulus of elasticity values for the different studied formulations. $MOR = P_{m\acute{a}x} \cdot Lb \cdot h^2$, $LOP = PLOP \cdot Lb \cdot h^2$, $SE = F \cdot d\epsilon b \cdot h$, $MOE = 276 \cdot L^3 \cdot 1296 \cdot b \cdot h^3 \cdot m$ and $= \epsilon L$; where P_{max} is the maximum load applied on the material, $PLOP$ is the maximum load applied in the elastic region, L is the major span between supports, b is the width of the sample, h is the thickness of the sample, ϵ is the registered deformation and m is the tangent of the curve (load vs. deflection) in the elastic region. 0% stands for MgO-SiO₂ samples with no sepiolite replacement. PC stands for PC cement samples used as a control samples. The rest of the samples indicate the percentage and type of sepiolite replacement..... 123

Table 26- Physical characterization of the composites for every formulation after 5 days curing at 55°C. 0% stands for MgO-SiO₂ samples with no sepiolite replacement. PC stands for PC cement samples used as a control samples. The rest of the samples indicate the percentage and type of sepiolite replacement..... 126

Table 27- Crystallinity index and crystallite size test results of the sisal fibres untreated and after 5 months and 400 accelerated ageing cycles embedded in MgO-SiO₂ cement and PC **¡Error! Marcador no definido.**

TABLE OF CONTENTS

1	INTRODUCTION	18
1.1	IMPORTANCE AND INNOVATION OF THE WORK	18
1.2	THE USE OF CELLULOSE-BASED MATERIALS AS REINFORCING ELEMENTS IN FRCC.....	20
1.2.1	Global warming perspective	20
1.2.2	CO2 encapsulation in cellulose as main approach	21
1.2.3	Cellulose as fibre reinforcement.....	22
1.2.4	Structure of cellulose-based fibres.....	23
1.3	PERFORMANCE OF THE FIBRES AS REINFORCEMENT FOR BENDING SOLICITATIONS.....	24
1.4	DURABILITY OF THE VEGETABLE FIBRES IN CEMENTITIOUS MATRICES	26
1.4.1	Fibres degradation	26
1.4.2	Fibre-matrix interface modification	29
1.5	SOLUTIONS AGAINST THE DEGRADATION OF CELLULOSE-BASED FIBRES.....	30
1.5.1	Low Ca(OH) ₂ cementitious matrices	30
1.5.2	Use of pozzolan additions.....	30
1.5.3	Use of carbonation techniques.....	32
1.5.4	Fibre treatments	34
1.5.5	Limitations of the proposed solutions	34
1.6	LOW-ALKALINITY MATRIX COMPOSITES BASED ON MAGNESIUM OXIDE CEMENT	35
1.6.1	Mg in low-alkalinity hydraulic binders	35
1.6.2	Mg carbonate cements	36
1.6.3	Magnesium oxide (MgO) based cements.....	36
1.6.4	Magnesium oxide (MgO) and silica (SiO ₂) based cements	37
1.7	CLARIFYING REMARKS ABOUT THIS WORK.....	38
1.7.1	Use of reactive MgO from MgCO ₃ thermal decomposition	38
1.7.2	Lower carbon alternatives for obtaining reactive MgO	39
1.7.3	Use of reactive SiO ₂	41
1.7.4	Dewatering-pressing moulding technique (DPM).....	42
1.8	STRUCTURE OF THE THESIS	43
1.9	AIM OF THE DIFFERENT BLOCKS.....	45
1.9.1	BLOCK 1.....	45
1.9.2	BLOCK 2.....	46

1.9.3	BLOCK 3.....	46
1.9.4	BLOCK 4.....	47
1.9.5	BLOCK 5.....	47
2	LITERATURE REVIEW.....	48
3	MATERIALS AND METHODS.....	54
3.1	BLOCK 1.....	54
3.1.1	Materials preparation and characterization.....	54
3.1.2	Test methods.....	56
3.2	BLOCK 2.....	57
3.2.1	Materials preparation and characterization.....	57
3.2.2	Composites formulation and preparation.....	59
3.2.3	Test methods.....	60
3.3	BLOCK 3.....	61
3.3.1	Materials preparation and characterization.....	61
3.3.2	Curing treatments.....	62
3.3.3	Ageing treatment.....	63
3.3.4	Test methods.....	63
3.4	BLOCK 4.....	64
3.4.1	Materials preparation and characterization.....	64
3.4.2	Test methods.....	66
3.5	BLOCK 5.....	68
3.5.1	Materials preparation and characterization.....	68
3.5.2	Test methods.....	69
4	RESULTS AND DISCUSSIONS.....	71
4.1	BLOCK 1.....	71
4.1.1	XRD characterization.....	71
4.1.2	TG characterization.....	73
4.1.3	FT-IR characterization.....	76
4.1.4	Hydration reactions and systems composition.....	77
4.1.5	SEM.....	79
4.1.6	Matrix selection for fibre-cement purposes: pH evaluation and compressive strength analysis.....	81
4.2	BLOCK 2.....	85

4.2.1	Flexural test	85
4.2.1.1	Composites reinforced with pine fibres	85
4.2.1.2	Composites reinforced with eucalyptus fibres	88
4.2.2	Apparent porosity vs MOE	90
4.2.3	SEM analysis	91
4.3	BLOCK 3	97
4.3.1	XRD analysis	97
4.3.2	TG and DTG analysis	99
4.3.3	SEM	102
4.3.4	EDS analysis	104
4.3.5	Hydrated Magnesium Carbonates (HMC) thermodynamic stability	107
4.3.6	Mechanical and physical tests	109
4.4	BLOCK 4	113
4.4.1	Paste tests	113
4.4.1.1	Hydration of the pastes and dynamic MOE results	113
4.4.1.2	Paste micrographs	116
4.4.2	Composite tests	118
4.4.2.1	Flocculation tests	118
4.4.2.2	Drainage tests	121
4.4.2.3	Flexural tests	122
4.4.2.4	Composite images	125
4.4.2.5	Physical tests	125
4.5	BLOCK 5	126
4.5.1	TG and DTG analysis	126
4.5.2	XRD analysis	131
4.5.3	DSC analysis	134
4.5.4	SEM and EDS analysis	135
5	CONCLUSIONS	140
5.1	BLOCK 2	141
5.2	BLOCK 3	143
5.3	BLOCK 1	140
5.4	BLOCK 4	144
5.5	BLOCK 5	145

6	POSSIBLE FUTURE WORKS.....	147
	REFERENCES	148

1 INTRODUCTION

1.1 IMPORTANCE AND INNOVATION OF THE WORK

Composite materials are a key solution for universal challenges in terms of materials engineering and science. A composite material, also called composite, is a solid material that results when more than one substance, each with its own characteristics, are combined to create a new substance whose properties are superior to those of the original components in a specific application (ENCYCLOPÆDIA BRITANNICA, 2013). Remarkable properties of composites may be achieved by embedding fibres of one substance in a host matrix of another. That is the case of fibre-reinforced composites (FRC).

While the structural value of a bundle of fibres is low, the strength of individual fibres can be harnessed if they are embedded in a matrix that acts as an adhesive. Therefore, fibres impart structural strength to the composite, while the matrix protects the fibres from environmental stress and physical damage and imparts thermal stability to them. The fibre-matrix combination also reduces the potential for a complete fracture; if one fibre fails cracking may not extend to other fibres, whereas a crack that starts in a monolithic (or single) material generally continues to propagate until that material fails (ENCYCLOPÆDIA BRITANNICA, 2013).

The most used composite in the construction industry, sector within the scope of this research, is reinforced concrete. However, this work focuses on those materials formed by a hydraulic cementitious matrix and various discreetly incorporated aggregates and discontinuous fibres: Fibre Reinforced Cementitious Composites (FRCC).

Sustainability is a growing worldwide concern in view of the limited natural resources, energy production, wastes disposal and polluting gases emissions. The use of regional agro-industrial residues is a smart strategy to save energy in order to attend the global construction market. Ligno-cellulose pulp and vegetable fibre from several agro-industrial processes may also be an alternative solution for durable fibre-cement products and consequently more sustainable materials (ARDANUY; CLARAMUNT; TOLEDO FILHO, 2015). At the same time, the use of lignocellulosic fibres presents an attractive potential for tropical countries in Africa and South America since their availability of quality materials that allow the manufacture of building elements at low cost. It also allows the development of a competent industry, with the possibility of international trade (SAVASTANO JR; WARDEN; COUTTS, 2003). In fact, with the development and

evolution of the Hatschek technology, cellulose fibres have been traditionally used to retain fine particles during the manufacturing process of fibre-cement products.

Despite the advantages of using vegetable fibres as reinforcement in FRCC, a significant drawback has been widely reported: the durability of composites. Contrarily to what happens with synthetic fibres, i.e. polyvinyl alcohol (PVA) and polypropylene (PP), mechanical and physical integrity of vegetable fibres are affected within the calcium based cement matrices. Under these circumstances, in porous alkaline environments ($\text{pH} > 12$), cellulose based fibres are degraded progressively, losing all its reinforcing performance. At this point is where research on new FRCC must find a compromise solution, avoiding excessive energy costs that cause the production of synthetic fibres and the limited durability offered by lignocellulosic fibres.

Literature regarding this loss of mechanical properties of vegetable fibres over time in Portland cement (PC) based FRCC claims that dissolution and decomposition of hemicellulose and lignin takes place. Thus, the cohesion between the individual fibres is broken at micro and macro scale. This breakdown is produced by the attack of $(\text{OH})^-$ ions from the calcium hydroxide $[\text{Ca}(\text{OH})_2]$ solutions over hemicellulose and lignin molecules. Another detrimental effect on the mechanical performance of the lignocellulosic fibres is the crystallization thereof. This phenomenon in PC based FRCC occurs when cellulose chains are surrounded by Ca^{2+} cations from $\text{Ca}(\text{OH})_2$ formed after calcium silicates hydration (C-S-H).

Traditionally, two strategies have been proposed to preserve cellulose-based fibres In FRCC:

1. Reduction of the amount of $\text{Ca}(\text{OH})_2$ solution in the cement pores
2. Fibre treatment for a chemical compatibility between cellulose based fibres and PC.

However, these techniques have not totally succeeded in their purpose. The first one do not avoid high concentrations of Portlandite, $\text{Ca}(\text{OH})_2$, in liquid phase reached during the early hours of the hydration process (TAYLOR, 1997) and remain in large proportions (about 25%) in the matrix for a certain period of time depending on the consumption speed. This portlandite reduction is not an instantaneous process, so meanwhile fibres are subjected to highly alkaline environments. The second method would involve an industrial sophisticated technique that reduces the economic and environmental benefits of using vegetable fibres.

In this thesis, an alternative to avoid vegetable fibres degradation in FRCC is explored: the use of a clinker free cement, a cement based on MgO hydrated compounds, with insignificant content in Ca (<1% by mass). With the use of cement based on magnesium oxide, to the matrix direct contact with Ca^{2+} is prevented.

Since MgO solubility is more than 10 times lower compared to CaO, and therefore $(\text{OH})^-$ content is also considerably lower, MgO-based cements are lower alkaline than PC. This new type of cement presents pH values below 11 over time, meanwhile Portland cement pH is above 12.5 from the very early stages of hydration (LEA; HEWLETT, 2004). This reduced alkalinity is essential to yield more stable environments on pores solutions at high moisture exposure conditions. Besides, MgO-based cements may offer satisfactory mechanical strength compared to PC.

According the above exposed statements, this work intends to:

1. Obtain FRCC by using MgO-based cements as a hydraulic binder matrix and cellulose-based fibres as reinforcing elements
2. Achieve optimal mechanical performance of the intended FRCC
3. Preserve lignocellulosic reinforcement properties at long term

Along next chapters that all together comprise this thesis, all the statements made in the present chapter will be further developed, detailed and properly referenced.

1.2 THE USE OF CELLULOSE-BASED MATERIALS AS REINFORCING ELEMENTS IN FRCC

1.2.1 Global warming perspective

In spite of non-conclusive predictions on the upcoming effects of climate change, it exists a neat relationship between the rising temperature of both atmosphere and oceans and the increased concentration of greenhouse effect gases on the atmosphere. All scientific evidences point out that climate change will become more intense on the assumption that no reduction of greenhouse effect gases emissions is attained. In industrialized areas, it is especially worrying the emission of carbon dioxide (CO_2) to the atmosphere from the combustion of fossil fuels due to the greenhouse effect of this gas. Different alternatives to alleviate this consequence are likely.

1.2.2 CO₂ encapsulation in cellulose as main approach

In order to face global warming a possible solution is to intake the excess of CO₂ from the atmosphere and store it. In nature, plants already naturally carry out this chemical process by photosynthesis. Thus, carbon from CO₂ becomes part of the plants structure, mainly composed by large polymeric chains. Encapsulating plant matter is presented as a potential technique to achieve the atmospheric CO₂ reduction. At the same time, plant fibres show excellent technical properties when used in composites, Table 1, that turn this material into an optimal choice to develop a low-carbon or hypo-carbonic technology (BODROS; BALEY, 2008; BOURMAUD et al., 2013; FAKIROV; BHATTACHARYYA, 2007; FARUK et al., 2012; OCHI, 2008; OKSMAN; SKRIFVARS; SELIN, 2003; SUMMERSCALES et al., 2010). Since the renewable nature of plant fibres and the low energy demand to obtain them, this technology is increasingly developed by different industries. However, it still exists a potential room for improvement and implementing this method in building and civil construction.

Table 1- Mechanical properties of different fibres used in composites application

Fiber	Density	Young's modulus (GPa)	Tensile strength (MPa)	Elongation at break (%)
Flax	1.54	27.5–85	345–2000	1–4
Ramie	1.5–1.56	27–128	400–1000	1.2–3.8
Hemp	1.47	17–70	368–800	1.6
Jute	1.44	10–30	393–773	1.5–1.8
Sisal	1.45–1.5	9–22	350–700	2–7
Coconut	1.15	4–6	131–175	15–40
Cotton	1.5–1.6	5.5–12.6	287–597	7–8
Nettle	1.51	24.5–87	560–1600	2.1–2.5
Kenaf	1.2	14–53	240–930	1.6
Bamboo	0.6–1.1	11–17	140–230	–
E-glass	2.5	70	2000–3500	2.5
Carbone	1.4	230–240	4000	1.4–1.8

Source: The hygroscopic behaviour of plant fibres: a review (CÉLINO, A. et al. The hygroscopic behavior of plant fibers: a review. *Frontiers in Chemistry*, Lausanne, v. 1, art. 43, 2014).

1.2.3 Cellulose as fibre reinforcement

Construction industry historically paid minor attention to plant fibres due to the biodegradable nature of these elements and, therefore, to the high maintenance cost and reduced durability. A prospective application to iron this disadvantage out is the embedment of plant fibres within construction materials. This concept emulates millennial construction techniques as adobe. In the case of cementitious materials, plant fibres may contribute to resist tension stresses the same way other reinforcing fibres do, while plant fibres are protected from environmental conditions so are sheltered from biological degradation.

To understand the true potential of using use of cellulosic fibres in FRCC is necessary to consider the potential benefits and disadvantages associated with this application. Some advantages and disadvantages are highlighted below (SAVASTANO JR.; SANTOS; AGOPYAN, 2009):

Table 2-Advantages and disadvantages of using cellulosic-based fibres as reinforcement in FRCC

Advantages	Disadvantages
<ul style="list-style-type: none"> • Low specific weight <ul style="list-style-type: none"> ➤ high specific mechanical properties • Renewable resource • Little energy for its production <ul style="list-style-type: none"> ➤ while oxygen is released to the environment • Produced with minimal investment • Good thermal and acoustic properties 	<ul style="list-style-type: none"> • Characteristics dependent on uncontrollable factors <ul style="list-style-type: none"> ➤ such as weather conditions • High moisture absorption <ul style="list-style-type: none"> ➤ increases in volume of the fibre • Limited temperature in the obtaining process • Price can fluctuate depending on: <ul style="list-style-type: none"> -crop yields -agricultural policies

Source: SAVASTANO JR., H.; SANTOS, S. F.; AGOPYAN, V. 3 - Sustainability of vegetable fibres in construction. In: KHATIB, J. M. (Ed.). **Sustainability of construction materials**. Cambridge: Woodhead Publishing, 2009. p. 55–81.

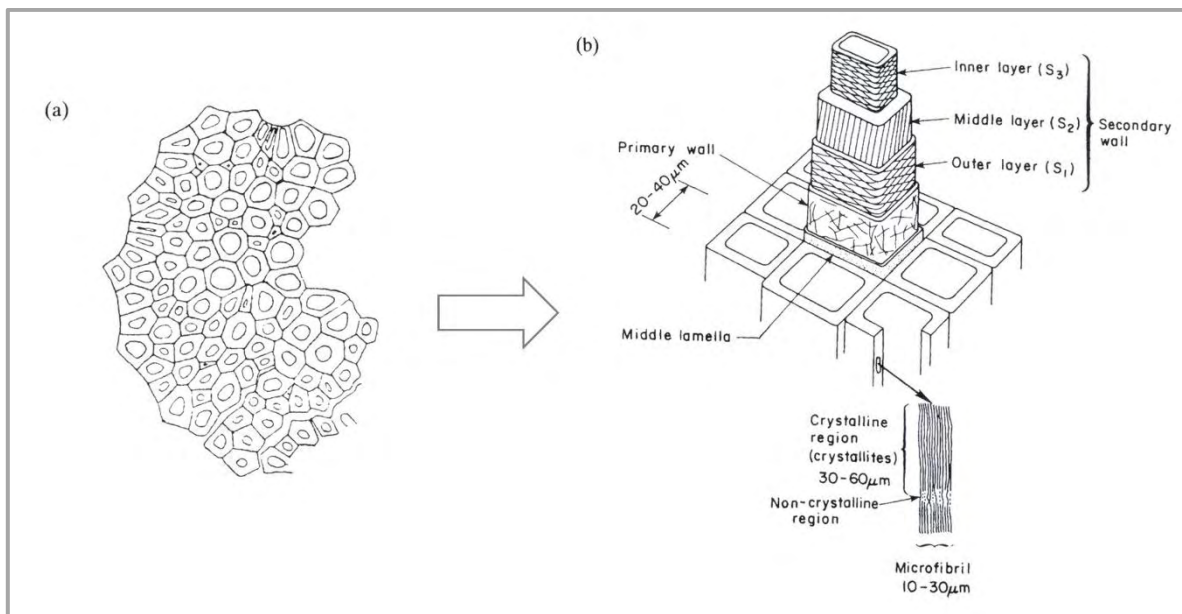
This approach was initially taken by fibre-cement industry given that asbestos fibres became gradually banned because of their hazardousness for human health. Nevertheless, the use of plant fibres as reinforcing elements in cementitious composites was not successful due to the durability of the products. It was found to be degraded under cement alkaline environment and, consequently, the benefit of using plant fibres was futile. Then, fibre-cement industry moved to alternative more chemically compatible reinforcing polymeric fibres, as PVA initially and PP recently, though their higher economic, energetic and environmental cost (IKAI et al., 2010). Still, natural cellulose (type I) microfibrils in the crystalline regions, zoomed in Figure 1b, have outstanding elastic properties i.e.

Young's Modulus in between 128 and 155GPa, that when it is weighted by its specific density of around ($1.5 \text{ g}\cdot\text{cm}^{-3}$) results in a specific Young's Modulus of around $138\text{GPa}\cdot\text{g}^{-1}\cdot\text{cm}^{-3}$.

1.2.4 Structure of cellulose-based fibres

Though cellulose is the main component of plant fibres and the responsible for the exceptional reinforcing properties, it is important to note that cellulose is not the only constituent of plant fibres. Besides, each plant species shows differences in fibres microstructure with those of other species. It also should be noted that the microstructure of a single fibre is quite complex, and the fibres are composed of many cells fibre, as shown in Figure 1, where a sisal fibre section is schematically displayed.

Figure 1- Schematic cross section (a) and representation of the structure (b) of a sisal fibre



Source: BENTUR, A.; MINDESS, S. **Fibre reinforced cementitious composites** 2nd ed. London: Taylor & Francis, 2007. p. 431.

In the particular case of sisal fibres, schematised in Figure 1a, its diameter is 0.3 mm and the cross section may be compound up to about 100 cells. The structure of a single cell presented schematically in Figure 1b, shows several layers of fibrils making up the fibre wall. The orientation of the fibrils of each layer of the wall is different. Secondary S₂ wall is oriented in the macrofibre direction and mainly composed by large molecules of cellulose, with a degree of polymerization of

about 25,000. The chains of cellulose molecules are grouped into longitudinal microfibrils. The other components of the cell wall, hemicellulose and lignin, have much lower polymerization degrees and are mainly in the middle lamella connecting the cells of individual fibres together. Thus, sisal fibres are made out of approximately 54–66% cellulose, 12–17% hemicellulose, 7–14% lignin, 1% pectin and 1–7% ash (MELO FILHO; SILVA; TOLEDO FILHO, 2013).

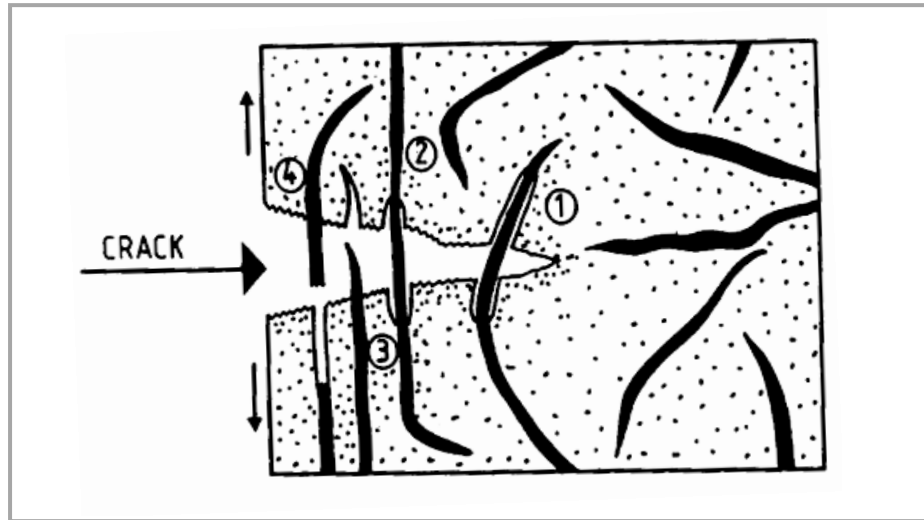
In recent years, an important scientific effort has been put to understand cellulose degradation process and significant advances are reached (MELO FILHO; SILVA; TOLEDO FILHO, 2013; MOHR; NANKO; KURTIS, 2005; MOHR; BIERNACKI; KURTIS, 2006; TOLÊDO FILHO et al., 2000; TOLEDO FILHO et al., 2009; SILVA; MOBASHER; TOLEDO FILHO, 2009; WEI; MEYER, 2014). With current expertise, plant fibres are presented as a viable alternative to synthetic polymeric fibres for the fibre-cement industry and several products have been developed both in lab and industrial scale, proving the viability of this technology. Also further technical defies arise from this experience and new ways of reinforcing materials may be explored, even replacing steel reinforcing bars from concrete structures. In this sense, the replacement of steel materials by cellulose would involve an extra CO₂ reduction since the high energy cost necessary to produce steel products in contrast with cellulose ones.

1.3 PERFORMANCE OF THE FIBRES AS REINFORCEMENT FOR BENDING SOLICITATIONS

Regarding fibres capacity to reinforce FRCC, it is assumed that in cement matrices under bending loads, lignocellulosic fibres induce mechanisms of fracture with a linear elastic branch (BENTUR; MINDESS, 2007). This is in contrast with unreinforced cement elements, which have a brittle behaviour. Thus, fibres addition to the matrix increases bending strength and the capacity of FRCC to absorb more energy before breaking by the distribution of the cracks throughout the material.

Rupture or collapse in the FRCC comes from an inside defect. These deficiencies include broken fibres, imperfection in the cement matrix or debonding between the matrix and the fibre. Figure 2 shows a schematic representation of a cross section of any composite reinforced with an indeterminate fibre.

Figure 2- Schematic representation of a cross section of any composite reinforced with an indeterminate fibre



Source: TONOLI, G. H. D. **Fibras curtas de Eucalipto para novas tecnologias em fibrocimento**. 2010. 128 f. Tese (Doutorado) – Interunidades em Ciências e Engenharia de Materiais, Universidade de São Paulo, São Carlos, 2010.

The illustration shows a break point before the global collapse. It is also shown that at a distance from the start of the crack, which propagates along the section, the fibres remain intact. In the fracturing process, the fibres tend to assist in the distribution of the stresses generated in the material by the friction generated between matrix and fibre and chemical bonding forces between them. If bond stresses and these hydrogen bonds do not exceed the maximum tensile stress of the fibre, a debonding process at the interface between fibre and matrix (points 1 and 2 in Figure 2) is produced. This debonding, also known as pull-out, is produced by the breaking of hydrogen bonding and physical type forces at the interface between fibre (point 3 in Figure 2). Pull-out means higher toughness performance of the material. Otherwise, when the fibre strength is lower than that of the chemical and physical forces generated between fibre and matrix, what occurs is breaking of the fibre, which leads to a decrease in toughness of the composite.

Therefore, to avoid a brittle material behaviour it must found a compromise where the fibre-matrix adhesion forces are balanced with the chemical adhesion mechanisms. It is also important to remember that water plays an important role in the mechanisms of adhesion of the fibres in the matrix, since the insertion of water molecules between the hydroxyl groups at the interface generates weaker hydrogen bonding between fibre and matrix (TONOLI, 2010).

1.4 DURABILITY OF THE VEGETABLE FIBRES IN CEMENTITIOUS MATRICES

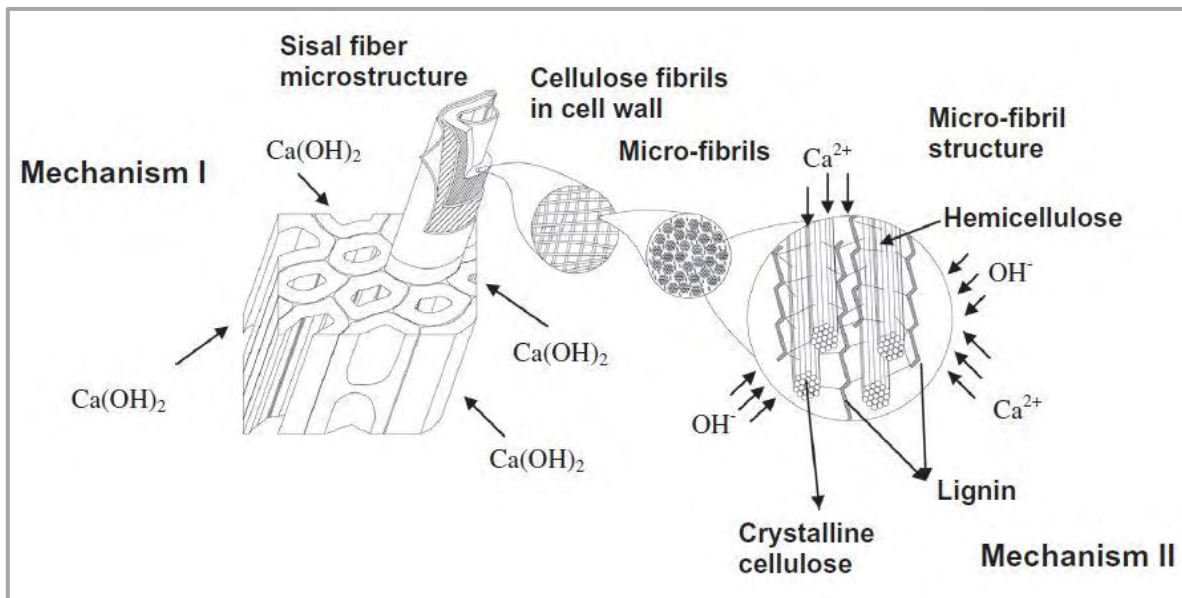
Despite the potential benefits produced by the use of vegetable fibres as reinforcement in FRCC, these fibres present a huge inconvenience to solve their: durability. The long-term performance of composites reinforced with cellulose fibres can be affected by several processes, either separately or at the same time.

1.4.1 Fibres degradation

Traditionally two fibre degradation mechanisms have been mainly reported in FRCC composites: fibre mineralization due to the precipitation of calcium hydroxide in the fibre cell and surface (SINGH, 1985) and degradation of cellulose, hemicellulose and lignin due to the adsorption of calcium and hydroxyl ions (GRAM, 1983a, 1983b, 1986). Degradation of cellulose is not considered responsible for the major deterioration of the fibres, principally due to this process takes places at temperatures over 75°C and because of the large degree of polymerization of cellulose (>25,000). Thus the studies regarding alkaline attack have been focused on hemicellulose and lignin degradation which are amorphous with relative low polymerization degree, so they have a higher hydrolysis rate and solubility in alkaline medium than cellulose (WEI; MEYER, 2014).

Through years of research these two mechanisms have confirmed and they and their effects have been widely studied (TOLEDO FILHO et al., 2009; MELO FILHO; SILVA; TOLEDO FILHO, 2013; WEI; MEYER, 2014). Figure 3 shows the two main mechanisms of degradation of a sisal fibre.

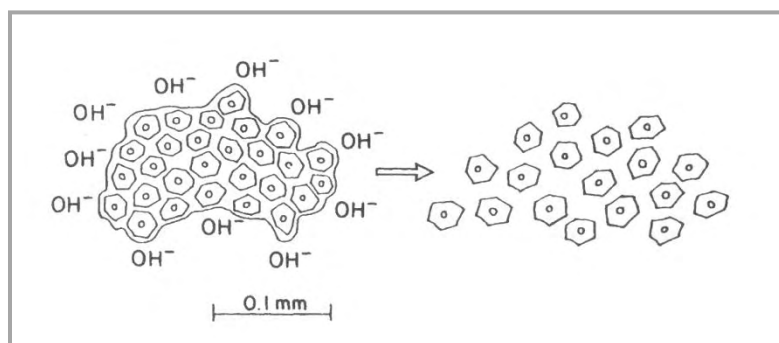
Figure 3- Schematic representation of the mechanisms of degradation of a sisal fibre



Source: MELO FILHO, J. de A.; SILVA, F. de A.; TOLEDO FILHO, R. D. Degradation kinetics and aging mechanisms on sisal fiber cement composite systems. **Cement and Concrete Composites**, Kidlington, v. 40, p. 30–39, July. 2013.

As lignin and hemicellulose are responsible for linking the microfibril structure, their degradation may also lead to a reduction in the macro mechanical properties of the fibres as a result of breaking the link between individual fibre cells (GRAM, 1983a; MELO FILHO; SILVA; TOLEDO FILHO, 2013; WEI; MEYER, 2014). This process is schematically explained in Figure 4.

Figure 4- Schematic representation of alkaline hydrolysis on sisal fibre



Source: BENTUR, A.; MINDESS, S. **Fibre reinforced cementitious composites**. 2nd ed. London: Taylor & Francis, 2007. p.458.

Vegetable fibres can suffer various degrees of degradation when exposed to an alkaline environment. The extent of the attack, as determined by strength loss of the fibres, depends on the

kind of alkaline solution (TOLEDO FILHO et al., 2009). The embrittlement of the composites may be mainly associated with the mineralisation of the fibres due to the migration of hydration products, especially calcium hydroxide, to the fibre lumen, walls and voids (TOLEDO FILHO et al., 2000). This may also reduce the amount of cellulose (MELO FILHO; SILVA; TOLEDO FILHO, 2013).

Despite of all researches agree that mineralisation brittles the fibres so toughness may be severely decreased, there is no wide assent about the effects on fibres tensile strength. Some authors (AKERS; STUDINKA, 1989) suggest that the fibre flexural strength increases with prettification, while some others propose the opposite (TOLEDO FILHO et al., 2009; MELO FILHO; SILVA; TOLEDO FILHO, 2013). Nevertheless, even considering positive effects on fibre tensile strength, fibre mineralization is an undesired phenomenon since it also reduces the pull-out mechanism in FRCC.

Another factor to be considered is that fibres degradation is more obvious when they are attacked by Ca(OH)_2 than with other alkaline hydroxide solutions. This aspect may be associated with the calcium hydroxide deposited in the lumen and voids of the fibre cells (GRAM, 1983a; SINGH, 1985; TOLEDO FILHO et al., 2000). According to this, apart from alkaline attack it is important the composition of alkaline minerals that contribute differently to the mineralization process of the fibres.

According to different studies where FRCC is assessed by accelerated ageing tests, the degradation process occurs rapidly, from the early stages (MELO FILHO; SILVA; TOLEDO FILHO, 2013; WEI; MEYER, 2014) and after longer ages a quite expressive modification in the flexural behaviour is observed. In these works, the residual mechanical parameters after accelerated ageing are the same as those observed in the unreinforced matrix. It was proposed that the initial calcium hydroxide content in the composite plays a significant role on the degradation along with wetting and drying cycles. Improvements in the composite durability are likely related to a reduction in the calcium hydroxide content and the stabilization of the alkali content. For the composites with reduced content in Ca(OH)_2 , fibre mineralization was satisfactorily prevented (MELO FILHO; SILVA; TOLEDO FILHO, 2013). Accelerated ageing treatments speed up the effect of both alkali hydrolysis of fibre's amorphous components and mineralization of fibre cell wall. This was confirmed by the highest crystallinity indices and minimum content of cellulose (WEI; MEYER, 2014).

1.4.2 Fibre-matrix interface modification

This process of degradation is important because strength and ductility performance is primarily governed by the fibre–matrix interface (BENTUR; MINDESS, 2007), or also called Interface Transition Zone (ITZ) , which allows fibre bridging and bonding mechanism which results in the distribution of micro-crack pattern (MELO FILHO; SILVA; TOLEDO FILHO, 2013). Reductions in the frictional stress may be produced because of an interface fatigue mechanism. This is due to the volumetric variation of the sisal fibres after wetting and drying stress (MELO FILHO; SILVA; TOLEDO FILHO, 2013). Since the reductions in the frictional stress, reduction in strength and toughness is produced from the early ages of the composites.

Several studies, with help of Scanning Electrons Microscopy (SEM), have reported modifications in the ITZ over time. In these studies was found that the gap between the binding zone surrounding the fibre surface and the fibre perimeter is larger in an unaged specimens than in the specimen submitted to ageing (TOLEDO FILHO et al., 2000).

There are mechanical properties specifically related to these modifications in the ITZ. Certain works associate a weak matrix in the vicinity of the fibre, and therefore its easiness for cracking, to the increase of the FRCC ductility (SAVASTANO JR; WARDEN; COUTTS, 2005). These authors points to the densening of matrix areas around the fibres or fibre embrittlement due to migration of hydration products from the matrix to the fibres as the main that increases flexural strength until first crack appears. This increase for the first crack to appear yields reduction in toughness, by reducing the flexibility and deformation capacity of the fibres (TOLEDO FILHO et al., 2000).

However, other authors consider denser matrices surrounding the fibres as more favouring conditions for pull-out processes to occur. In this sense, a denser ITZ is likely to improve the contact between fibres and cement matrix, and certainly favouring the better adhesion between them. Thus, higher energy is absorbed by the composite due to the frictional slipping process during the pulling-out of fibres with a better interface with the matrix (ALMEIDA et al., 2013; PIZZOL et al., 2014).

1.5 SOLUTIONS AGAINST THE DEGRADATION OF CELLULOSE-BASED FIBRES

1.5.1 Low Ca(OH)₂ cementitious matrices

As previously mentioned, the lignin-cellulosic fibres used as reinforcements in FRCC exhibit serious problems of durability due to a number of factors, most notably the fibre degradation in highly alkaline environments. The majority of studies in this area agree that this loss of mechanical properties of the vegetable fibres over time in PC matrices is caused by the dissolution and decomposition of hemicellulose and lignin of the middle layer. Thus, the link between the individual fibres is broken. This breakdown is produced by the attack of OH⁻ ions from the Ca(OH)₂ on lignin and hemicelluloses. In turn, another detrimental effect on the mechanical performance of the fibres is the crystallization thereof and embrittlement of the ITZ. This phenomenon occurs when the cell lumen is filled with cations Ca²⁺ and fibre surrounding presents a high Ca(OH)₂ concentration exceeding from calcium silicates hydration.

It seems logical, therefore, eliminate, or at least reduce the amount of Ca(OH)₂ in the matrices to improve the durability of the fibres. Many authors have already achieved successful experiences by this approach.

1.5.2 Use of pozzolan additions

Within the traditional cement manufacturing process, considering the energy required for cement production processes and the stoichiometry of limestone and clay calcination (which also implies CO₂ emissions), a straight route to reduce CO₂ emissions has been the reduction of clinker to obtain cementitious materials. This reduction of clinker is likely through the replacement of Portland cement by other binding products. This proposed solution, the reduction of calcium hydroxide within the cementitious matrix, becomes a real solution with the partial replacement of cement by pozzolanic materials (JOHN et al., 2005; MOHR; BIERNACKI; KURTIS, 2007; SAVASTANO JR.; SANTOS; AGOPYAN, 2009; SANTOS et al., 2012).

When referring to the pozzolanic materials is referred to all, both natural and artificial, materials capable of combining directly with lime, at room temperature and in the presence of water, to form inorganic cementitious materials compounds similar to those major constituents

originated in the hydration of Portland cement. Also pozzolans are defined as follows (EN 494:2012+A1:2015, 2012):

Siliceous or siliceous and aluminous material which, in itself, possesses little or no cementitious value but which will, in finely divided form and in the presence of water, react chemically with calcium hydroxide at ordinary temperature to form compounds possessing cementitious properties.

In this regard, it should be noted that Ca(OH)_2 , (CH), present in cement matrices is derived from the hydration reactions of bicalcium silicate (C2S) and tricalcium (C3S) to form calcium silicate hydrate gel ($\text{C}_3\text{S}_2\text{H}_3$) commonly mentioned as S-C-H phase. It is in this hydration reaction where the calcium hydroxide or portlandite is released according to the following equations:

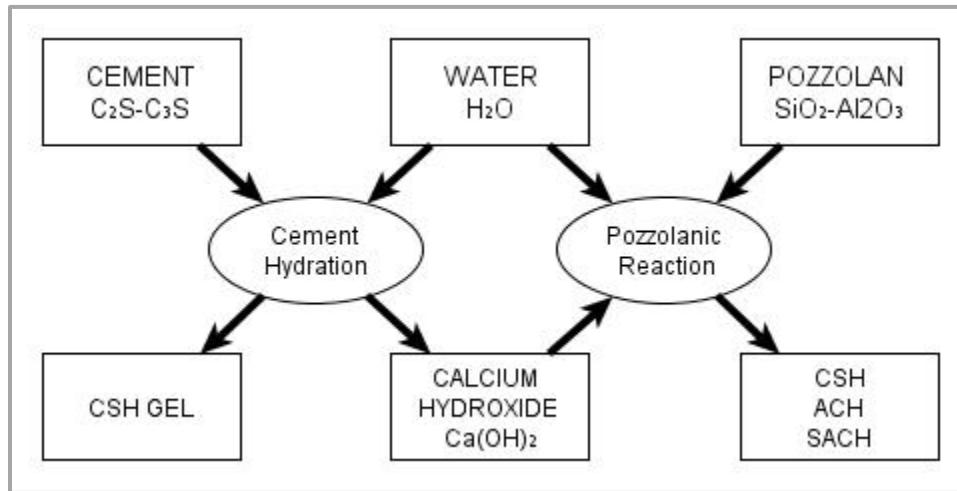


Thus, pozzolans therefore react with the calcium hydroxide released by the hydration of Portland cement to give other products of desirable mechanical properties as hydrated gels (silicates (SCH), aluminates (ACH) and calcium silico-aluminates hydrated (ASCH), as shown below (Figure 5):



Therefore, the use of pozzolanic materials, in addition to meeting the goal of eliminating Portlandite content, help to improve the mechanical strength of the cementitious matrix.

Figure 5- Diagram of a pozzolanic reaction in conventional Portland cement



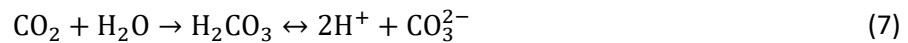
Source: Own creation

Considering the previous premises, 1) incorporation of plant fibre to resist tension stresses and 2) removal of $\text{Ca}(\text{OH})_2$ from the final hydrated binding composition, the partial replacement of PC by pozzolanic materials has been explored.

1.5.3 Use of carbonation techniques

In order to reduce the CO_2 concentration in the atmosphere, a similar strategy is the encapsulation of carbon within cementitious matrices. This procedure has been traditionally avoided in order to prevent steel reinforcement corrosion in building constructions. One of the main features of hardened Portland cement is its high alkalinity, which allows the passivation of the steel bars that reinforce concrete elements (TAYLOR, 1997). This elevated alkalinity is given by $\text{Ca}(\text{OH})_2$ from the cement hydration process, which is very soluble, releasing Ca^{2+} and $(\text{OH})^-$ ions to the cement pores suspensions. While $\text{Ca}(\text{OH})_2$ is desirable in terms of steel protection, this hydrated constituent is considered to provide reduced mechanical performance, being considered the weakest component of aged cement. Therefore, in cementitious materials where steel reinforcement is not required, $\text{Ca}(\text{OH})_2$ would not be of any importance, being its replacement by other stronger components a beneficial technique.

A possibility for both carbon encapsulation and $\text{Ca}(\text{OH})_2$ reduction in PC is possible through carbonation. Carbonation is a physicochemical process that takes place within the pores of hardened Portland cement. In the aqueous solution within PC matrices, $\text{Ca}(\text{OH})_2$ is constantly solved and precipitated according to (6). High alkalinity, and therefore high $(\text{OH})^-$ concentrations, in aqueous solutions promotes the easy formation of carbonic acid (H_2CO_3) so CO_2 gets dissolved, as shown in (7). Thus, alkalinity is reduced which favours the precipitation of calcite, (CaCO_3), following (8).



Carbonation in PC based materials naturally occurs at environmental conditions over time. This process is more important on the edges of the settled PC based elements, losing its effectivity to the inwards of the elements. CO_2 gets through the matrix pores and starts the carbonation process. This way, carbonation of cement elements has been proved to meet this principle, both removing $\text{Ca}(\text{OH})_2$ by its reaction with CO_2 and producing calcium carbonate (CaCO_3), a denser component, more rigid and stronger (FRÍAS; GOÑI, 2013; MORANDEAU; THIÉRY; DANGLA, 2015; MO; ZHANG; DENG, 2015; ZHA et al., 2015). Though densification of cement yields better mechanical attributes to the hydrated cement, it also hinders environmental CO_2 to the core of the PC based elements. This problem has already sorted out by the modification of the environment conditions (CO_2 concentration increase, optimal humidity and temperature) to boost carbonation reactions in the early stages of PC within the whole matrix.

Besides, in conjunction with the first strategy to encapsulate CO_2 using plant fibres as reinforcing material, carbonation becomes a favourable option since the removal of $\text{Ca}(\text{OH})_2$ from cement matrices has been evidenced efficient to increase cellulose durability and encapsulate CO_2 . When fibre-cement products are exposed to elevated CO_2 concentration at early ages, moreover, technical features are improved, obtaining outstanding products along with the encapsulation of CO_2 from the environment (ALMEIDA et al., 2013; PIZZOL et al., 2014; PURNELL; SHORT; PAGE, 2001; PURNELL et al., 2003; SANTOS et al., 2015a).

1.5.4 Fibre treatments

Another methodology to achieve a better long-term performance of the FRCC is the partial modification of the fibres' properties. Since fibre degradation is produced via contact with some compounds from PC hydration, it is also possible to avoid a direct interface between alkaline environments and potential degradable components of plant fibres (hemicellulose and lignin mainly) by modifying the surface of the fibres. This is feasible using different techniques such as grafting with different agents (BELGACEM; GANDINI, 2005; TONOLI et al., 2009b, 2013) and methane plasma treatment (BARRA et al., 2012), amongst others. The positive effects of these type of treatments on the durability of the fibres over time along with the possibility of combining any fibre treatment with less alkaline matrix boost this methodology.

Besides, other crude methods, like bleaching and hornification (TONOLI et al., 2012; BALLESTEROS et al., 2015), have been satisfactorily explored. Although these techniques are not entirely effective to avoid fibre degradation, it is possible to use them together with lower alkaline matrices. Thus, the effects of these methods are more effective with no interference.

1.5.5 Limitations of the proposed solutions

Despite the apparent benefits of the use of pozzolanic materials or carbonation techniques to improve the durability of vegetable fibres within a cement matrix, its application has limitations. The main obstacle is the chemical activity, pozzolanic activity or carbonation activity, which is based in the reaction with Ca^{2+} from $\text{Ca}(\text{OH})_2$. Pozzolanic reaction and carbonation are not instantaneous processes, so while the pozzolan and CO_2 reacts with portlandite, fibres undergo highly alkaline environments. Considering that $\text{Ca}(\text{OH})_2$ is dissolved in an aqueous solution, releasing Ca^{2+} cations, and given the hygroscopic nature of lignocellulosic fibres, Ca absorption by plant tissues is likely as well as an alkalinity increase in the cell walls. Although higher concentrations of Portlandite in liquid phase (about 25%) are reached during the early hours of the hydration process (TAYLOR, 1997), portlandite remains in large proportions in the matrix for a certain period of time depending on the rapidity of pozzolanic and carbonation reactions.

Regarding fibre treatments, this alternative would reduce the economic and environmental advantage of using cellulose-based fibres as reinforcement in FRCC. In this sense, cellulose-based materials bring limited improvement compared to PVA and PP fibres.

1.6 LOW-ALKALINITY MATRIX COMPOSITES BASED ON MAGNESIUM OXIDE CEMENT

In order to avoid direct contact between fibres and the high alkalinity water occluded within the matrix, this work explores the replacement of PC by a fast setting and lower alkalinity alternative binder: magnesium (Mg) based cement. The main advantage of using this type of cement is that the amount of Ca compounds is insignificant in its composition. Therefore, the reduction of Ca(OH)_2 in the hardened binder is utterly solved.

1.6.1 Mg in low-alkalinity hydraulic binders

MgO based cement, also known as reactive magnesia cements, may be described as cementitious materials in which composition MgO is used.

Mg is the eighth most abundant element in the solar system and constitutes about 2% of Earth crust. It is also the third most abundant element in solution in seawater, with a concentration of about 1300 ppm. However, MgO, or also known as magnesia or periclase, is not obtained by direct mining due to its scarcity on Earth crust. The most important rock-forming minerals containing magnesium are chlorites, pyroxene and amphibole group minerals, dolomites, and magnesium calcites (calcite with some of the Ca replaced by Mg). Mg is also present in magnesite (MgCO_3), nesquehonite ($\text{MgCO}_3 \cdot 3\text{H}_2\text{O}$), lansfordite ($\text{MgCO}_3 \cdot 5\text{H}_2\text{O}$) and brucite [Mg(OH)_2]. In addition, there is a series of basic hydrated magnesium carbonates having the empirical formula $x\text{MgCO}_3 \cdot y\text{Mg(OH)}_2 \cdot z\text{H}_2\text{O}$. These include hydromagnesite $4\text{MgCO}_3 \cdot \text{Mg(OH)}_2 \cdot 4\text{H}_2\text{O}$ and artinite $\text{MgCO}_3 \cdot \text{Mg(OH)}_2 \cdot 3\text{H}_2\text{O}$. Magnesium also occurs in salt deposits such as carnallite ($\text{KMgCl}_3 \cdot 6\text{H}_2\text{O}$), epsomite ($\text{MgSO}_4 \cdot 7\text{H}_2\text{O}$) and kieserite ($\text{MgSO}_4 \cdot \text{H}_2\text{O}$).

It has been estimated that the total mass of the sedimentary layer in Earth's crust is 1.4×10^{18} tonnes (WEDEPHOL, 1969). Carbonate rocks constitute about 8wt% of the total sediments (GOLDSCHMIDT, 1954). Magnesite (MgCO_3) is the magnesium end member of an isomorphous

series of carbonates. Hereafter, this study focuses on the use of MgO from MgCO₃ thermal decomposition, as follows:



1.6.2 Mg carbonate cements

MgCO₃ calcination according to (9) is reversible and it is possible to obtain a hydraulic binder through this opposite reaction called carbonation. Carbonation is also possible in an aqueous environment, which previously hydrates MgO to form Mg(OH)₂ and at last forms a Hydrated Magnesium Carbonate (HMC), with the generic form of xMgCO₃·yMg(OH)₂·zH₂O.



These HMC are the main binder component of this type of cement (LISKA; AL-TABBAA, 2009). This attempt of introducing Mg as a binding system was initially explored to reduce PC content in cementitious systems. However, this application is out of the purpose pursued by using MgO for composites reinforced with lignocellulosic fibres. Based on the results obtained from this experience, this HMC system is effective when the cement to aggregates ratio is too low (0.1), in which case compressive strength is even higher than PC. Nevertheless, since this system is based on carbonation, similar handicaps found in PC carbonation may arise for this innovative system, where higher cement to aggregates ratios result into less porous matrices that difficult carbonation process.

1.6.3 Magnesium oxide (MgO) based cements

The origin of magnesia cement, in 1867, was magnesium oxychloride cement (MOC), obtained from the reaction between MgO and an aqueous magnesium chloride (MgCl₂) solution. The main bonding phases found in this hardened system are Mg(OH)₂, 5Mg(OH)₂·MgCl₂·8H₂O (5-form) and 3Mg(OH)₂·MgCl₂·8H₂O (3-form) (SHAND, 2006). This material is widely known as Sorel cement, but it is not the only type of magnesia cement. Magnesium oxychloride cement has not remained popular in the building industry is that the magnesium oxychloride phase is not stable in

prolonged contact with water, which will result in the leaching of magnesium chloride from the cement phase, leaving $\text{Mg}(\text{OH})_2$ behind as the binder. Since $\text{Mg}(\text{OH})_2$ does not have adequate strength, the cement bond as a whole is severely weakened.

In the literature it is been reported two other well-known magnesia cements. The first is magnesium oxysulfate (MOS), which is the sulphate analogous of magnesium oxychloride and is formed by the reaction between Mg and magnesium sulphate (MgSO_4) in an aqueous solution. Four oxysulfate phases are formed at temperatures between 30 and 120°C: $\text{Mg}(\text{OH})_2 \cdot \text{MgSO}_4 \cdot 3\text{H}_2\text{O}$ (5-form), $3\text{Mg}(\text{OH})_2 \cdot \text{MgSO}_4 \cdot 8\text{H}_2\text{O}$ (3-form), $\text{Mg}(\text{OH})_2 \cdot \text{MgSO}_4 \cdot 5\text{H}_2\text{O}$, and $\text{Mg}(\text{OH})_2 \cdot 2\text{MgSO}_4 \cdot 3\text{H}_2\text{O}$. Only the 3-form and 5-form are stable at 25°C (SHAND, 2006). This cement has the same lack of water resistance as MOC cement.

The second is magnesium phosphate cement (MAP), formed by the reaction between MgO and a soluble phosphate, such as dibasic ammonium phosphate ($\text{NH}_4\text{H}_2\text{PO}_4$). The main phases reported in this cement are struvite ($\text{NH}_4\text{MgPO}_4 \cdot 6\text{H}_2\text{O}$), newberyite ($\text{MgHPO}_4 \cdot 3\text{H}_2\text{O}$), hannayite [$(\text{NH}_4)_2\text{Mg}_3\text{H}_4(\text{PO}_4)_4 \cdot 8\text{H}_2\text{O}$], schertelite [$(\text{NH}_4)_2\text{MgH}_2(\text{PO}_4)_2 \cdot 4\text{H}_2\text{O}$], dittmarite ($\text{NH}_4\text{MgPO}_4 \cdot \text{H}_2\text{O}$), stercorite ($\text{NaNH}_4\text{HPO}_4 \cdot 4\text{H}_2\text{O}$) and struvite-K ($\text{MgKPO}_4 \cdot 6\text{H}_2\text{O}$) (WALLING; PROVIS, 2016). Similarly to what happens to MOC and MOS, the reaction between MgO and phosphoric acid results in a water-soluble cementitious mass, this type of cement has no practical use after ageing.

1.6.4 Magnesium oxide (MgO) and silica (SiO_2) based cements

A different solution becomes possible where Ca chemistry is replaced by Mg, and the cement is produced by combining reactive MgO and highly amorphous SiO_2 to form magnesium silicate hydrate (M-S-H in cement chemistry nomenclature, M: MgO; S: SiO_2 ; H: H_2O) (SZCZERBA et al., 2013; JIN; AL-TABBAA, 2014; LI et al., 2014; ZHANG; VANDEPERRE; CHEESEMAN, 2014; WALLING et al., 2015). Whereas this type of cement historically attracted limited interest, during the last decade it has attracted research interest. In initial studies of this system, a great amount of bonding M-S-H was achieved with satisfactory mechanical properties (JIANGXIONG; YIMIN; YONGXIN, 2006).

Apart from the potentially suitable mechanical performance of this material, the present thesis is mainly interested in a different characteristic, its lower alkalinity ($\text{pH} < 11$) (ZHANG; CHEESEMAN; VANDEPERRE, 2011). In accordance with different studies, after evaluating MgO-

based cements alkalinity, pH values are below 11 before 7 days and around 10 after 14 days. According to the wide collection of studies about fibres degradation processes and the mechanisms that lead to the loss of mechanical properties of the fibres as cement reinforcement, using MgO-based cements provides potential and less aggressive environments than PC, where pH is above 12.5 from the very early stages of hydration.

Another aspect to be considered to protect fibres against environmental humidity variations is the use of lowest permeability matrices. This aim could be achieved by using lower porosity matrices, restricting humidity variations from the outside environment. In this case MgO-based cement seems to have a higher apparent density (KRYSTAFKIEWICZ et al., 2004).

1.7 CLARIFYING REMARKS ABOUT THIS WORK

A MgO and SiO₂ hydraulic binding system is applied in this work in order to assess its real potential to obtain long term durable FRCC completely reinforced with lignocellulosic elements. According to the previous reasons above offered, cellulose-based reinforcing elements in FRCC become a promising option to develop a beneficial technology from an economic, environmental and social point of view. Nonetheless, some clarifying remarks are presented for a better understand the initial intention, possible limitations and solutions for future studies.

1.7.1 Use of reactive MgO from MgCO₃ thermal decomposition

The first point addressed is the calcination process of MgCO₃. MgO used for this work is provided by Magnesita SA, South America's leading producer of dead-burn and caustic-calcined magnesia as well as refractory products. Production of magnesite is almost entirely centred on the deposits around Brumado, located in Brazilian south-western Bahia State. Magnesita has the capacity to produce around 2.7 Mt of unburnt magnesite a year as well as 272,000 tonnes/year of dead-burned magnesite, although current production levels are about 231,000 tonnes per annum. Caustic calcined magnesite output is around 41,000 tonnes per year. The major commercial deposit of crystalline magnesite is in the area of Serra das Éguas, where the magnesite occurs as bladelike aggregates and euhedral crystals. Magnesite also occurs as massive aggregates, which comprises the commercial ore. This ore ranges in colour from white to a red-orange owing to the presence of

a finely divided hematite. The most typical is fine- to medium-grained white or light gray magnesite. The formation of this deposit is thought to have involved magnesium-bearing solutions depositing magnesite as a replacement of dolomite and altering quartz to enstatite and talc (SHAND, 2006).

The essential reaction that occurs during MgCO_3 heating is the loss of carbon dioxide from magnesite, with the corresponding formation of magnesium oxide; see (9). The full decomposition of 1.0 kg of pure magnesite yields 0.48 kg magnesium oxide and 0.52 kg of carbon dioxide. Therefore, it will require 2.08 kg of pure magnesite to yield 1.0 kg of magnesium oxide.

According to SimaPro 8 database, used to calculate impact assessment results:

- Total mining and transport of raw materials related CO_2 emissions = 0.01-0.015 t CO_2 /t MgO
- Total electricity or fuel related CO_2 emissions = 0.13-0.15 t CO_2 /t MgO

Also from stoichiometry, the CO_2 released during calcination process of magnesite to magnesium oxide is approximately 1.09 t CO_2 /t MgO.

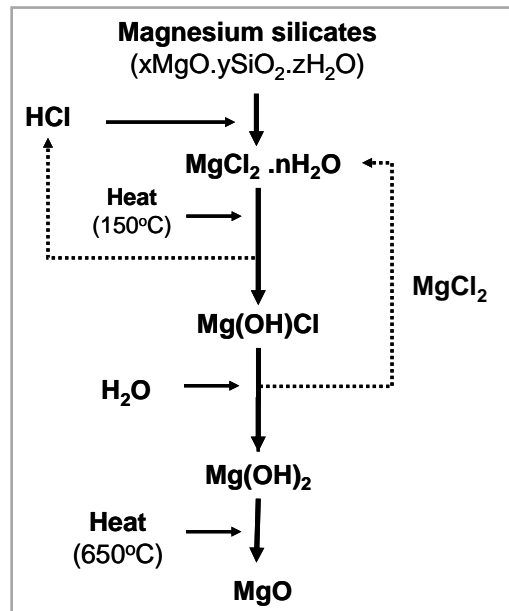
Altogether, a total value of approximately 1.23-1.26 t CO_2 /t MgO are released to the atmosphere.

Comparing CO_2 emission values to those for Portland cement (0.9-1t CO_2 /t MgO) (GARTNER, 2004; BARCELO et al., 2014), MgO production may be considered as more pollutant option. Nevertheless, the proposed binder system is a blend of MgO and SiO_2 based materials that could result in much reduced emission per tonne of binder. According to literature, up to 50% of the binding system may be constituted by SiO_2 additions, which could clearly decrease these CO_2 emission figures.

1.7.2 Lower carbon alternatives for obtaining reactive MgO

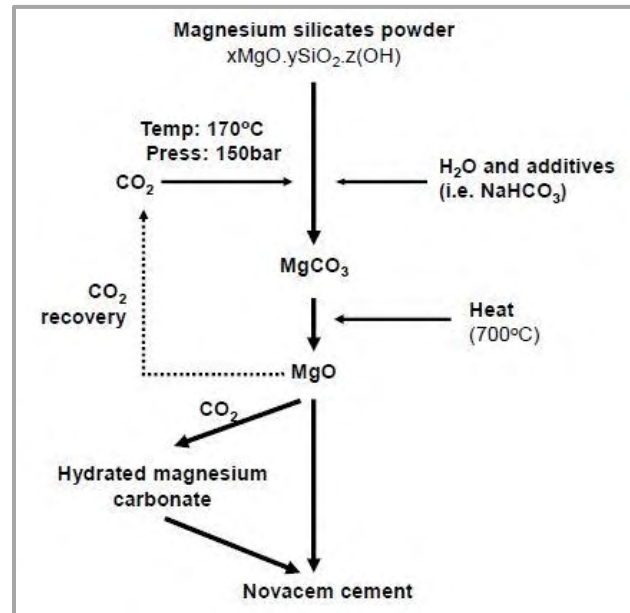
Another route to obtain reactive MgO was proposed two decades ago (LACKNER et al., 1995). It was suggested a new production technology to obtain MgO from magnesium silicates, MS, (Figure 7). In accordance with this process magnesium silicates decomposition does not involve any CO_2 chemical emission and only fuel related emission occurs. Thus, only 0.2-0.4 tonnes of CO_2 are emitted for each tonne of MgO produced, reducing considerably the pollutant effect of MgCO_3 calcination.

Figure 6- Diagram of the process for magnesium oxide production according to (LACKNER et al., 1995)



Source: Based on: LACKNER, K. S. et al. Carbon dioxide disposal in carbonate minerals. **Energy**, London, v. 20, n. 11, p. 1153–1170, 1995.

The production of reactive MgO from MS was also explored by Novacem Ltd. This former Imperial College London spin-out developed several products regarding Mg-based technology. Although the company liquidation in 2012, Novacem left an intellectual property legacy, currently in possession of Calix (Australia), that included an improved process for manufacturing MgCO_3 from MS ores by carbonation (i.e. treatment with carbon dioxide and/or carbonic acid H_2CO_3 at high temperature and pressure) (VLASOPOULOS; BERNEBEU, 2014). Very interesting advantages from this system are obtained since CO_2 is cyclically recovered into the process for raw materials carbonation; see Figure 7. Another positive aspect derived from this process is the low temperature demand that makes viable the use of fuels with low energy content. Novacem claimed to produce carbon negative cement, though it was never industrially upscaled for cement products manufacture. Despite the initial shortcomings of Novacem technology (high pressure demand and high degree of milling to process raw materials), this approach has been pointed out as energy-competitive with PC (GARTNER; HIRAO, 2015), though more research was essential to develop viable Mg-based cement.

Figure 7- Summarized process of MgCO_3 production according to (VLASOPOULOS; BERNEBEU, 2014)

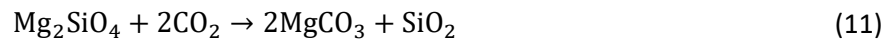
Source: Based on VLASOPOULOS, N.; BERNEBEU, J. P. **Production of magnesium carbonate**. [s.l.]: Google Patents, 2014.

1.7.3 Use of reactive SiO_2

In this work, reactive SiO_2 is obtained from silica fume (SF). This SF is U920, provided by Elkem Materials South America Ltda, Diadema, SP, Brazil. SF is widely reported to be very effective pozzolan material (ZELIĆ et al., 2000; ROY; ARJUNAN; SILSBEE, 2001; WONG; ABDUL RAZAK, 2005). SF, also called microsilica, (CAS number 69012-64-2, EINECS number 273-761-1) is an amorphous (non-crystalline) polymorph of SiO_2 . This spherical shaped mineral, with an average diameter of $0.15\mu\text{m}$, is obtained as a by-product of the silicon and ferrosilicon alloy production. After years of experience, SF is not considered as a waste product any longer and it is widely employed as an essential compound to produced high strength cements. With time, SF price has arisen and it is not an economic option to produce FRCC. However, SF is chosen since its pozzolanic nature is broadly understood as well as its homogeneity facilitates a better reproducibility of laboratory scale tests.

One more interesting aspect to be considered from Novacem technique (Figure 7) is the production of SiO_2 as a by-product from the carbonation process of MS, according to (11). This SiO_2 , when amorphous and finely obtained is the second mineral necessary to produce the previously

mentioned cement based on MgO-SiO₂. Therefore, MgO-SiO₂ cement has a promising route to go follow the initial steps made by this company.



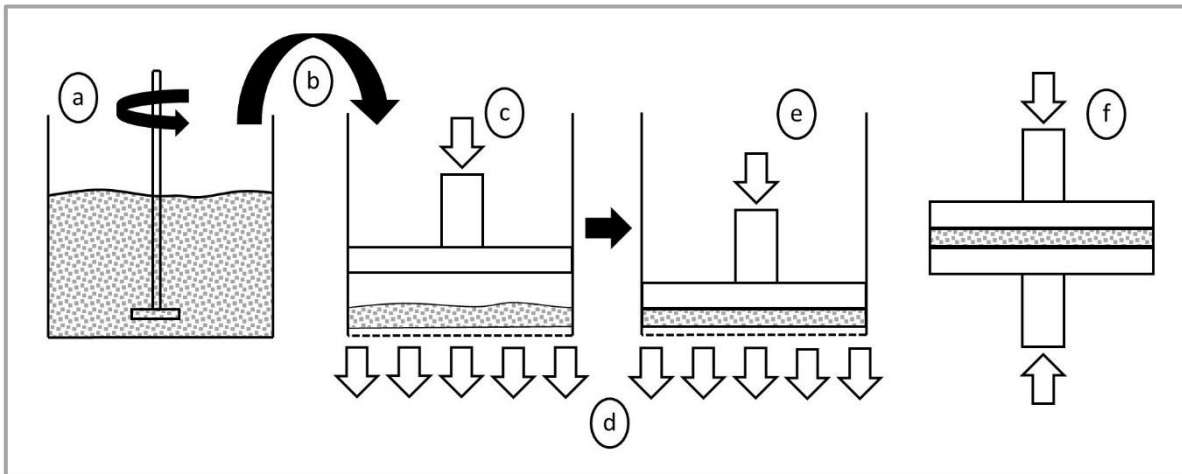
1.7.4 Dewatering-pressing moulding technique (DPM)

In front of all the possibilities given by the use of MgO-SiO₂ and cellulose-based fibres, this thesis focuses on the production of FRCC moulded following a dewatering-pressing moulding, DPM, technique.

Based on the scientific career of the supervisor of this thesis (lattes.cnpq.br/4108663280979993) and his renowned success in introducing cellulose-based elements in FRCC by DPM, this method becomes as the most suitable solution to produce the specimens tested during this work. For a clear assessment of the durability of these composites, the produced FRCC uses only lignocellulosic reinforcement from paper pulping.

This moulding process is an adaptation of the Hatschek process to a laboratory scale, displayed in Figure 8. The Hatschek process involves the production of fibre cement by overlaying thin sheets made of a mixture of cementitious binders, fibres, aggregates and water. Thin sheets of fibre cement are obtained by retention of solid materials during filtration in rotary sieves, which are later transferred and accumulated in a cylindrical press, to obtain the desired thickness. The cellulose fibres have an essential role in this process, since they constitute the network of fibres that trap suspended solids during filtration. The adaptation of the Hatschek process to a DPM has been successfully reproduced and described (DIAS; SAVASTANO JR.; JOHN, 2010). With this adaptation, DPM allows to obtain very thin materials that simplifies the flexural performance analysis of the composites since insignificant compressive contribution of the cement is produced under bending tests.

Figure 8- Scheme of laboratory scale of DPM process. (a) slurry stirring, mixture of cement, fibres and aggregates in water; (b) transfer to a moulding chamber; (c) composite casting; (d) dewatering by vacuum and tamping by low hydraulic pressing ; (e) finished upper surface and (f) composite compaction by high hydraulic pressing



Source: **Own creation**

Considering the hydration reaction of MgO to form Mg(OH)_2 (12), to hydrate 1g of MgO it is needed approximately 0.4467g of H_2O . However, due to the high specific surface area of reactive MgO, more water is required to promote a dissolving-precipitating process until total MgO is hydrated, as well as extra water is required for a minimum flowability in order to assure a good casting. At this point DPM also results favourable since this process introduces an initial extra amount of water for the composite casting and later removes it. In the case of Mg-based materials this is of importance since no additive is required for moulding.



1.8 STRUCTURE OF THE THESIS

The present work is composed of 5 different experimental studies as displayed in Figure 9. Each experimental work is considered as an independent block.

The whole study has been structured in three main experimental stages, as depicted in Figure 9:

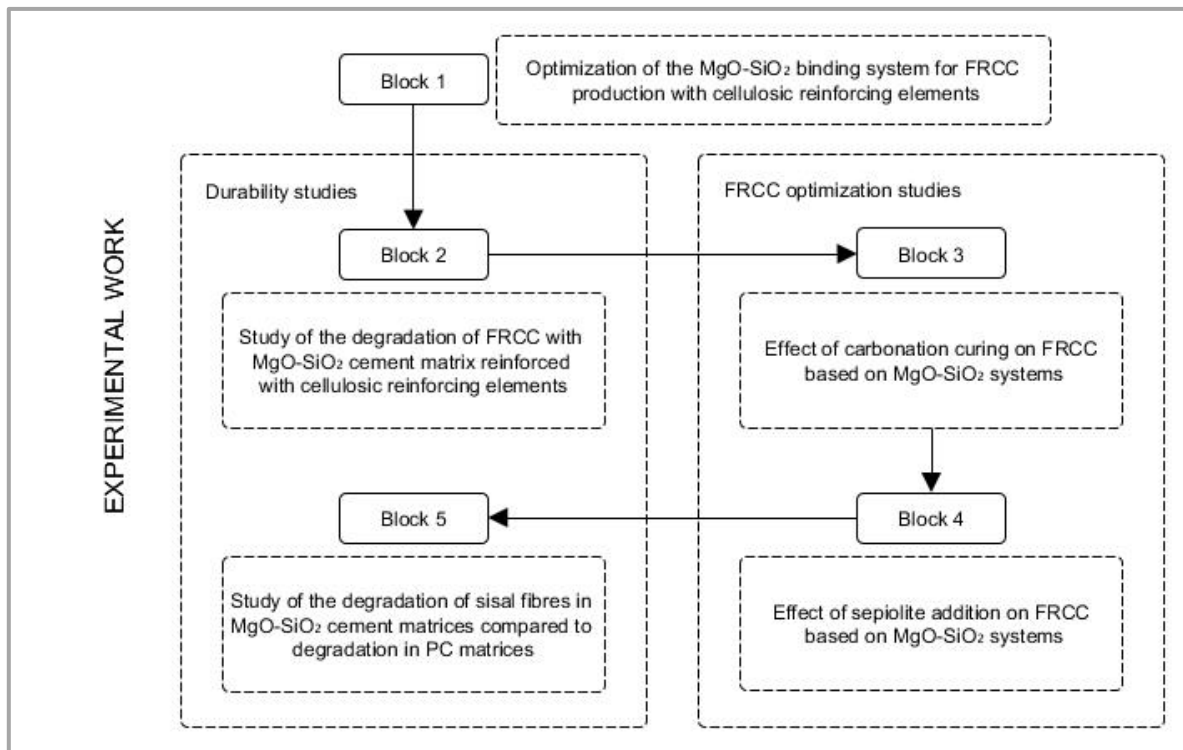
1) Optimization of the MgO-SiO₂ binding system for FRCC production with cellulosic reinforcing elements (Block 1)

2) Durability studies (Block 2 and Block 5). Analysis of the different aspects of the cellulose based reinforcing elements durability. While Block 2 assesses the durability of lignocellulosic elements introduced as pulp to reinforce thin plates, along with the analysis of the composites mechanical performance before and after ageing, Block 5 only focuses on the durability of macrofibres in terms of chemical integrity before and after time when are embedded in cement matrices.

3) FRCC optimization studies (Block 3 and Block 4). Introduction of two different routes to improve MgO-SiO₂ systems: the use of different curing treatments to promote carbonation of Mg hydrates compounds (Block 3) and the incorporation of magnesium silicate hydrates additives to improve composite performance (Block 4).

Part of Block 4 and Block 5 were developed in Spain, at the Department of Chemistry Engineering of Universidad Complutense de Madrid and at the Institute of Materials Technology of Universitat Politècnica de València respectively.

Figure 9- Flowchart representing the workflow of the thesis according the work carried out in the different chapters



Source: Own creation

1.9 AIM OF THE DIFFERENT BLOCKS

1.9.1 BLOCK 1

Optimization of the MgO-SiO₂ binding system for FRCC production with cellulosic reinforcing elements

This block has been adapted from: (MÁRMOL et al., 2016). Every Table and Figure has been adapted from this only source.

A range of MgO and SiO₂ blends mixed with water is analysed to develop clinker-free Fibre Reinforced Cementitious Composites (FRCC) products reinforced with cellulosic fibres. For FRCC production, particularly in the case of fibre-cement products, it is necessary to understand the early properties of the binding matrix, since rapid development of rigidity (in the first week of age) is required during the production and stock process. For this reason, this chapter assesses the hydration evolution from 7 to 28 days of different MgO-SiO₂ formulations simulating the fibre-

cement manufacture conditions. Hence, the optimal dosage by a compromise solution between the lowest alkalinity (from mixing until 28 days) and the highest mechanical performance (at 7 and 28 days) is chosen.

1.9.2 BLOCK 2

Study of the degradation of FRCC with MgO-SiO₂ cement matrix reinforced with cellulosic reinforcing elements

This block has been adapted from: (MÁRMOL; SAVASTANO, 2017). Every Table and Figure has been adapted from this only source.

This block assesses the use of low alkaline composites based on magnesium oxide and silica (MgO-SiO₂) cement and reinforced with cellulose fibres for the production of thin FRCC to resist bending loads. The strategy adopted aims to study the durability of lignocellulosic fibres in a lower pH environment than the ordinary Portland cement (PC) by comparing the flexural performance of samples at 28 days and after 200 accelerated ageing cycles (aac). Furthermore, apparent porosity (AP), bulk density (BD) and water absorption (WA) are assessed both at 28 days and after 200 aac. Two types of vegetable fibres are utilised: eucalyptus and pine pulps.

1.9.3 BLOCK 3

Effect of carbonation curing on FRCC based on MgO-SiO₂ systems

High CO₂ concentration environment is evaluated as a curing treatment in order to optimise Mg-based cementitious matrices in FRCC. Thin FRCC made out of MgO-SiO₂ binding systems and reinforced with polypropylene (PP) and cellulosic (pine) pulp, are produced by a Dewatering Pressing Moulding (DPM) technique are mechanically and physically characterized. Samples are cured under two different conditions: 1) steam water curing at 55°C and 2) a complementary high CO₂ concentration (20% by volume). To evaluate the mechanical performance of the MgO-SiO₂ cement and the possibility to be fibre reinforced, 4 point-bending test is used. In addition, apparent porosity (AP), bulk density (BD) and water absorption (WA) are assessed. In order to study the effects of carbonation on the materials, and their performance over time, cycles of accelerated ageing are used. At this point, PP fibres are introduced along with lignocellulosic fibres in this thesis since they are longer fibres, and therefore yield better energy dispersion by pull-out. Higher energy

dispersion samples facilitate the evaluation of the CO₂ curing treatment and its effects on FRCC. Also the thermodynamic stability of the possible obtained HMC on the matrix is confirmed.

1.9.4 BLOCK 4

Effect of sepiolite addition on FRCC based on MgO-SiO₂ systems

The addition of sepiolite in FRCC is analysed as a possible additive constituent of the binding matrix. With the intention of optimising the Mg-SiO₂ cementitious system in FRCC, small cement replacement (1 and 2% wt.) by sepiolite is introduced in the composites so its effects are studied, firstly, in hardened cement pastes and, later, in FRCC systems. When used only in cement pastes, non-destructive studies are used to assess flexural performance over time as well as the possible reactivity between additive and cement. When sepiolite is introduced in FRCC, the properties of the slurry suspensions are evaluated to understand its interference in the Dewatering Pressing Moulding (DPM) process and, finally, flexural tests are carried out to understand the outcome of this additive on the mechanical performance of the composite.

1.9.5 BLOCK 5

Study of the degradation of sisal fibres in MgO-SiO₂ cement matrices compared to degradation in PC matrices

After proving that cellulose microfibrils do not suffer any chemical degradation, when used in thin FRCC made out of MgO-SiO₂ cement, it becomes essential to understand the behaviour of macrofibrils when submitted to the same conditions. Although this thesis only focuses on the performance of the FRCC produced by DPM, it becomes necessary to evaluate the real potential of all types of cellulosic fibres in order to obtain different types of FRCC, especially those reinforced with longer fibres. In this sense, the comparative study of fibre degradation when applied in different cementitious systems, MgO-SiO₂ and PC, reveals the real compatibility of lignocellulosic fibres and Mg-based cement. Since several authors have broadly used sisal to reinforce PC composites and its deterioration has been well reported, this type of fibre has been selected to assess its integrity over time in MgO-SiO₂ systems.

2 LITERATURE REVIEW

The use of lignocellulosic fibres in FRCC was proposed ever since the production of asbestos-free fibre-cement became a key challenge from a technical point of view (COUTTS, 2005). At present, necessity for new fibre cement technologies is increasing to attend the huge demand that exists in both developing countries and more industrialized areas. It has increasingly become a very interesting material as reinforcement element for FRCCs, e.g. flat sheets, roofing and siding shingles, and clapboards, due to their excellent mechanical properties (ARDANUY; CLARAMUNT; TOLEDO FILHO, 2015). Many other types of fibres present a remarkable potential as reinforcement elements in cementitious products i.e. carbon (BAEZA et al., 2013; SHU et al., 2015), synthetic polymers (HAN et al., 2012), rubber (GUPTA; CHAUDHARY; SHARMA, 2016), glass fibre reinforced plastic (ASOKAN; OSMANI; PRICE, 2009) or steel (MADANDOUST et al., 2015; SENARATNE et al., 2016). In spite of their suitable properties, these synthetic fibres introduce an extra cost in the production of FRCC and likewise are not the best option from an environmental point of view (TONOLI et al., 2010). On the other hand, lignocellulosic fibres, when used with Portland cement, undergo alkaline degradation leading to deterioration in flexural properties over time. Vegetable fibres can suffer various degrees of degradation when exposed to an alkaline environment and this degradation is especially manifested when fibres are exposed to alkaline environments which are also rich in Ca^{2+} (TOLEDO FILHO et al., 2000).

The degradation of lignocellulosic fibres is thoroughly described (MELO FILHO; SILVA; TOLEDO FILHO, 2013), though the mechanism of degradation becomes difficult to establish since it includes three combined factors on the deterioration of sisal fibre (WEI; MEYER, 2014):

- (i) Alkaline pore water, from cement hydration, dissolves the amorphous materials of fibre, such as waxes, fats, hemicelluloses and lignin, which are susceptible to both $\text{Ca}(\text{OH})_2$ and high alkalinity attack and can be disintegrated in alkali environment. This declines the linkage between individual fibre cells, leading to the decrease of tensile strength;
- (ii) alkaline hydrolysis of cellulose molecules, which generates a rupture between molecular chains and so a reduction in degree of polymerization and lower tensile strength, since the strength of fibre mainly depends on the content of crystalline cellulose; and

- (iii) crystallization of lime in the lumen, walls of the individual fibres and middle lamellae yielding a reduction in the fibre flexibility and strength, which is also known as fibre mineralization process.

Many attempts to solve this inconvenience have been explored effectively, improving fibre integrity after ageing, although far from achieving a completely successful solution. So far, all the techniques used to improve vegetable fibre durability in Portland cement are based on the reduction of portlandite, by the use of highly reactive pozzolans (BEZERRA et al., 2006; MÁRMOL et al., 2013; PEREIRA et al., 2013) and carbonation (ALMEIDA et al., 2013; PIZZOL et al., 2014; SANTOS et al., 2015a). However, these methods rely on chemical reactions which take place gradually rather than immediately, and this means that the vegetable fibres are surrounded by high concentrations of Ca(OH)_2 in the initial stages, which may be deleterious for reinforcing performance (TOLEDO FILHO et al., 2000).

A different solution becomes possible where Ca chemistry is replaced by Mg, and the cement is produced by combining reactive MgO and highly amorphous SiO_2 to form magnesium silicate hydrate (M-S-H in cement chemistry nomenclature, M: MgO; S: SiO_2 ; H: H_2O) (SANDBERG; MOSBERG, 1989). In initial studies of this system, a great amount of bonding M-S-H is achieved with satisfactory mechanical properties (SANDBERG; MOSBERG, 1989). Whereas this type of cement historically attracted limited interest, during the last decade it has become an attractive alternative to Portland cement due to its properties: low alkalinity ($\text{pH} < 11$) (ZHANG; CHEESEMAN; VANDEPERRE, 2011; WALLING et al., 2015) and potentially good mechanical performance (JIANGXIONG; YIMIN; YONGXIN, 2006; ZHANG; VANDEPERRE; CHEESEMAN, 2014).

The better understanding of this new fibre-cement product is crucial for the manufacture of more sustainable building materials since cellulosic fibres are biodegradable, renewable, demand low processing energy and are available around the world at lower rates with diversity of morphologies and dimensions (SANTOS et al., 2015b). In addition, MgO- SiO_2 cements assessed in this thesis, in contrast to Portland cement, which requires high temperatures (about 1450°C) during its production, demand less energy [750°C is the maximum temperature for the controlled calcination to obtain reactive MgO from MgCO_3 (SHAND, 2006)]. This alternative cement, would also allow the reuse of agro-industrial residues in to obtain amorphous silica (ANTIOHOS; PAPADAKIS; TSIMAS, 2014), becoming a more efficient cement from the environmental point of view.

New types of cement as magnesium oxysulfate (MOS) cements have been successfully used to prevent cellulosic fibres degradation over time (GOMES; CAMARINI, 2014). However, the mechanical results of this new kind of cement are far from those obtained with Portland cement products. Besides MOS cement is known to have leaching problems with time (SHAND, 2006). A new type of magnesia cement is presented for the production of FRCC elements from the combination of MgO and reactive SiO₂ (MgO-SiO₂ cement).

Accelerated carbonation has been shown to be capable of improving cementitious matrices for fibre cement applications (ALMEIDA et al., 2013; PURNELL; SHORT; PAGE, 2001; PURNELL et al., 2003; PIZZOL et al., 2014; SANTOS et al., 2015a). The main effect of carbonation on hydrated Portland cement paste is the conversion of portlandite (Ca(OH)₂) into calcite (CaCO₃). This reaction increases the density of the matrix, (FRÍAS; GOÑI, 2013; MO; ZHANG; DENG, 2015; MORANDEAU; THIÉRY; DANGLA, 2015; ZHA et al., 2015), making it more rigid and stronger. It also strengthens the fibre-matrix interface, but this can modify the fracture mechanism, often leading to a reduction in the energy absorbed during a flexural test, despite significant increases in the modulus of rupture (MOR) and modulus of elasticity (MOE) (PURNELL; SHORT; PAGE, 2001; ALMEIDA et al., 2013; PIZZOL et al., 2014; SANTOS et al., 2015a).

Reactive periclase binders can also harden by carbonation, sequestering CO₂ as part of the process of making construction materials (UNLUER; AL-TABBAA, 2013, 2014, 2015; VANDEPERRE; AL-TABBAA, 2007). When MgO is carbonated in the presence of water, HMC are produced, with general formula $x\text{MgCO}_3 \cdot \text{Mg}(\text{OH})_2 \cdot y\text{H}_2\text{O}$, (HMC) (BOTHAS; STRYDOM, 2001; LANAS; ALVAREZ, 2004). These compounds bind both water and CO₂ and thus create a very large additional solid volume, giving them a much greater potential than Portland cement in terms of overall binder efficiency. The transformation of brucite into HMC, identically to what occurs for Ca(OH)₂ when turns into (CaCO₃), increases strength of the hydrated pastes.

One more particular benefit for carbonating MgO cements is the higher water demand of this types of cements compared to Portland cement (ZHANG; VANDEPERRE; CHEESEMAN, 2014). This higher water demand implies a more porous matrix and therefore facilitates the transportation of CO₂ through the matrix. In addition to generating porous matrices, the high water demand of MgO cements also creates favorable conditions for the carbonation of Mg(OH)₂ since a previous requirement for the formation of HMC is the dissolution of CO₂ in water to form carbonic acid (H₂CO₃) (VANDEPERRE; AL-TABBAA, 2007). This factor has to be considered in the production of

fibre-cement as the possible addition of cellulosic fibres would increase the amount of water within the matrix after reinforcement dry due to the hygroscopic nature of vegetal fibres (ONUAGULUCHI; BANTHIA, 2016). The release of water from vegetable fibres would increase the capillary water, favouring the generation of H_2CO_3 and promoting carbonation.

Another aspect to be analysed is the condition for carbonation to be effective. Up to now the best results to accelerate carbonation on Portland cement are those achieved by supercritical carbonation (PURNELL; SHORT; PAGE, 2001; SANTOS et al., 2015a). From a technical point of view, supercritical carbonation requires high energy to reach the critical point (pressure of at least 7.38 MPa) as well as additional sophisticated chambers to resist those reactor conditions. However, for HMC, it is not necessary supercritical fluids for carbonation in order to accelerate the carbonation reaction. This factor makes feasible the production of carbonated products with simpler technologies that exclusively require higher concentration of CO_2 .

Although all the mentioned advantages of carbonating MgO-SiO₂ systems, a debate has been settled recently regarding the thermodynamic stability of the produced phases as a consequence of carbonation (UNLUER; AL-TABBAA, 2013, 2016; WALLING; PROVIS, 2016). This factor requires a special attention and discussion to determine the viability of this new type of cement to be reinforced with cellulosic reinforcements.

Sepiolite is a clay with a very characteristic fibrous structure with an empirical formula of $Si_6Mg_4O_{15}(OH)_2 \cdot 6H_2O$. This mineral has a wide range of uses due to its sorptive, optical, rheological and molecular sieve properties. In cementitious materials, sepiolite is usually utilized as a rheological additive to enhance their features in both the fresh and the hardened state. Sepiolite has a thixotropic character improving workability, adherence to the substrate, pumpability and surface finishing (ÁLVAREZ et al., 2011). In the case of fibre-cement products, the use of this additive has a significant effect as rheological agent. The modification of the rheological properties of the fibre-cement suspensions entails better fibre distribution and better fine particles retention (FUENTE et al., 2010). Besides, when sepiolite is used in the fabrication of Portland cement products reinforced with cellulosic fibres, it enhances interlaminar bonding of the sheets, promotes an excellent surface finishing and presents a good compatibility with flocculants of different ionic charge and molecular weight (FUENTE et al., 2010; JARABO et al., 2010).

The use of sepiolite for fibre-cement applications depends on its surface anionic charge. The higher anionic charge affects cement hydration by reducing the extent of oxygen atoms in the

sepiolite surface with free pairs of electrons to interact with water through hydrogen bonding (JARABO et al., 2014). The dispersion of sepiolite in fibre-cement is favoured by reducing the anionic charge of this material (JARABO et al., 2014). Dispersion of sepiolite is, therefore, related to the efficiency as rheological agent and as well as inhibitor of expansion cracks (JARABO et al., 2014). When a moderate-to-low anionic charge surface sepiolite is added in fibre-cement suspensions flexural properties are improved (modulus of rupture, limit of proportionality and specific energy). However this enhancement is not reflected on an improvement of the physical properties (density, porosity and water absorption) (JARABO et al., 2014). Sepiolite in fibre-cement increases the stability of the flocs. Besides the higher grade of flocculation of the small particles makes easier the flow of water through the spaces among the flocs (FUENTE et al., 2010). Sepiolite, when present in fibre-cement suspensions, competes with the rest of the components (cellulose mainly) to absorb flocculant (A-PAM), increasing the flocculation efficiency in terms of chord size and stability of the flocs (JARABO et al., 2010). Likewise, when sepiolite is dispersed in water either with cement or silica also improves flocculation by interacting with the flocculant particles (JARABO et al., 2010).

Apart from its rheological properties, this clay is also used to reinforce cementitious materials due to its morphology. It is found that the addition of 10% sepiolite fibres enhances the mechanical properties of the mortar (compressive and bending strengths) compared to the plain Portland cement samples (KAVAS; SABAH; ÇELİK, 2004). Because of its needle-like shape, with a length of 0.2-2.0 mm, a width of 100-300 Å and a thickness of 50-100 Å, within a cement matrix, sepiolite fibres fill the pores in the paste. It is also proved that an optimal fibre distribution is necessary for a proper linkage of the fibres in the cement matrix (KAVAS; SABAH; ÇELİK, 2004). Also, because of the short length and the random distribution of its microfibrils, it has a beneficial effect to reduce crack width and crack length and shrinkage cracking (KANG; SONG; KIM, 2008) and decrease soundness (expansion volume) and leads to a reduced shrinkage (KAVAS; SABAH; ÇELİK, 2004).

In the case of MgO-SiO₂ FRCC with cellulosic materials, all these properties are required. Moreover, sepiolite has been used in lime mortars due to its absorption properties to act as a water reservoir in conditions of low humidity (ANDREJKOVIČOVÁ et al., 2012) which could be advantageous to complete hydration of MgO-SiO₂ systems that demand higher amounts of water compared to Portland cement. In addition, in lime mortars, this mineral addition promotes interlocking of mortar components, producing a denser structure and, therefore, improves the

mechanical properties at later ages. Since one of the main hydration products of MgO-SiO₂-H₂O systems, poorly crystalized magnesium silicate hydrate, has the same chemical composition as sepiolite, it is expected to create new nucleation links between sepiolite and M-S-H gels. When lime mortars are improved by the addition of a pozzolan, particularly metakaolin, in addition to improving mechanical properties at later ages, adding sepiolite provides a wet environment for metakaolin, favoring the pozzolanic activity (ANDREJKOVICÔVÁ, 2011). This reactivity could be greater in an Mg rich environment provided during the hydration of MgO-SiO₂ systems.

3 MATERIALS AND METHODS

3.1 BLOCK 1

This work is structured in two different sections. The first step aims to analyze MgO-SiO₂ systems with different formulations and their hydration reactions in the early stages. The second stage intends to select the optimal blended system for fibre-cement production according to the results of pH and mechanical performance.

The main target is obtaining hydrated magnesium silicates (M-S-H) gels, intending to obtain hydration products analogous to those achieved from dicalcium silicate (C₂S) and tricalcium silicate (C₃S) hydration, but using magnesium chemistry instead of calcium.

3.1.1 Materials preparation and characterization

To achieve this objective, pastes made of a blend of fine powders acted as clinker-free cement. The two components of this blended cement are reactive magnesium oxide powder, [Q-MAG-200-AR (AR200)], obtained by controlled calcination of MgCO₃ and provided by Magnesita S.A., Contagem, MG, Brazil, and undensified microsilica powder type 920U with high content of silicon dioxide with a typical bulk density of 200-350 kg/m³, provided by Elkem ASA Materials, Sao Paulo, SP, Brazil. Before mixing with water, ball milling for powder homogenization is carried out at a ball to powder ratio of 2:1 at 1 rpm. The basic properties of these materials are shown in Table 3.

Table 3- Properties of the raw materials used to produce the blended samples

	MgO AR200	SiO ₂ 920U
Chemical composition (wt.%)		
MgO	97.4	0.33
SiO ₂	0.1	95.1
Al ₂ O ₃	<0.10	<0.10
Fe ₂ O ₃	0.34	0.35
CaO	0.81	0.25
TiO ₂	<0.10	<0.10
K ₂ O	<0.10	0.91
Na ₂ O	<0.10	0.26
LOI	1.6	1.7
Specific gravity (g/cm ³)		
	3.5	2.3
Particle size		
D ₁₀ (μm)	7.11	11.41
D ₅₀ (μm)	17.41	19.02
D ₉₀ (μm)	64.64	36.99
Surface area (m ² /g)		
	22.7	16.1

Source: **Own creation**

The initial MgO to SiO₂ ratios are analysed according to Table 4.

Table 4- Different MgO and SiO₂ blends analysed in this block

MgO (wt.%)	SiO ₂ (wt.%)
50	50
60	40
70	30
80	20

Source: **Own creation**

As a control cement matrix, High Early Strength Portland Cement is used (CPV-ARI, according to Brazilian Standards NBR 5733) to compare the pH and compressive strength results. CPV-ARI is selected because it is mainly constituted of clinker with no mineral additions. This condition is desirable to set a baseline for the comparative tests here, since in the case of mineral additions being present a pozzolanic reaction may take place. This may generate a less aggressive environment for lignocellulosic fibres due to the reduction of the portlandite and pH.

3.1.2 Test methods

The evolution of pH over time is measured following the procedures of previous studies (ZHANG; CHEESEMAN; VANDEPERRE, 2011). 10 g of blended powders according to the formulations shown in Table 4 are poured into sealed glass beakers containing 100 mL of deionized water, and stirred. The temperature is kept constant at 30°C. pH measurements are taken 30 min after mixing the powders in water, then at 1, 7, 14, 21 and 28 days. For pH measurements a Digimed DM-23 pHmeter, an Ika HS10 magnetic stirrer and an Ika ETS-D5 digital temperature controller are used.

One of the criteria to select the best formulation is mechanical performance. In spite of the need for a good flexural resistant fibre-cement product, the value that represents cement strength in a more reliable manner is compressive strength. An adaptation of standardized mortar tests (ASTM C780-14, 2014) for application to pastes is taken in order to use materials in a more efficient way as a lower amount of material is required to achieve consistent results. For every sample, including Portland cement pastes, the water to binder ratio is held constant at 0.50 in order to compare mechanical results regardless of water demand. For that purpose, plasticizer (Melflux 2651F provided by Sika) is added to the samples for binary systems. Axial compressive strength is measured at 7 and 28 days (6 replicate cylindrical test samples, 50mm high x 25mm diameter, per curing time), performing the test with a 50 kN cell load and a swivel device for a uniform approach to the upper side of the samples. The deformation rate is 0.3 mm/min. The samples are cured in a sealed bag and kept in a 95% humidity box. After compressive strength testing, samples are crushed into powder and immersed in acetone for 5 days and then dried at 65°C until constant mass. Then, only particles through a 63µm size mesh were considered for testing. Hydration is also stopped for bigger pieces. Fragments of around 5mm length are embedded in epoxy resin mixed in a 7:1 resin to hardener ratio and, after hardening, polished with different grit size (9, 3 and 1 µm respectively) silicon carbide pads for 6 minutes at 300rpm and 10N·m.

Mineralogical analysis by means of X-ray diffraction (XRD) is carried out using powder samples, using an X-ray diffractometer Horiba LA-960, scanning between 5-65° 2θ at 10 °/min. Rietveld analysis is performed using PDXL-2 software. Thermogravimetry tests (TG) are conducted with a Netzch STA 440 F3 Jupiter instrument in alumina crucibles under atmosphere of nitrogen set at a flow rate of 60 mL/min, from 25 to 1000 °C at a heating rate of 10 °C/min. In order to replicate and characterize the expected M-S-H gel, a gel with a Mg/Si molar ratio of 0.50 is synthesized via a precipitation method according to prior work (BREW; GLASSER, 2005; ZHANG; VANDEPERRE;

CHEESEMAN, 2014) using solutions of sodium metasilicate pentahydrate ($\text{Na}_2\text{SiO}_3 \cdot 5\text{H}_2\text{O}$) and magnesium nitrate hexahydrate ($\text{Mg}(\text{NO}_3)_2 \cdot 6\text{H}_2\text{O}$). This gel is used as a thermogravimetric reference, with a low Mg content to avoid $\text{Mg}(\text{OH})_2$ contamination via an excess of Mg during the precipitation.

For infrared spectroscopy a NEXUS 670 spectrometer from Nicolet Instrument Corporation is used, observing wavenumbers between 4000 and 400 cm^{-1} . Scanning electron microscopy (SEM) images are collected with a Hitachi TM3000 microscope, and EDS measurements are conducted with a SwiftED3000, Oxford Instruments. The acceleration voltage used for the SEM analysis is 15 kV.

3.2 BLOCK 2

3.2.1 Materials preparation and characterization

An cement matrix (MgO-SiO_2 cement) to PC is produced using 60 wt% lightly burned magnesium oxide (MgO) and 40wt% silica fume (SF), based on Block 1 results. In order to compare results with a reference material, Brazilian ordinary Portland cement (PC) CPV-ARI (high early strength), equivalent to Type I as defined in ASTM-C150 (ASTM C150/C150M, 2012) is chosen because of its finer particle size and higher reactivity in comparison to other blended cements available in the Brazilian market, apart from the absence of mineral additions. This condition is desirable since in case of mineral addition present in the matrix, a pozzolanic reaction may take place. This would generate a less aggressive environment for the fibres due to the reduction of the portlandite and pH. Following the procedure of fibre-cement industry, the cementitious material is replaced in 25% by mass of Itaú limestone, produced by Votorantim Cimentos (Santa Helena, SP, Brazil). Powder materials properties are summarized in Table 5. This replacement is carried out in order to reduce the cost of fibre-cement production and improve dimension stability generated by high shrinkage levels due to an excess of cement. For the production of the FRCC, considering the most common pulps used by paper industry in Brazil, two different types of fibres are used: Unbleached Pine pulp, provided by OJSC Solombala Pulp-and-Paper Mill, Arkhangelsk, Russia, and Bleached Eucalyptus pulp, provided by Fibria, Jacarei, SP, Brazil. Chemical characterization is shown in Table 6 and fibre length and width distribution is presented in

Figure 10. In both cases, vegetable fibres are presented in dry laminar sheets with approximately 5% RH. In order to obtain the fibres, after 48 h in water immersion, it is necessary to disintegrate them by stirring in water for 25 min using a cellulosic pulp mixer Tedemix MRF31450.

Table 5- Chemical characterization and particle size parameters of the raw materials used for the matrix formulation of the composites

	MgO	SiO ₂	PC CPVARI	Limestone
X-ray fluorescence chemical analysis (% by mass)				
MgO	97.40	0.33	3.13	3.04
SiO ₂	0.10	95.10	19.4	1.7
Al ₂ O ₃	<0.10	<0.10	4.11	0.21
Fe ₂ O ₃	0.34	0.35	2.3	0.17
CaO	0.81	0.25	63.5	51.7
TiO ₂	<0.10	<0.10	-	0.03
K ₂ O	<0.10	0.91	1.09	0.09
Na ₂ O	<0.10	0.26	0.24	0.01
LOI	1.60	1.70	3.29	43.05
Nominal particle size				
D ₁₀ * (μm)	7.11	11.41	4.97	6.42
D ₅₀ * (μm)	17.41	19.02	11.88	20.10
D ₉₀ * (μm)	64.64	36.99	27.79	64.03

*Loss on Ignition

**D10, D50, D90 are values of the dimensions of the particles at 10, 50 and 90% in the cumulative distribution.

Source: **Own creation**

Table 6- Chemical composition of the cellulosic pulps

Type of fibre	Chemical composition (%)			
	Cellulose	Hemicellulose	Lignin	Others
Eucalyptus (bleached)	85.70	7.21	0.24	6.85
Pine (unbleached)	82.55	8.39	1.73	7.33

Source: **Own creation**

Cellulose fibres are refined in order to obtain a better malleability, fibrillate the fibre surface and develop a good adhesion with cementitious matrix and higher flexural strength of the composites (COUTTS, 2005; TONOLI et al., 2010). The CSF test is a widely accepted standard measure of the drainage properties of pulp suspensions and it relates well to the initial drainage rate of the wet pulp pad during the dewatering process. It is considered the higher the CSF values the lower the refining level of the pulp. Pulps in water slurry (25 g / L) are processed in a flat disks refiner Bruno, model 2RA-12, until a Canadian Standard Freeness (CSF) value of 573 for bleached eucalyptus and 36 for unbleached pine. CSF values are determined after each refining level following TAPPI T 227 om-99 (TAPPI 1999) Standard. Fibre size characterization (

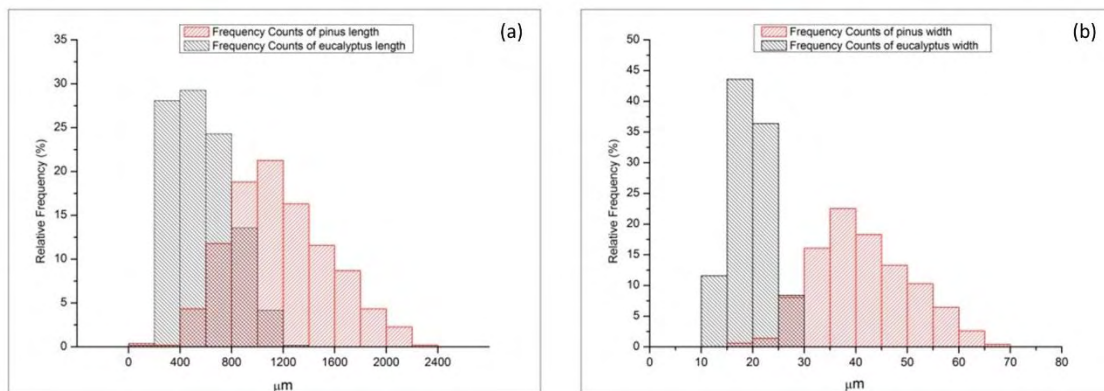
Figure 10) is carried out by an adaptation of the TAPPI T271 Standard, where an optical microscope (Axio Lab.A1) and software (AxioVision) are used to capture and measure the fibre dimensions respectively.

Table 7- Formulation of the FRCC samples used in Block 2 tests

Raw material Content (% by mass)	
PC or MgO-SiO ₂	69
Limestone filler	23
Bleached eucalyptus / Unbleached pine pulp	8

Source: **Own creation**

Figure 10- Histogram of the length (a) and width (b) distribution for both types of pulp reinforcement. Grey bars stand for pine and black bars stand for eucalyptus



Source: **Own creation**

3.2.2 Composites formulation and preparation

FRCC (flat pads) measuring 200 mm x 200 mm and an thickness of around 6-mm are produced at laboratory scale using slurry DPM process, as described in details by Savastano et al. (SAVASTANO JR.; WARDEN; COUTTS, 2000). DPM technique is schematically displayed in Figure 8, where 330 g of dry solid materials following the composition established in

Table 7 are mixed in 1500ml of water at 3000rpm , Figure 8 (a), and then transferred to a casting box (b) are 0.5MPa compacting pressure is applied (c) and after vacuum drainage (550mm Hg) for 2min (d). Once most of the water is removed and flat surfaces are achieved (e), the thin sheets are placed between steel plates and 3MPa compacting pressure is applied for 5min (f).

The different water to binder ratios achieved for each formulation are shown in Table 8. Pads are wet cut into four 165 mm × 40 mm flexural test specimens using a water-cooled diamond saw.

3.2.3 Test methods

4 point bending tests are performed after curing and ageing using a testing machine EMIC DL 3000 equipped with 1 kN load cell and a deflectometer. The deflection values are divided by the major span (135 mm) of the bending test, and considers (ϵ) as specific deflection. Four-point bending configuration is employed to determine the different flexural properties with a deflection speed of 5mm/min.

Table 8- Water to matrix ratio and water to binder ratio after pressing process of every formulation for both types of reinforcement

	Type of binder			
	MgO + SiO ₂		PC	
	Type of pulp			
	Unbleached	Bleached	Unbleached	Bleached
Water to binder ratio after pressing	0.60	0.53	0.45	0.35

Source: **Own creation**

Four-point bending configuration is utilized to determine (MÁRMOL et al., 2013):

Modulus of rupture (MOR)

$$\text{MOR} = \frac{P_{\text{máx}} \cdot L}{b \cdot h^2}$$

Limit of proportionality (LOP)

$$\text{LOP} = \frac{P_{\text{LOP}} \cdot L}{b \cdot h^2}$$

Modulus of elasticity (MOE)

$$\text{MOE} = \frac{276 \cdot L^3}{1296 \cdot b \cdot h^3} \cdot m$$

Specific energy (SE)

$$\text{SE} = \frac{\int F \cdot d\epsilon}{b \cdot h}$$

Where:

- P_{LOP} is the maximum load applied in the elastic region i.e. in linear portion of the load

- P_{max} is the maximum load applied
- L is the major span between supports
- b is the width of the sample
- h is the thickness of the sample
- m is the tangent of the slope angle of the load vs. deflection plotting in the elastic behaviour
- ϵ is deformation registered

Samples are kept immersed in water for saturated curing at 25°C until 28 days of age. After controlled curing until the age of 28 days, the composites are exposed to accelerated aging cycles. The accelerated aging cycles aims to speed up natural weathering using soaking and drying cycles, which allows a better understanding of the long-term behaviour of the composites. Specimens are successively immersed into water at $20 \pm 5^\circ\text{C}$ for 170 min and, after an interval of 10min, they are heated to the temperature of $60 \pm 5^\circ\text{C}$ for 170 min in a ventilated oven. Another interval of 10 min at room temperature also preceded the subsequent cycle, as recommended by the EN 494:2012 Standard (EN 494:2012+A1:2015, 2012). Each cycle finished when one soak and dry is completed and the samples are submitted to 200 accelerated aging cycles

The physical properties, bulk density (BD) and water absorption (WA) are obtained following procedures specified by the ASTM C 948 Standard (1981). The polished (previously embedded in cold-setting resin with the same procedured used in Block 1 section 3.1.1) and fractured surfaces of specimens resulting from the mechanical tests are examined by scanning electron microscope (SEM) with Energy-Dispersive X-ray Spectroscopy (EDS), using Quanta 600 FEG (FEI, Eindhoven, the Netherlands) with an acceleration voltage 15 kV.

3.3 BLOCK 3

3.3.1 Materials preparation and characterization

As previously applied in Block 2, MgO-SiO₂ cement is used as a blend of lightly burned MgO (60%) and silica fume (40%) based on Block 1 results or (MÁRMOL et al., 2016). Based on Block 2, section 3.2.2, the cementitious material is replaced in 25% by mass using ground limestone, Itaú produced by Votorantim Cimentos (Santa Helena, SP, Brazil). The properties of MgO, SiO₂ and limestone used in this research are identical as used in Block 2, section 3.2.1. With the intention of

reproducing the conditions used by fibre-cement industry, similar mix design is used. As reinforcing elements both synthetic and vegetable polymeric reinforcements are used. Synthetic reinforcement concentration is of 2% by mass of the composite (5.82% by volume). In this study polypropylene (PP) fibres (H 216, Braskem, with a density of $0.905 \text{ g}\cdot\text{cm}^{-3}$, a flexural modulus -1% secant- of 1.4GPa, tensile strength of 36MPa and elongation at break of 9%) are used to evaluate their capacity as alternative reinforcement to polyvinyl alcohol (PVA) fibres. The use of synthetic fibres in this study is due to the length of this type of fibres (around 10 mm). Using longer fibres assures enough anchorage in case of deficient matrix-fibre adherence. Pine pulp described in Block 2, section 3.2.1 is used. Refinement is used to change the morphological properties of the cellulose pulp for a better capture of the mineral particles during the drainage of excess water from the pad under formation in the Hatschek process, improving the adherence of the fibres with the matrix (TONOLI et al., 2009a).

The formulation of the composites is chosen with the intention of reproducing the proportions usually utilized by the fibre-cement industry as shown in Table 9.

Table 9- Formulation of the FRCC samples used in Block 3 tests

	Raw materials	Amount (% by mass)
Matrix	Magnesium oxide AR 200	42
	Silica Fume Elkem U920	28
	Limestone Itaú	25
Cellulosic pulp	Unbleached pine pulp (CSF = 36)	3
Synthetic fibre	Polypropylene	2

Source: **Own creation**

Samples for bending and physical tests are produced according to Block 2, section 3.2.3.

3.3.2 Curing treatments

According to Szczerba et al. (2013), $\text{MgO-SiO}_2\text{-H}_2\text{O}$ systems are highly influenced by curing temperature, where hydration reactions are accelerated at temperatures over 30°C . Then, after initial curing at 25°C for 24 h in a sealed plastic bag, water steam curing at 55°C for 7 days is applied (Figure 11). For carbonation curing, after first 24 h, samples are placed in an environmental chamber (ESPEC-brand, EPL-4H model) for 48 h with a CO_2 concentration of 20% by volume, keeping RH at 90% and temperature at 45°C (Figure 11). This temperature is chosen as higher temperatures

accelerate the hydration kinetics and consequently would obstruct the diffusion of CO₂. After the carbonation cycle, a period of 5 days of steam curing at 55°C is carried out (Figure 11). After the steam curing for both carbonated and non-carbonated samples, specimens are kept in water for 48 h to complete saturation for wet flexural and physical tests.

Figure 11- Curing conditions diagram for non-carbonated and carbonated samples

		Condition		
		Water steam saturated environment at 25°C		
		Water steam curing at 55°C		
		20% CO ₂ concentration at 45°C and 90% of RH		
Non carbonated	Period (h)	24	168	
	Condition	[Bar chart showing 24h in light grey, 168h in dark grey]		
Carbonated	Period (h)	24	48	120
	Condition	[Bar chart showing 24h in light grey, 48h in dark grey, 120h in medium grey]		

Source: **Own creation**

3.3.3 Ageing treatment

Accelerated cycles are used to evaluate the composites performance after ageing. This technique aims to speed up natural weathering using soaking and drying cycles. Accelerated ageing cycles are described in Block 2, section 3.2.3. Each cycle finishes when one soak and dry is completed and the samples are submitted to 100 accelerated aging cycles. This ageing treatment is used to submit samples to extreme weathering conditions evaluate thermodynamic stability of HMC.

3.3.4 Test methods

Four point bending tests are performed according to Block 2, section 3.2.3. After mechanical testing, aliquots of each sample are crushed and immersed in acetone to stop hydration reactions and later dried at 60°C. Crushed samples are prepared as described in Block 1, section 3.1.1, to perform X-ray diffraction and thermogravimetric characterization at different ages. X-ray diffractometer Horiba LA-960 (CuK_α radiation at a voltage of 40 kV and a current of 30 mA, between 5-65° with a speed of 10°/min) and a Netzch STA 440 F3 Jupiter TG equipment under an inert atmosphere of nitrogen set at a flow rate of 60 mL/min and performed from 25 to 1000°C at a

heating rate of 10°C/min. The physical properties, bulk density (BD) and water absorption (WA) are obtained following procedures specified by the ASTM C 1185 Standards (2012)(ASTM C1185-08, 2012). The fractured surfaces of specimens resulting from the mechanical tests are resin coated as described in Block 1 and examined by backscattered electron microscopy (SEM) and Scanning Electron Microscopy with X-ray microanalysis (EDS), using Quanta 600 FEG (FEI, Eindhoven, the Netherlands) with an acceleration voltage of 15 kV.

3.4 BLOCK 4

3.4.1 Materials preparation and characterization

In the present work, two types of cement systems are studied: Portland Cement (CEM I meeting EN 197–1:2000 Standard) and the MgO-SiO₂ cement employed in Block 2, Block 3 or (MÁRMOL et al., 2016). Limestone filler (CaCO₃) is also used in the compositions for flocculation study to recreate analogous conditions as used in Block 2 and Block 3. The two types of sepiolite used in this study are provided by TOLSA GROUP and are defined in Table 10: CIMSIL and PANGEL, both either delaminated or undelaminated for flocculation assessment.

Table 10- Properties of the two types of sepiolite used in the study: CIMSIL and PANGEL

	CIMSIL	PANGEL
Bulk density (g·cm ⁻³)	2.2	4.45
pH	7.7	8.7
Brookfield viscosity at 5 ppm (cP)	45000	56000
% of particles smaller than 5 µm	89.9	96.4
Specific surface (BET m ² ·g ⁻¹)	319	309

Source: **Own creation**

To study suspensions flocculation, cement and fibre-cement suspensions in water are mixed according to Table 11. Delamination consists in high-energy Ultraturrax stirring at 10000 rpm for 10 min in order to assure a colloidal system and the proper dispersion of sepiolite needles. APAM is used as a flocculant (Praestrol 1225). Cellulose is added to the suspensions according to Table 11 to replicate fibre-cement suspensions. Hornificated pine pulp (from pulp described in Block 2, section 3.2.1) is used as fibre source to avoid excessive water absorption of the cellulosic material during

the fibre-cement production. Four hornification cycles are used following the procedure described by Ballesteros et al. (2015).

Table 11- Composition of the suspensions used for the assessment of fibre-cement flocculation

Powder used	Cement (g)	CaCO (g)	Sepiolite Type and %		Sepiolite (g)	Flocculant (mL)	Cellulose (g)
Cement	18.40	***	***	***	***	1.33	***
Cement + filler	13.80	4.60	***	***	***	1.33	***
Cement + filler	13.66	4.60	CIMSIL	1%	0.14	1.33	1.60
+	13.52	4.60	CIMSIL	2%	0.28	1.33	1.60
undelaminated	13.66	4.60	PANGEL	1%	0.14	1.33	1.60
sepiolite	13.52	4.60	PANGEL	2%	0.28	1.33	1.60
Cement + filler	13.66	4.60	CIMSIL	1%	0.14	1.33	1.60
+	13.52	4.60	CIMSIL	2%	0.28	1.33	1.60
delaminated	13.66	4.60	PANGEL	1%	0.14	1.33	1.60
sepiolite	13.52	4.60	PANGEL	2%	0.28	1.33	1.60

Source: **Own creation**

3.4.2 Test methods

Since one of the main hydration products of MgO-SiO₂-H₂O systems is a poorly crystallized magnesium silicate hydrate with similar chemical composition as sepiolite [Mg₄Si₆O₁₅(OH)₂·6H₂O], it is expected to create new nucleation links between sepiolite and M-S-H gels. In order to explore this hypothesis, Scanning Electron Microscopy, X-Ray Diffraction and Thermogravimetry analysis are carried out on hardened slurry samples that are also vacuum filtered (500 mm of Hg) after mixing 18.4g of MgO-SiO₂ powder in 100 g of water for 5 min. After 10 days of steam curing at 55°C, hardened paste samples are used for cement characterization.

For XRD tests, pastes are finely crushed and sieved, using the particle fraction passing through 63 µm mesh. X'Pert Pro MPD PANalytical's X-ray diffractometer is used (Cu Ka radiation of 1.54 Å) to collect data between 5° and 65°. The thermal analysis (TG/DTG) of the samples is carried out in nitrogen atmosphere (50 mL/min) from 35 to 1000°C using a Seiko Exstar 6000 TGA/DTA thermobalance. SEM analysis is performed on a JSM 6335F electron microscope, JEOL brand with an intensity of 10 kV. The effect of sepiolite addition on the flexural performance of the MgO-SiO₂ cement is examined by elastic dynamic modulus (DMOE) analysis as an adaptation of the ASTM C1548 – 02 (2007) Standard (ASTM C1548 - 02, 2007), using a SONELASTIC® equipment, ATPC brand, Brazil. For ultrasound tests, 50 x 40 x 5 mm samples are casted and placed in a steam bath at 55°C for curing. DMOE is recorded over time and bulk density after 24 h of curing for every formulation.

Cement replacements of 1 and 2% by mass are used for both types of sepiolite. All samples are mixed in water (water to binder ratio of 0.5). For MgO-SiO₂ samples, 1% by mass of MELFLUX 2651F superplasticizer is used.

In order to test flocculation for the different suspensions, the procedure detailed by Fuente et al (2010) is applied. This process, summarized in Table 12, is applied by focused beam reflectance measurement technique (FBRM), using a M500L probe (Mettler Toledo, Seattle, USA). Thus, suspensions in 400 g of water are produced and analysed, mixing 18.4 g of different powder and powder-fibre solids in accordance with Table 11. Chord length distribution is recorded over time for all the compositions.

For water retention analysis, the method of Fuente et al. (2010) is also considered but the saturation in calcium hydroxide [Ca(OH)₂]. In this test, with the aim of obtaining a calcium free system that avoids cellulose degradation (MELO FILHO; SILVA; TOLEDO FILHO, 2013; TOLEDO FILHO et al., 2009) only MilliQ water is used. Subsequently, the different suspensions are submitted to vacuum drainage at 500 mm of Hg and water retention values are recorded over time to study the effect of the different sepiolite formulations during this fibre-cement manufacture stage.

Table 12- Method to assess pure powder and fibre-cement suspensions flocculation: adding sequence and stirring rate variations (meeting the process used by Fuente et al. (2010))

Samples with only powder particle suspensions		
Time (s)	Stage	Rotation speed (rpm)
0	Cement and filler addition	800
100	Sepiolite addition	800
300	Stirring intensity reduction	400
600	Flocculant addition	400
840	Deflocculation	800
960	Reflocculation	400
Samples with both powder particle and fibre suspensions		
Time (s)	Stage	Rotation speed (rpm)
0	Fibres addition	800
300	Cement and filler addition	800
400	Sepiolite addition	800
600	Stirring intensity reduction	400
900	Flocculant addition	400
1140	Deflocculation	800
1260	Reflocculation	400

Source: **Own creation**

Fibre-cement thin sheets of approximately 6 mm thickness are produced to carry out 4-point bending tests according to Block 2, section 3.2.3 or (MÁRMOL; SAVASTANO, 2017). For fibre-

cement composites flexural testing, 280 g of solids, meeting the same proportions as noted in Table 11, are used following the DPM technique described in Block 2, section 3.2.2.

After compaction, samples are cured for 5 days at 55°C and 90% relative humidity. Then pads are cut into 160 x 40 mm specimens. After 2 days of water immersion for saturated testing, samples are tested as indicated in Block 2, section 3.2.3 or (MÁRMOL et al., 2016). The same procedure is used to carry out the physical tests in accordance to ASTM C1185-08 (ASTM C1185-08, 2012) Standards. For Scanning Electron Microscopy test, after flexural testing, composite samples are cut into 1 x 1 x 1 cm cubes and embedded in epoxy resin. SEM samples preparation is conducted as described in Block 1 section 3.1.1. A Quanta 600 FEG microscope (FEI, Eindhoven, Netherlands) is used.

Since the effects of sepiolite addition on PC cement composites reinforced with cellulosic fibres has been already studied (JARABO et al., 2014), PC are just used as control samples (with no addition of sepiolite).

3.5 BLOCK 5

3.5.1 Materials preparation and characterization

Sisal fibres (*Agave sisalana*) as harvested in Pocinhos (Paraíba, Brazil), were used for this study. Without any treatment, unaged sisal fibres were cut to 4 cm length and individually embedded in cement paste prisms. For this study, high early strength Portland cement (CPV-ARI according to Brazilian Standards, equivalent to Type III as defined in ASTM-C150 (ASTM C150/C150M, 2012, p. 150) and Mg-SiO₂ cement, previously used in Block 2, section 3.2.1. A water to cement ratio of 1 was used to assure a proper moulding of the prisms and generate an excess of water for higher porosity and therefore higher alkaline medium. Two different ageing treatments were applied to the cement prisms: 1) 5 months of ageing of the prisms inside a sealed plastic bag at 25°C and 65% RH and 2) 400 accelerated ageing cycles for a rapid study of a simulated long-term ageing. Accelerated ageing cycles are conducted according to Block 2, section 3.2.3.

After these ageing treatments, cement prisms were mechanically crushed so fibres were detached and then different techniques were used to assess sisal fibres degradation.

3.5.2 Test methods

Thermogravimetric study was performed in a METLER TOLEDO TGA/SDTA851^e with simultaneous thermal analyser. Temperature was linearly increase at a pace of a 10°C/min from 25 to 800°C, with flow rates of 50 mL/min, in oxygen atmosphere inside alumina crucibles. During holocellulose decomposition, Activation Energy (E) was calculated from Arrhenius equation (18) that relates the reaction rate (k) and pre-exponential factor (A), universal gas constant (R) and the absolute temperature (T):

$$k(T) = A \cdot \exp\left(\frac{-E}{RT}\right) \quad (18)$$

Two methods for this calculation were used: 1) differential method (reference) where Activation Energy is calculated as in Equation (19)

$$\ln\left(-\frac{d\omega}{dt}\right) - \ln\omega = \ln A - \frac{E}{RT} \quad (19)$$

and 2) integral method, calculating E as in Equation (20)

$$\ln \ln\left(\frac{1}{x}\right) \cong \frac{-E}{RT} + \text{cons} \quad (20)$$

Where x is the residual fraction in Equation (21), defined as:

$$x = 1 - \frac{\omega_0 - \omega}{\omega_0 - \omega_\infty} = \frac{\omega - \omega_\infty}{\omega_0 - \omega_\infty} \quad (21)$$

Where ω is the sample mass at time t, ω_0 is the initial sample weight and ω_∞ is the final sample weight or residue.

A Bruker D2PHASER diffractometer equipped with a CuK α radiation (1.54056 Å) and source operated at 30 kV and 15 mA was used to irradiate finely chopped (1 mm length) sisal fibres. The resulting diffractogram was registered by scanning the samples from 10° to 40° (2 θ) in 0.02° steps at a rate of 0.30/min.

The crystallinity index, $I_c(\%)$, was calculated for every treatment also by two different methods:

1) using the equation (22) proposed by Segal (SEGAL et al., 1959):

$$I_c(\%) = \frac{I_{am}}{I_{max}} \times 100 \quad (22)$$

Where I_{max} is the maximum intensity of the (200) lattice reflection of cellulose I β type, located at 2θ between 22° and 23° , and I_{am} is the intensity attributed to amorphous part, given at 2θ between 18° and 19° for I β cellulose; and

2) by dividing the diffractogram area due to crystalline cellulose by the total area of the original diffractogram. For this method, amorphous cellulose from the diffractogram of the whole sample was subtracted with the aid of TOPAS software in order to establish crystalline fraction (PARK et al., 2010).

The crystallite size was determined by the Scherrer equation (LANGFORD; WILSON, 1978) according to Equation (23),

$$d = \frac{k\lambda}{\beta \cos\theta} \quad (23)$$

Where d is the perpendicular size to the lattice plane represented by the peak (200), k is the constant related to the shape of the crystallites and the indices of the reflecting plane, λ is the wavelength of the incident beam in the diffraction experiment, β is the peak width at half maximum (PWHM) in radians and θ is the position of the peak (half of the plotted 2θ value). For Scanning Electron Microscopy (SEM) tests, sisal fibres were embedded in epoxy resin to reproduce the state of the fibres cross section within a binding material. After resin hardening, samples were firstly polished with abrasive silicon carbide and then with alumina until smooth surface was achieved. Field emission scanning electron microscope (FESEM) ZEISS Brand, ULTRA 55 model, was equipped with microanalysis by EDS from Oxford Instruments Ltda.

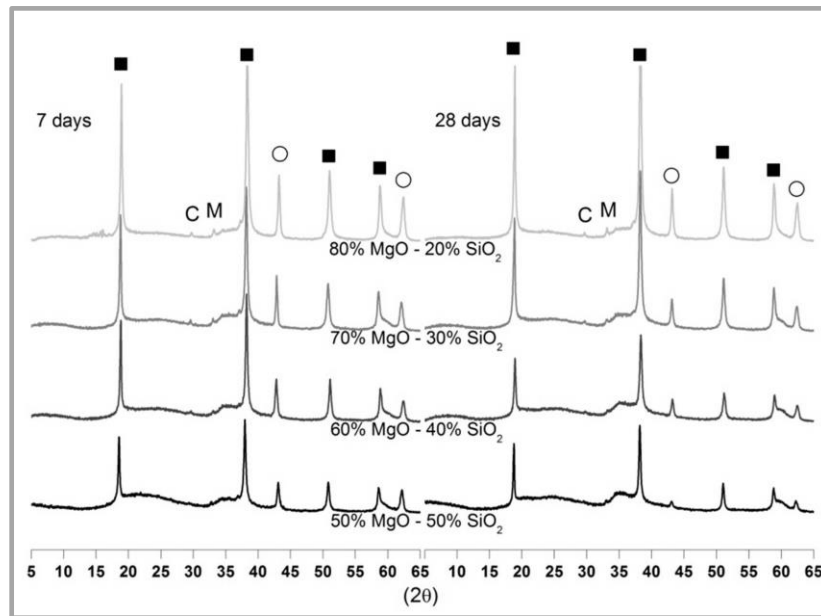
4 RESULTS AND DISCUSSIONS

4.1 BLOCK 1

4.1.1 XRD characterization

In Figure 12, XRD patterns for all the samples are depicted. For every sample, it can be seen that peaks corresponding to brucite have a higher intensity when compared to peaks matching reflections of periclase. This implies that most of the MgO has either been hydrated to form $\text{Mg}(\text{OH})_2$ or reacted to form M-S-H, with a hydration degree close to completion (up to 98% for samples with lower MgO content by Rietveld refinement). As expected, formulations with higher contents of MgO show more intense peaks corresponding to both periclase and brucite, as there is less opportunity for conversion to M-S-H in these instances, and thus a lower degree of reaction. The most remarkable difference between samples at 7 and 28 days is that the peaks corresponding to periclase (at 43 and 62°) decrease with time for every system. According to literature (ALI; KOTP; EL-NAGGAR, 2010; BREW; GLASSER, 2005; JIN; AL-TABBAA, 2014; LOTHENBACH et al., 2015; RASHID et al., 2009; ROOSZ et al., 2015; SZCZERBA et al., 2013; TEMUUJIN; OKADA; MACKENZIE, 1998, 2005; ZHANG; CHEESEMAN; VANDEPERRE, 2011; ZHANG; VANDEPERRE; CHEESEMAN, 2014), magnesium silicate hydrated formed from a mixture of MgO and silica rich powder in the presence of water shows highly disordered characteristics with broad peaks throughout the diffraction pattern range. Two minor, broad peaks are evident here at $33\text{--}39^\circ$ and $58\text{--}61^\circ$ 2θ . Another expected broad peak corresponding to magnesium silicate hydrate is supposed to appear between $25\text{--}30^\circ$ 2θ but in this case it overlaps with the broad hump due to unreacted silica. These features confirm the presence of M-S-H gels (ALI; KOTP; EL-NAGGAR, 2010; BREW; GLASSER, 2005; JIN; AL-TABBAA, 2014; LOTHENBACH et al., 2015; RASHID et al., 2009; ROOSZ et al., 2015; SZCZERBA et al., 2013; TEMUUJIN; OKADA; MACKENZIE, 2005; WALLING et al., 2015; ZHANG; VANDEPERRE; CHEESEMAN, 2014).

Figure 12- XRD diffractograms of the different MgO-SiO₂ samples at 7 days (left) and at 28 days (right). Peaks marked are brucite (■), periclase (○), calcite (C) and magnesite (M)

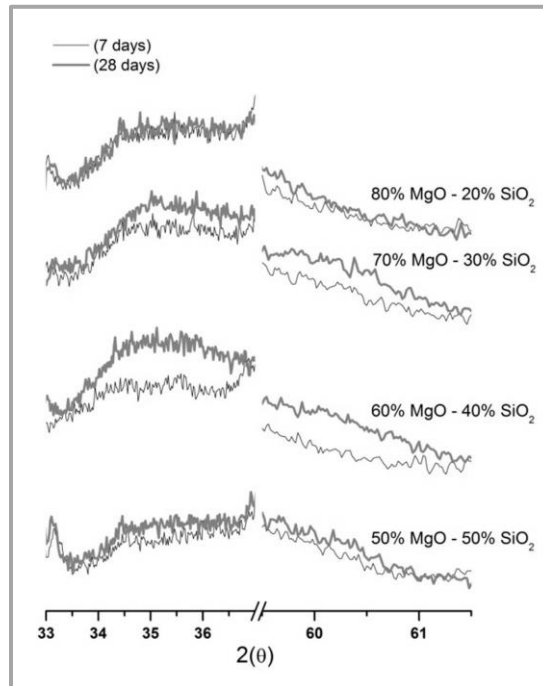


Source: Own creation

Figure 13 shows an enlarged view of selected key regions of Figure 12 for every formulation. Parts of the regions where features arising from M-S-H gel are expected have been omitted since they overlapped with unreacted silica peaks, so Figure 13 illustrates just the regions where only gel bumps are manifest (33-37° and 59.5-61.5° 2θ). Both regions show a broad hump corresponding to the M-S-H gel XRD patterns obtained in previous studies, confirming the presence of the gel. Nevertheless the intensity of these humps is not as high as it is found in previous works. This may be explained by the fact that M-S-H gel is not the only main phase present in the matrix, in contrast to what is intended in previous reports where synthesized magnesium silicate is the only constituent (BREW; GLASSER, 2005; TEMUJIN; OKADA; MACKENZIE, 1998; ZHANG; VANDEPERRE; CHEESEMAN, 2014). In the two regions, between 35-39° and 58-61° 2θ, the intensity of the humps for most of the formulations is slightly higher for 28 day cured samples, suggesting that the development of the gel have been ongoing over time. According to literature Mg(OH)₂ content tends to decrease with time, although there is little systematic variation observed here due to the replenishment of Mg(OH)₂ by ongoing hydration of remnant MgO. It can be assumed that Mg(OH)₂ reacts with SiO₂ to form more gel (JIN; AL-TABBAA, 2014; LIAO; SENNA, 1993; LOTHENBACH et al., 2015; ROOSZ et al., 2015; SANDBERG; MOSBERG, 1989; SZCZERBA et al., 2013; TEMUJIN; OKADA;

MACKENZIE, 1998, 2005; WALLING et al., 2015; ZHANG; VANDEPERRE; CHEESEMAN, 2014). This phenomenon may be accelerated by pretreatment of the MgO-SiO₂ powder, either mechanical (grinding) or chemical (use of deflocculants such as sodium phosphates), that contribute to the reduction of the crystallization degree of Mg(OH)₂ and therefore improve dissolution in aqueous environments.

Figure 13- Enlarged view of the XRD spectra of the regions where gel bumps are present



Source: Own creation

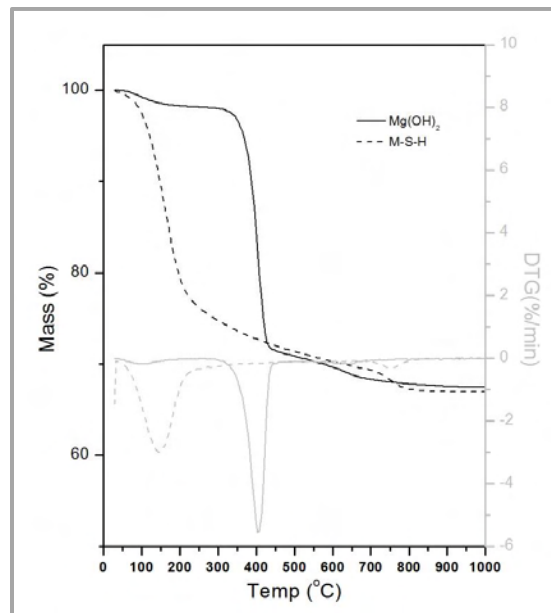
4.1.2 TG characterization

Figure 14 shows thermogravimetric curves for hydrated MgO and synthetic M-S-H gel at 28 days and their differential curves. From the differential thermogravimetric (DTG) curves it is possible to distinguish clearly two endothermic peaks, one below 300°C corresponding to the synthesized gel and, another one corresponding to Mg(OH)₂, between 300 and 550°C. These two peaks have been found by other authors that produced M-S-H gels (JIN; AL-TABBAA, 2014; LOTHENBACH et al., 2015; ROOSZ et al., 2015; WALLING et al., 2015; ZHANG; VANDEPERRE; CHEESEMAN, 2014). These two peaks match perfectly the peaks produced by TG analysis of calcium silicate hydrate and calcium hydroxide, the main products obtained during the hydration of tri-calcium silicate (C₃S) and bi-

calcium silicate (C_2S), which together make up 75–80% of Portland cement (RAMACHANDRAN, 2003). Also from Figure 14 it is depicted another tiny endothermic peak at around 750°C, in the DTG curve of M-S-H gel but it has been neglected for phase determination.

In Figure 15, it is displayed TG and DTG analysis for every assessed formulation containing MgO - SiO_2 at 7 and 28 days. In this figure it is also possible to identify the two main peaks obtained in Figure 14, concluding that the major hydrated phases present in this type of material are $Mg(OH)_2$ and M-S-H gel. These results are very similar to those obtained after the hydration of synthetic C_3S and C_2S , where similar peaks were obtained at the same range of temperatures for $Ca(OH)_2$ and C-S-H gel (GOÑI et al., 2010). The only difference is that in the case of M-S-H gel the first endothermic peak is centered between 110 and 135°C, instead of 75°C for both C-S-H gels (GOÑI et al., 2010). In this way, at initial stages, it is likely to associate the mass loss to weakly adsorbed surface water and water bound to exchangeable cations in the gel when the mass loss is produced below 300 and over 550°C. This is also in agreement with other authors (SZCZERBA et al., 2013; WALLING et al., 2015; ZHANG; VANDEPERRE; CHEESEMAN, 2014). From Zhang et al. TG analysis, where until 14 days the principal mass loss is produced below 300°C, the increase in water content means a higher M-S-H gel content since the higher amount of water the higher XRD intensity of the bumps.

Figure 14- TG and DTG graphs of the hydrated MgO (AR200) and M-S-H gel with a 0.5 Mg/Si ratio



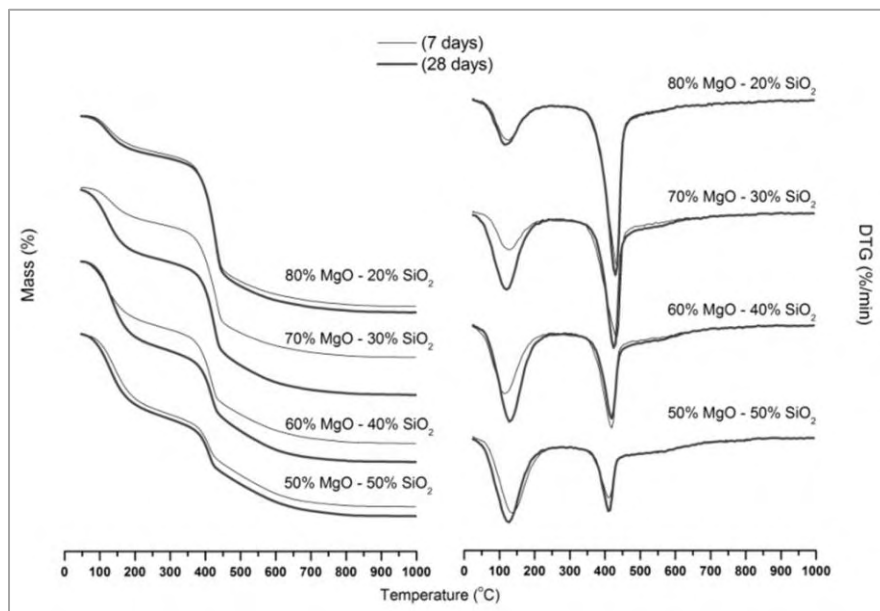
Source: Own creation

The same way it is reasonable to estimate the amount of $\text{Mg}(\text{OH})_2$ present in the samples by considering the mass loss between 300 and 550°C mainly due to the dehydroxilation of $\text{Mg}(\text{OH})_2$ (TEMUUJIN; OKADA; MACKENZIE, 1998), as follows:



After such considerations, results of mass loss displayed in Table 13 are obtained from Figure 15. In accordance with XRD results (Figure 12), from these results it is also inferred that the higher content in MgO, the higher content in $\text{Mg}(\text{OH})_2$ for both 7 and 28 days. This amount of $\text{Mg}(\text{OH})_2$ for every formulation does not increase from 7 to 28 days. Contrarily to $\text{Mg}(\text{OH})_2$ results, the content on M-S-H increases with the lower content of MgO at 7 days. However, at 28 days, the higher content on magnesium silicate hydrated is achieved by the 60% MgO – 40% SiO_2 system.

Figure 15- TG (left) and DTG (right) graphs of the of the different MgO- SiO_2 samples at 7 days and at 28 days



Source: Own creation

Table 13- Weight loss according to TG results of the different MgO-SiO₂ samples at different temperatures ranges

Formulation	Curing time	Mass loss (%)		
		25-300°C	300-550°C	550-1000°C
50%MgO-50%SiO ₂	7 days	11.07	10.02	3.00
	28 days	11.71	9.81	3.24
60%MgO-40%SiO ₂	7 days	9.35	12.92	2.79
	28 days	12.29	12.50	2.86
70%MgO-30%SiO ₂	7 days	6.87	15.72	2.38
	28 days	10.02	15.48	2.78
80%MgO-20%SiO ₂	7 days	5.26	18.34	2.41
	28 days	5.71	17.82	2.90

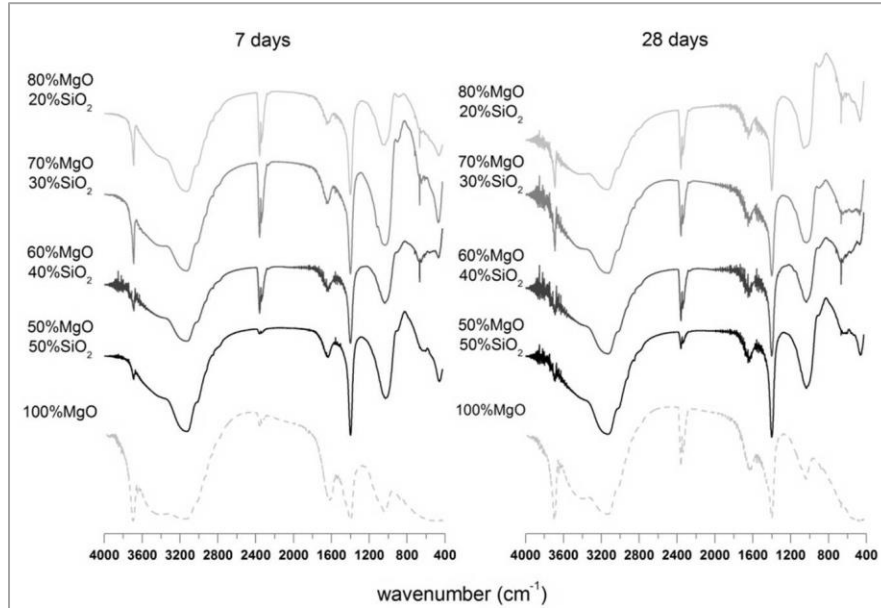
Source: **Own creation**

4.1.3 FT-IR characterization

FT-IR results in Figure 16 show that the systems containing MgO and SiO₂ present a similar spectra to systems with 100% MgO for every formulation, proving the great influence of Mg(OH)₂ structure in the hydrated pastes. Brucite is the main hydration product expected for a powder with 97.4% MgO purity, In addition. It is a member of the group of minerals known as the layer hydroxides, whose structures show similarities to the layer and chain silicates as well as the basic building unit of all the layered double hydroxide (LDH) structure minerals (KAMATH; ANNAL THERESE; GOPALAKRISHNAN, 1997). Thus, it is uncertain to establish which vibrational bands belong to Mg(OH)₂ and which ones to M-S-H gel. 100% MgO hydrated samples, at both 7 and 28 days, show bands around between 3000-3700, 1600, 1400 and 1040 cm⁻¹ that are accurately reproduced for every MgO-SiO₂ samples. For 100% MgO samples the broadening peak from 3300 to 3600 cm⁻¹ and the peak at 1600 cm⁻¹ are derivable from H-bonding of coordinated water (ALI; KOTP; EL-NAGGAR, 2010; LOTHENBACH et al., 2015) due to an excess of adsorbed water molecules on the MgO surface, as the 0.5 w/c exceeds the water requirement for MgO hydration. The sharp absorbance near 3696 cm⁻¹ is a characteristic Mg–OH stretch and around 1400 and 1040 cm⁻¹ Mg-OH bend is also depicted (HANNA, 1965; BRATERMAN, 2006; TEMUUJIN; OKADA; MACKENZIE, 1998). In the literature the peak at 1040 cm⁻¹ also reveals Si–O–Si vibrations of the tetrahedral sheets within the talc structure (JIN; AL-TABBAA, 2014; WALLING et al., 2015). The sharp peak in 3696 cm⁻¹ is more prominent for samples with a higher content in MgO which is coincident with previous results. In previous works with M-S-H gels, at 1640 cm⁻¹ (ALI; KOTP; EL-NAGGAR, 2010) and 1400 cm⁻¹ (BREW; GLASSER, 2005), identical bonds are present (OH stretching) and at approximately

1040 cm^{-1} a strong band is present due to Si–O–Si symmetrical stretching vibrations (JIN; AL-TABBAA, 2014; RASHID et al., 2009; WALLING et al., 2015), hindering the identification of the phases.

Figure 16- FT-IR spectra of the different MgO-SiO₂ and 100% MgO samples at 7 days (left) and at 28 days (right)



Source: Own creation

Although all the similarities in the spectrograph from 1000-4000 cm^{-1} , clear differences arise from 400 to 1000 cm^{-1} between the 100% MgO and the MgO-SiO₂ systems. For the MgO-SiO₂ systems, a sharp peak around 672 cm^{-1} arises from Si–O bending vibrations (LOTHENBACH et al., 2015) while Mg–O vibrations occur at 455 cm^{-1} (BREW; GLASSER, 2005; ALI; KOTP; EL-NAGGAR, 2010). However these bonds show no modifications for MgO-SiO₂ samples over time and remain alike at 7 and 28 days, being complicated to establish whether phases concentration stay at equal levels or gels with LDH are formed from Mg(OH)₂.

4.1.4 Hydration reactions and systems composition

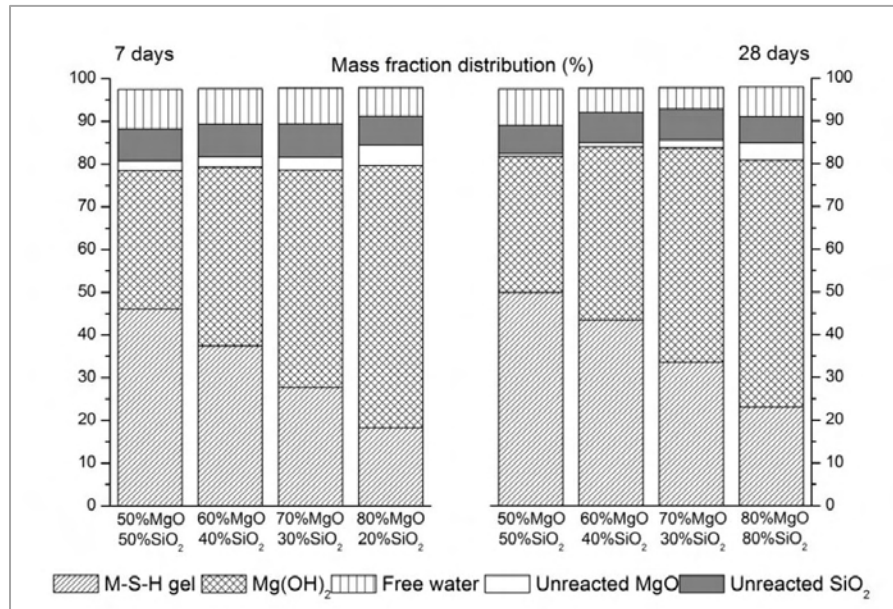
On the basis of all the analysis carried out to understand the hydration of this cementitious system, the different hydration reactions are adjusted in Table 14 at ages 7 days and 28 days respectively:

Table 14- Hydration reaction of the different formulations studied at 7 and 28 days

7 days					
	M-S-H gel	MH	Mu	Su	Hu
50% MgO - 50% SiO ₂	0,40 M _{0,48} SH _{1,94}	0,56	0,06	0,12	0,51
60% MgO - 40% SiO ₂	0,29 M _{0,64} SH _{2,29}	0,72	0,06	0,13	0,46
70% MgO - 30% SiO ₂	0,19 M _{0,97} SH _{2,76}	0,87	0,07	0,13	0,47
80% MgO - 20% SiO ₂	0,10 M _{1,18} SH _{4,43}	1,05	0,12	0,11	0,37
28 days					
	M-S-H gel	MH	Mu	Su	Hu
50% MgO - 50% SiO ₂	0,42 M _{0,59} SH _{1,99}	0,55	0,01	0,11	0,46
60% MgO - 40% SiO ₂	0,30 M _{0,81} SH _{2,76}	0,69	0,02	0,12	0,32
70% MgO - 30% SiO ₂	0,20 M _{1,12} SH _{3,61}	0,86	0,05	0,12	0,28
80% MgO - 20% SiO ₂	0,11 M _{1,82} SH _{4,40}	0,99	0,10	0,10	0,34

Source: **Own creation**

M, S and H represent the concentration of raw materials mixed, correcting the molarity according to powders purity, to yield the different hydration products (MgO, SiO₂ and H₂O respectively), MH stands for brucite which is determined as described in Section 3.2, Mu, Su and Hu refer to the amount of unreacted raw materials. Unreacted silica and water have been calculated as the difference between the original concentrations of raw materials and the concentration of these molecules in the M-S-H and MH molecules. Mu concentration has been obtained from Rietveld analysis, where periclase peaks have been compared between 100% AR200 MgO samples and the different MgO-SiO₂ systems. H in M-S-H has been quantified from TG analysis, considering water molecules released below 300 and over 550 °C. M in M-S-H has been estimated as the difference between the original concentration before mixing and the MgO present in MH and Mu. With the help of EDS analysis (Table 15), MgO/SiO₂ is determined in the M-S-H particles so it is also possible to determine S in M-S-H. It is important to remark that Hu represents a surplus of water required for mixing and good workability. This excess of water is evaporated in the drying process, generating voids in the matrix (capillary porosity). Figure 17 displays the mass fraction distribution at 7 and 28 days, calculated from Table 15.

Figure 17- Mass fraction distribution of all the components of MgO-SiO₂ pastes, determined from different tests results

Source: Own creation

4.1.5 SEM

The aspect of the hydrated paste at 28 days of the 60%MgO-40%SiO₂ system polished surface is given at Figure 18(a). The microstructure, as confirmed in preliminary tests, is mainly comprised by Mg(OH)₂ crystal particles dispersed in a M-S-H gel matrix. Mg(OH)₂ particles present two equal dimensions sections with very defined corners. In Figure 18(b), the same image as in Figure 18(a) is edited with the help of EDS mapping to clearly identify the different phases in the cement. In yellow, the brucite particles have been thresholded and in blue, the M-S-H gel. Tiny white particles correspond to unreacted silica particles. Darker blue zones match the impurities present in the MgO powder.

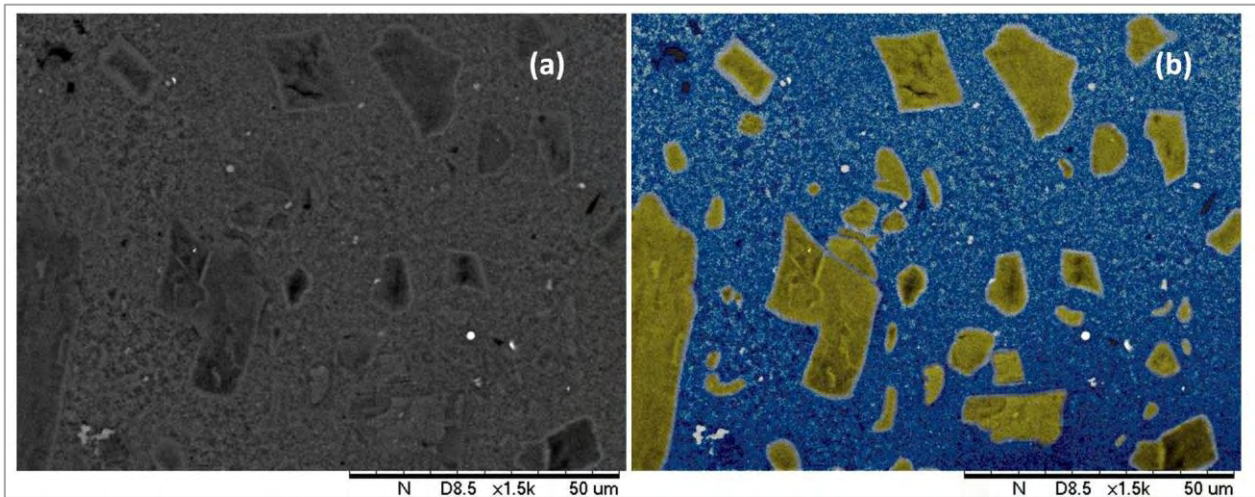
Table 15- Mg/Si ratio for the different MgO-SiO₂ systems according EDS results

Age		50MgO 50SiO ₂	60MgO 40SiO ₂	70MgO 30SiO ₂	80MgO 20SiO ₂
7 days	\bar{x}	0.48	0.64	1.00	1.18
	σ	0.03	0.03	0.08	0.08
28 days	\bar{x}	0.69	0.81	1.12	1.82
	σ	0.03	0.10	0.10	0.10

Source: Own creation

The interface between $\text{Mg}(\text{OH})_2$ crystals and M-S-H gel has also been highlighted in grey. Using EDS mapping it is possible to establish that the interface has a high concentration of Si molecules. Considering the $\text{Mg}(\text{OH})_2$ crystals as almost non Si concentration region, on the boundaries of these particles an overconcentration of unreacted silica is produced.

Figure 18- (a) SEM image of the polished surface of a 60% MgO – 40% SiO_2 paste at 28 days. (b) Treated SEM image of a 60% MgO - 40% SiO_2 at 28 days. Yellow particles are $\text{Mg}(\text{OH})_2$, blue regions are M-S-H gels and white particles are unreacted SiO_2



Source: Own creation

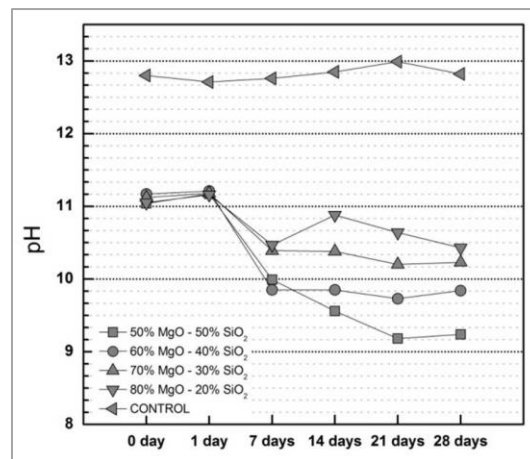
According to hydration of MgO reaction mechanism (FEITKNECHT; BRAUN, 1967; FRUHWIRTH et al., 1985), water is chemisorbed on MgO to form a liquid layer on the surface. Then water reacts with the MgO to form a surface layer of $\text{Mg}(\text{OH})_2$ and $\text{Mg}(\text{OH})_2$ subsequently dissolves in the water layer and, only after layer becomes saturated, precipitation takes places. In the meantime plenty of OH^- cations are released promoting the dissolution of SiO_2 into silicic acid form $[\text{Si}(\text{OH})_4]$ and anion $\equiv\text{Si-O}^-$ ion (ALEXANDER; HESTON; ILER, 1954) which increase the concentration of Si surrounding $\text{Mg}(\text{OH})_2$ crystals that can be seen in Images 1 and 2. The presence of Mg^{2+} cations neutralizes these anions charges. The apparition of the $-\text{Si-O-Mg}^{2+}$ linkage does not allow the reverse reaction to form siloxane bonds. Since this work is focused only on the early hydration stages, it is difficult to predict the evolution of the reaction over time. However, in the light of previous works where ageing until 90 and 180 days is studied (SZCZERBA et al., 2013; JIN; AL-TABBAA, 2014), $\text{Mg}(\text{OH})_2$ is expected to continue to react with the unreacted silica to form more M-S-H gel. For longer curing time, TG curves tend to be smoother indicating the continuous transition

from brucite to M–S–H in the region between 300 and 550°C. Also from TG curves, in which synthesized gels have been used (LOTHENBACH et al., 2015; ROOSZ et al., 2015), it can be deduced that at this range of temperatures (300-550°C) gel dehydroxylation takes place, suggesting that OH⁻ ions from Mg(OH)₂ end up as a part of the poor crystallized structure of the magnesium silicate hydrate by replacing part of the silicate chains.

4.1.6 Matrix selection for fibre-cement purposes: pH evaluation and compressive strength analysis

From Figure 19 it can be seen that all the samples containing MgO present notoriously lower pH values compared to PC samples, confirming a lower concentration of OH⁻ ions in the matrix. Meanwhile Control sample keeps stable pH values with time (12.80-13.00), MgO samples present a descent value of pH for all the formulations. In so far as MgO is increased in the MgO-SiO₂ formulations, the pH values do not decrease as much as it happens for samples with lower contents in MgO since their higher content in hydroxyls. It can be observed that the most important reduction of pH occurs between 1 and 7 days. From that age, only 50% MgO – 50% SiO₂ samples present a pH decrease until the age of 21 days, when it gets stabilized. pH results are consistent with previous works where MgO-SiO₂ systems are analyzed (ZHANG; CHEESEMAN; VANDEPERRE, 2011), obtaining pH values below 10 at 28 days. In addition, samples containing 60% of MgO and 40% of SiO₂ have a pH value around 10 at 7 days and decreases with time to reach a pH value of 9.8. This reduced alkalinity could be very advantageous since pH values below 11 at early stages help to prevent cellulosic fibre degradation (MÁRMOL et al., 2013).

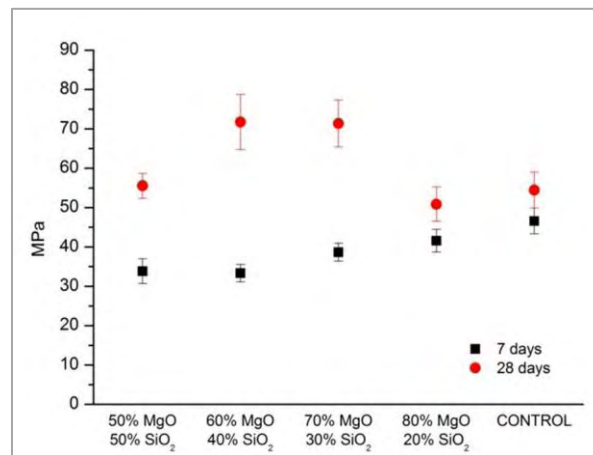
Figure 19- pH evolution over time of different MgO-SiO₂ blended systems and control samples (100% Portland cement)



Source: Own creation

Figure 20 shows the compressive strength results. At 7 days, it appears to be a slight enhancement of the mechanical strength with the increase of the MgO in the samples. This difference is statically significant (Table 16) when the MgO content varies from 60 to 70%, so it can be concluded that at 7 days of curing samples containing 50 and 60% of MgO and 70 and 80% have similar values. At this same age, PC samples have significant higher values compared to almost every samples with MgO. The only sample with an equivalent performance is 80% MgO – 20% SiO₂.

Figure 20- Compressive axial strength of different MgO-SiO₂ pastes and control samples (100% Portland cement) at 7 and 28 days



Source: Own creation

However at 28 days, all the formulations containing MgO have at least the same performance that Control samples have. It is also remarkable that all the MgO-SiO₂ samples present a strength improvement for every formulation, in contrast to Control samples which have no statistic considerable variation. 60% MgO – 40% SiO₂ and 70% MgO – 30% SiO₂ systems have the highest values, 71.8 and 71.4 MPa respectively, showing a statistical difference with the rest of the samples. These values are also around 30% higher compared to PC samples, with an average compressive strength of 54.5 MPa. This fact may be explained because of the excessive water to cement ratio used (0.5) to mold Portland cement pastes. The majority authors appear to have fixed with the remark that complete hydration is not possible if w/c is below 0.38 although it has been reported total hydration even in pastes with w/c = 0.22 (TAYLOR, 1997). However a w/c = 0.5 is not disproportionate for MgO-SiO₂ systems, according to Lothenbach et al. (2015), who establishes that M-S-H gels present a silicate sheet structure and a higher amount of chemically bound water compared to Portland cement.

Table 16- Compressive strength results of the different MgO-SiO₂ systems and control samples (100% Portland cement). Tukey test (0.05 confidence) are represented next to the numeric value. Compressive strength at 28 days to compressive strength at 7 days ratio is on the right column

	7d	28d	R_{c28d}/R_{c7d}
50% MgO 50% SiO ₂ \bar{x} (MPa)	33.9 a, A	55.5 a, B	1.64
σ (MPa)	3.15	3.13	
60% MgO 40% SiO ₂ \bar{x} (MPa)	33.4 a, A	71.8 b, B	2.15
σ (MPa)	2.20	7.00	
70% MgO 30% SiO ₂ \bar{x} (MPa)	38.7 a, b, A	71.4 b, B	1.85
σ (MPa)	2.27	6.00	
80% MgO 20% SiO ₂ σ (MPa)	41.6 b, c, A	50.9 a, B	1.22
σ (MPa)	2.90	4.38	
CONTROL \bar{x} (MPa)	46.6 c, A	54.5 a, A	1.17
σ (MPa)	3.29	4.57	

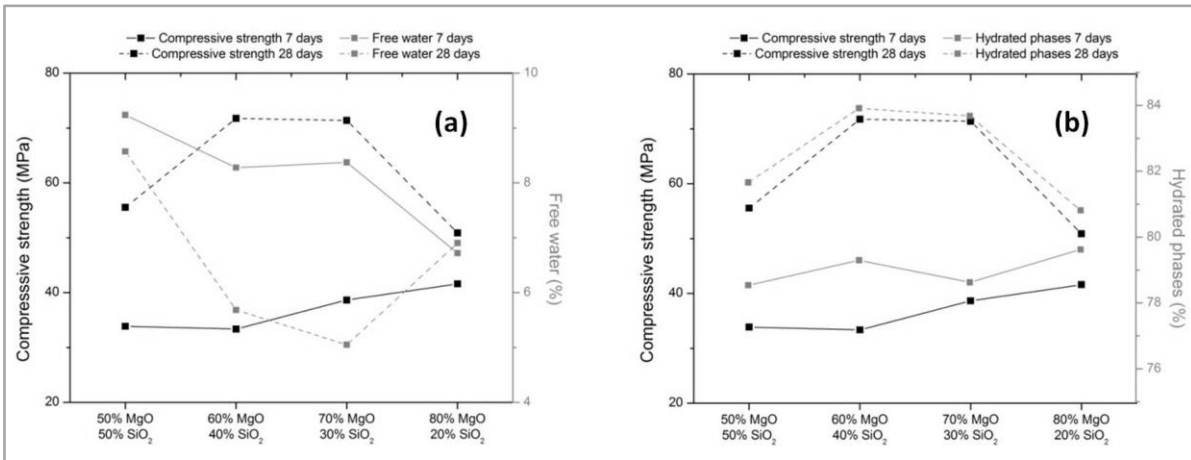
Same lower case letters in the same column mean no statistical significant difference.

Same capital letters in the same row mean no significant statistical significant difference.

Source: **Own creation**

Considering Figure 21, it is reasonable to establish a relation between compressive strength and both free water and total amount of hydrated phases in the systems. The less free water in the matrix leads to higher compressive strength. This is in line with what happens with other types of inorganic cement as Portland cement (TAYLOR, 1997; LEA; HEWLETT, 2004), where an increase of porosity leads to a drastic decrease of mechanical properties. Another clear trend related to compressive strength is the relation between compressive strength and total amount of hydrated phases. This relation is especially evident at 28 days Figure 21b, where compressive strength and total amount of hydrated phases match in an accurate manner. Also it is possible to infer that all the samples with MgO have a compressive strength at 28 days to compressive strength at 7 days ratio (R_{c28d}/R_{c7d} in Table 16) higher than Control samples. This ratio has a precise coincidence with the amount of hydrated phases in the pastes. This fact is an interesting evidence to conclude that the amount of M-S-H is not the only determinant factor to obtain more resistant cements at initial stages.

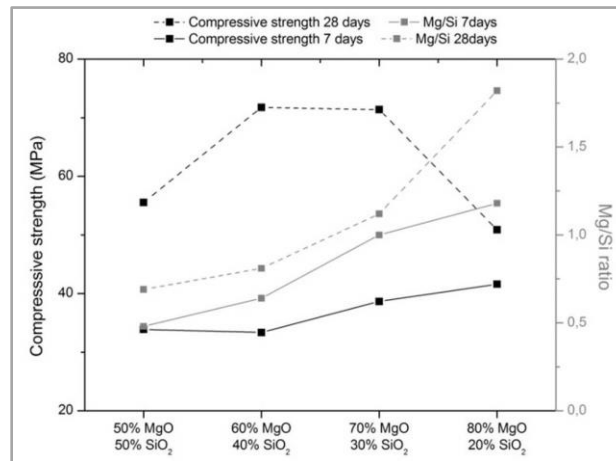
Figure 21- (a) Trends in double Y-axis of the compressive axial strength (left axis) and free water content (right axis). (b) Trends in double Y-axis of the compressive axial strength (left axis) and total hydrated phases content (right axis)



Source: Own creation

Attending to the relationship between compressive strength and the Mg/Si ratio for the different formulations (Figure 22), at 7 days it is possible to detect how the higher Mg/Si ratio implies a higher compressive strength. However this trend is not displayed at 28 days, where the formulation with highest Mg/Si ratio (80% MgO – 80% SiO₂) presents the lowest mechanical performance. All which can be deduced from Figure 22 is that the formulations with the uppermost strength for both ages, 7 and 28 days, present a Mg/Si ratio ranging from 0.8-1.2, according to what is pointed out at the literature (JIN; AL-TABBAA, 2014; LI et al., 2014; LOTHENBACH et al., 2015; WALLING et al., 2015). This difference in Mg/Si content may be associated to a change in M-S-H gel structure (BREW; GLASSER, 2005; LOTHENBACH et al., 2015; WALLING et al., 2015), achieving a more resistant structure (Q³ silica tetrahedral) for Mg/Si ratios around 0.8-1.2.

Figure 22- Trends in double Y-axis of the compressive axial strength (left axis) and Mg/Si ratio (right axis)



Source: Own creation

In view of the pH and compressive strength results, in order to choosing the optimal matrix to produce fibre-cement products reinforced with lignocellulosic fibres, the system that would offer the lowest pH value is the 50% MgO – 50% SiO₂ formulation. However this formulation has approximately 30% less of compressive strength compared with the 60% MgO – 40% SiO₂ formulation and besides the difference in pH between this two formulations is not very noteworthy. Since the formulation that offers a better compromise between alkalinity and mechanical properties, the most promising formulation selected is the 60-40.

4.2 BLOCK 2

4.2.1 Flexural test

4.2.1.1 Composites reinforced with pine fibres

At 28 days the best MOR results, shown in

Table 7, are achieved by PC samples (average of 11.35 MPa). These values are significantly higher compared to the samples made out of MgO-SiO₂ cement (9.03 MPa). This difference may be attributed to the matrix performance and therefore explained because of the water to binder ratio for the different formulations. As it can be seen in Table 8, the water demand for the samples where MgO-SiO₂ cement has been used (0.60) is higher than for samples using Portland cement (0.45). This

water/binder factor can generate an excess of water in the matrix, increasing the capillary pores, which is closely related to the decrease of the mechanical performance of cementitious materials (CHEN; WU, 2013; KUMAR; BHATTACHARJEE, 2003; OZTURK; BARADAN, 2008). A data that confirms this fact is the bulk density of the materials at this age (Table 19), where the values for MgO-SiO₂ cement samples (1.39 g/cm³) are inferior to those for PC samples (1.54 g/cm³). At this same age, it can be seen that MOE is also clearly superior for Portland cement samples when compared to samples with MgO-SiO₂ cement, presenting values of 7.59 and 3.26 GPa respectively. This fact also supports the idea that the higher flexural strength for samples with PC is correlated with its higher binder performance at 28 days, since MOE in cementitious materials is closely related to cementitious materials strength, considering the low modulus of vegetable fibres (ARDANUY; CLARAMUNT; TOLEDO FILHO, 2015; MEHTA; MONTEIRO, 2006; NOGUCHI et al., 2009).

Table 17- MOR, LOP and MOE results of every formulation at 28 days and after 200 cycles of accelerated ageing

		MOR* (MPa)		LOP* (MPa)		MOE* (GPa)	
		28 days	200 acc	28 days	200 acc	28 days	200 acc
		\bar{x}	σ	\bar{x}	σ	\bar{x}	σ
MgO-SiO ₂ - Pine	\bar{x}	9.03 a, A	10.63 a, B	2.94 a, A	5.94 a, B	3.26 a, A	4.92 a, B
	σ	0.70	1.68	0.68	0.89	0.19	0.35
MgO-SiO ₂ - Eucalyptus	\bar{x}	9.23 a, A	10.36 a, B	4.49 b, A	4.98 b, A	5.71 b, A	5.99 a, A
	σ	1.12	1.38	0.39	1.23	0.38	0.70
PC - Pine	\bar{x}	11.35 b, A	9.07 b, B	6.55 b, A	7.45 c, A	7.59 c, A	9.13 b, B
	σ	0.93	0.78	1.30	0.84	0.91	0.35
PC - Eucalyptus	\bar{x}	11.24 b, A	7.69 c, B	5.22 c, A	6.95 a, c, B	8.84 c, A	11.16 c, B
	σ	1.06	1.20	1.33	0.91	2.15	1.53

*MOR= Modulus of Rupture, LOP= Limit of Proportionality, MOE= Modulus of Elasticity

Same lower case letters in the same column mean no statistical significant difference and vice versa.

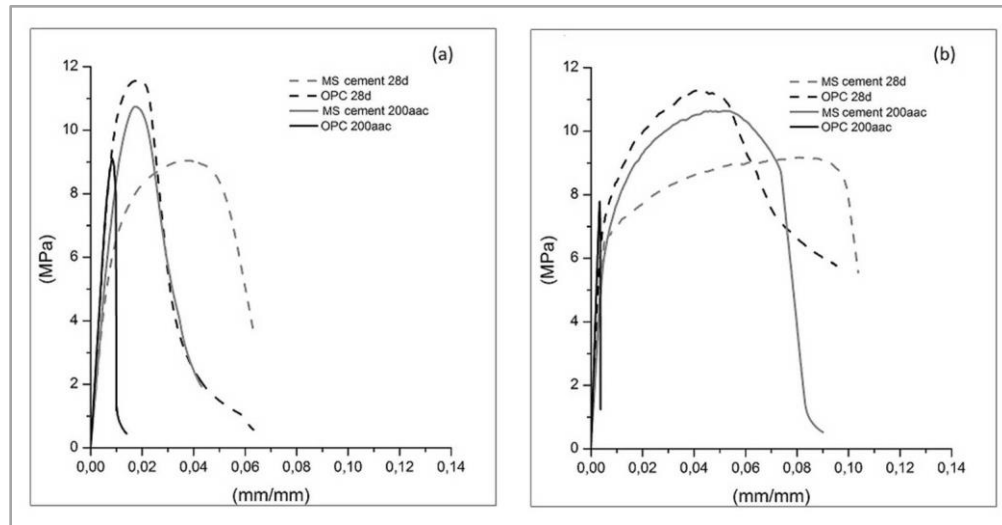
Same capital letters in the same row mean no significant statistical significant difference and vice versa.

Source: **Own creation**

However the excess of water within the matrix, and hence a more porous matrix, can be responsible for a better interface between fibre and matrix, where pull-out is favoured instead of fibres collapse, promoting a higher deformation and absorbing more energy (SAVASTANO; WARDEN; COUTTS, 2005; TOLEDO FILHO et al., 2000). Even with a lower MOR for MgO-SiO₂ samples, SE thereof at 28 days (2.75 kJ/m²) is significantly outstanding when compared to PC samples (1.51 kJ/m²), which means that this new type of cement presents a good compatibility with pine pulp to

resist flexural loads. The good flexural performance of the samples using MgO-SiO₂ cement is still more pronounced with regard to the specific deflection at 50% of MOR, where these present a value of 0.05, more than twice than the value obtained for PC samples.

Figure 23- Tension-deflection curves of the composites reinforced with pine (a) and eucalyptus (b) pulps for both types of binders, MgO-SiO₂ (MS) and Portland (OPC), at 28 days and after 200 cycles of accelerated ageing



Source: Own creation

In contrast to what occurs at 28 days, the highest MOR values after 200 aac is exhibited by MgO-SiO₂ samples (10.63 MPa). These samples experienced a statistical gain (from 9.03 MPa) that is accompanied also by another statistical MOE increase (from 3.26 to 4.92 MPa). All together indicates that the MOR improvement for MgO-SiO₂ samples corresponds to the matrix modification and densification of the interfacial transition zone (ITZ). This is also based on the notable increase of the bulk density that is experienced (from 1.39 to 1.46 g·cm⁻¹) by these samples (Table 19). The matrix modification of MgO-SiO₂ samples may be responsible for the reduction of the specific deflection at 50% of MOR due to changes in the fibre-matrix interface. A less porous matrix may densify the vicinity of the fibre region. Therefore the adherence between fibre and matrix is improved and pull-out mechanism is hindered (SAVASTANO; WARDEN; COUTTS, 2005; TOLEDO FILHO et al., 2000).

In the case of samples made out of PC the MOR suffers a drastic loss although MOE rises with a statistical significance, from 7.59 to 9.13 GPa. MOE and LOP are related to the matrix phase densification, which is favoured along hydration process that takes place after ageing cycles.

According to what was suggested previously, in this case the improvement of the matrix performance does not imply a better mechanical resistance of the whole composite. It is remarkable that, apart from suffering a drastic reduction of the MOR, specific energy and deflection, after ageing the samples made with PC have a slight increase of LOP, when compared to samples at 28 days. Considering LOP as the first cracking point in the stress-deformation curve (ARDANUY; CLARAMUNT; TOLEDO FILHO, 2015) and therefore the point where strain hardening begins, the limited growth of flexural stress after LOP may be considered as a decline of the reinforcing capacity of the fibres.

Table 18- SE and SD results of every formulation at 28 days and after 200 cycles of accelerated ageing

		SE* (kJ/m ²)		SD* (mm/mm)	
		28 days	200 acc	28 days	200 acc
		\bar{x}	σ	\bar{x}	σ
MgO-SiO ₂ - Pine	\bar{x}	2.75 a, A	1.10 a, B	0.05 a, A	0.02 a, B
	σ	0.61	0.17	0.01	0.00
MgO-SiO ₂ - Eucalyptus	\bar{x}	5.40 b, A	5.07 a, A	0.10 b, A	0.08 b, A
	σ	0.98	1.06	0.01	0.01
PC - Pine	\bar{x}	1.51 a, A	0.18 b, B	0.02 b, A	0.01 c, A
	σ	0.49	0.05	0.01	0.00
PC - Eucalyptus	\bar{x}	4.97 b, A	0.14 c, B	0.08 c, A	0.00 a, c, B
	σ	1.67	0.05	0.02	0.00

*SE= Specific Energy, SD= Specific deflection

Same lower case letters in the same column mean no statistical significant difference and vice versa.

Same capital letters in the same row mean no significant statistical significant difference and vice versa.

Source: **Own creation**

4.2.1.2 Composites reinforced with eucalyptus fibres

For samples reinforced with eucalyptus pulps, identical trends to those observed for samples reinforced with pine pulp are found at both 28 days and after ageing treatment. Samples made out of PC present the highest MOR values at 28 days (11.24 MPa) but these values severely decrease after ageing (7.69 MPa) since bleached fibres are more susceptible to degradation. Samples with MgO-SiO₂ cement, as happened for samples reinforced with pine pulp, initially present lower MOR values with higher SE at 28 days (9.23 MPa and 5.40 kJ/m² respectively), although no statistical reduction of the SE occurs after ageing. This behaviour is exceptional since this conservation of the toughness after ageing is produced for the toughest formulation (5.07 kJ/m²

after ageing). This higher toughness observed for samples reinforced with eucalyptus may be linked to their morphological properties (TONOLI et al., 2010). As it can be seen in

Figure 10, average length and width of eucalyptus fibres is considerably inferior to pine. Thus, for the same mass of reinforcing material, more reinforcing elements are dispersed within the matrix. This generates more reinforcing points to prevent cracking incidence (TONOLI et al., 2010). Also, from Figure 30, it is displayed a better dispersion of the eucalyptus fibres, avoiding the presence of unreinforced regions and, therefore, the propagation of major cracking before MOR is achieved.

Table 19- BD, WA and AP results of every formulation at 28 days and after 200 cycles of accelerated ageing

		BD* (g/cm ³)		WA* (%)		AP* (%)	
		28 days	200 acc	28 days	200 acc	28 days	200 acc
MgO-SiO ₂ - Pine	\bar{x}	1,39 a, A	1,46 a, B	30,13 a, A	27,49 a, B	42,55 a, A	38,92 a, B
	σ	0,03	0,03	0,58	0,56	0,49	0,86
MgO-SiO ₂ - Eucalyptus	\bar{x}	1,52 b, A	1,52 b, A	24,97 b, A	22,51 b, B	38,11 b, A	34,68 b, B
	σ	0,02	0,02	0,65	0,71	0,65	0,65
PC - Pine	\bar{x}	1,54 b, A	1,57 c, A	25,19 b, A	20,28 c, B	38,94 b, c, A	32,54 c, B
	σ	0,03	0,01	0,94	0,61	1,05	0,73
PC - Eucalyptus	\bar{x}	1,52 b, A	1,56 d, B	26,82 c, A	18,06 d, B	39,51 c, A	29,71 d, B
	σ	0,02	0,03	1,20	0,80	0,65	0,81

*BD= Bulk Density, WA= Water Absorption, AP= Apparent Porosity.

Same lower case letters in the same column mean no statistical significant difference and vice versa.

Same capital letters in the same row mean no significant statistical significant difference and vice versa.

Source: **Own creation**

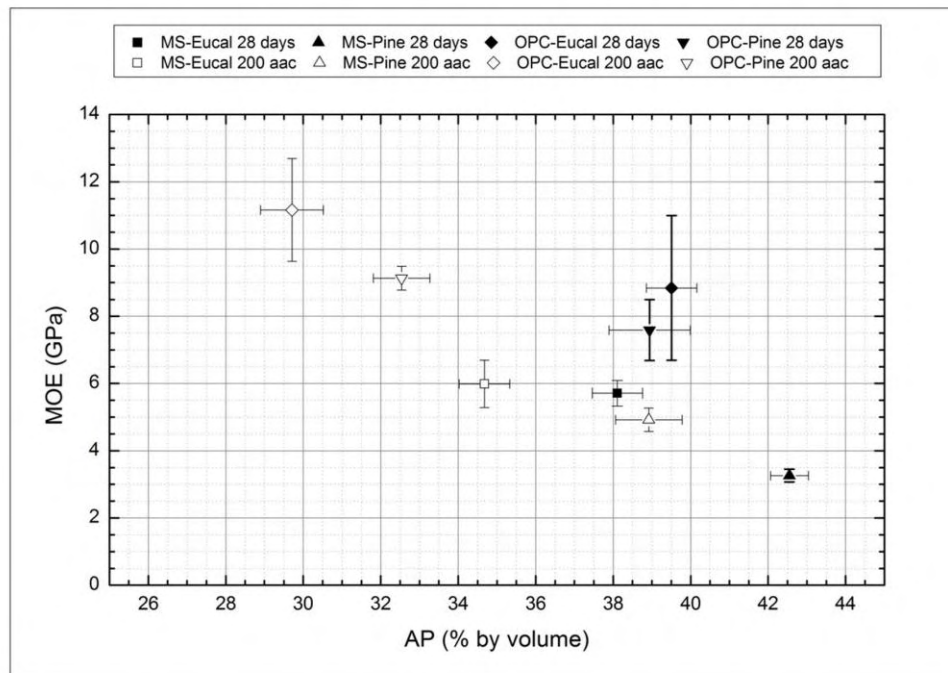
Another disclosed aspect from flexural tests is the fibre preservation achieved by using low alkaline cement. It is reported that bleached pulps are more prone to chemical degradation due to their lower lignin content (MOHR; NANKO; KURTIS, 2005). Lignin acts as a barrier: being the first pulp component to suffer alkaline attack and consequently saving cellulose and hemicellulose initially from this deterioration. Such observation is noticeable by a drastic reduction of the SE (from 4.97 to 0.14 kJ/m⁻²) for the samples of PC. Considering that the formulation where MgO-SiO₂ cement and eucalyptus pulp are used present the higher SE and SD results, at 28 days and after ageing, it can be concluded that this type of material does not suffer a chemical degradation. In spite of the

reduction of the SE, this is not statistically meaningful, and the reduction of specific deflection may be linked to the modification of the fibre-matrix interface due to a matrix densification.

4.2.2 Apparent porosity vs MOE

From Figure 24 it is possible to appreciate a clear trend relating the decrease of apparent porosity with the increase of MOE. For every formulation, it is noted that samples experiment a decrease of the apparent porosity after ageing, accompanied by an enhancement of MOE. As previously mentioned this can be related to an improvement of the binder performance, since cement hydration continues after 28 days (ARDANUY; CLARAMUNT; TOLEDO FILHO, 2015; NOGUCHI et al., 2009). Thus, the matrix becomes less porous which improves the mechanical performance (MOE in this case) (CHEN; WU, 2013). The same situation can be proposed for the samples made out of MgO-SiO₂ cement (ZHANG; VANDEPERRE; CHEESEMAN, 2014), as the hydration happens gradually, since the reaction of the SiO₂ particles with Mg²⁺ ions takes place over time, because the hydration of MgO is needed to release ions and this process is not immediate (THOMAS; MUSSO; PRESTINI, 2014). The increase in matrix rigidity may modify the fibre-matrix interface, and this phenomenon can be attributed to the apparent porosity reduction. According to the graph, PC samples experience greater porosity reduction than MgO-SiO₂ samples after ageing. This may be due to the larger amount of water retained within the MgO-SiO₂ matrix after moulding (Table 8), which once the samples are set becomes void volume (CHEN; WU, 2013). This excess of water, added to the water absorbed by the vegetable fibres, generates an excess of voids that results into a less resistant material. The only case where water demand does neither imply a statistical difference in AP nor MOE is for PC samples at 28 days. However, the same trend observed for the rest of the samples is also noticed for PC after ageing.

Figure 24- Average values of modulus of elasticity (MOE) vs. apparent porosity (AP) of samples at 28 days and after 200 accelerated ageing cycles for both types of cement: MgO-SiO₂ (MS) and Portland cement (OPC). Horizontal and vertical lines indicate the standard deviation of every sample



Source: Own creation

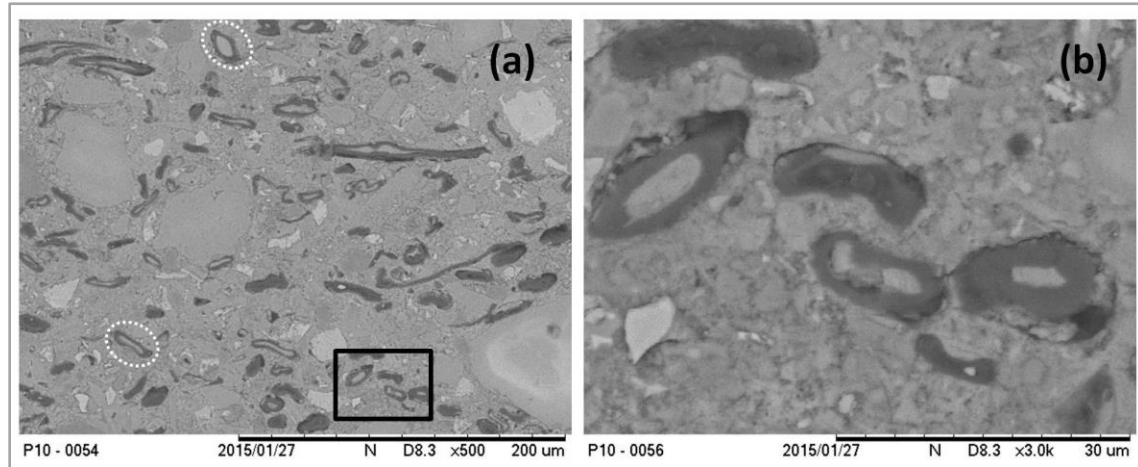
4.2.3 SEM analysis

From SEM analysis it is possible to see that in samples with Portland cement, vegetable fibres undergo mineralization after 200 aac. Figure 25 shows many eucalyptus fibres with the lumen filled with hydration products (encircled in white) after ageing. Also in Figure 25, there is a region (black square) that is zoomed for a better observation of this event. By EDS characterization it is inferred that there is a high concentration in Ca(OH)₂ in the lumens of the eucalyptus fibres, since it is detected a high presence of Ca (green dots in Figure 26) and insignificant concentration of Si (blue dots). This situation may be explained by the bleached nature of the eucalyptus used in this study. While lignin is blocking the entrance of the ions in the lumen and pores of the pine fibre (Figure 26), the absence of lignin in the chemical composition of eucalyptus pulp may produce an increase of the fibres permeability, which also increases the ingress of Ca²⁺ and OH⁻ ions that settle with time to produce Ca(OH)₂ crystals, as proposed by Tonoli et al. (2012). Contrarily to what happens with samples with Portland cement and reinforced with eucalyptus fibres, when samples are reinforced

with pine pulp, the lumen of the fibres suffer much less mineralization, since unbleached pulp contain a higher percentage of lignin (Table 6) that helps with blocking the entrance of hydration products inside the lumen (Figure 27). For this type of reinforcement no trace of $\text{Ca}(\text{OH})_2$ penetrates into the inner regions of the fibres and rather stays surrounding the outer region of the fibres

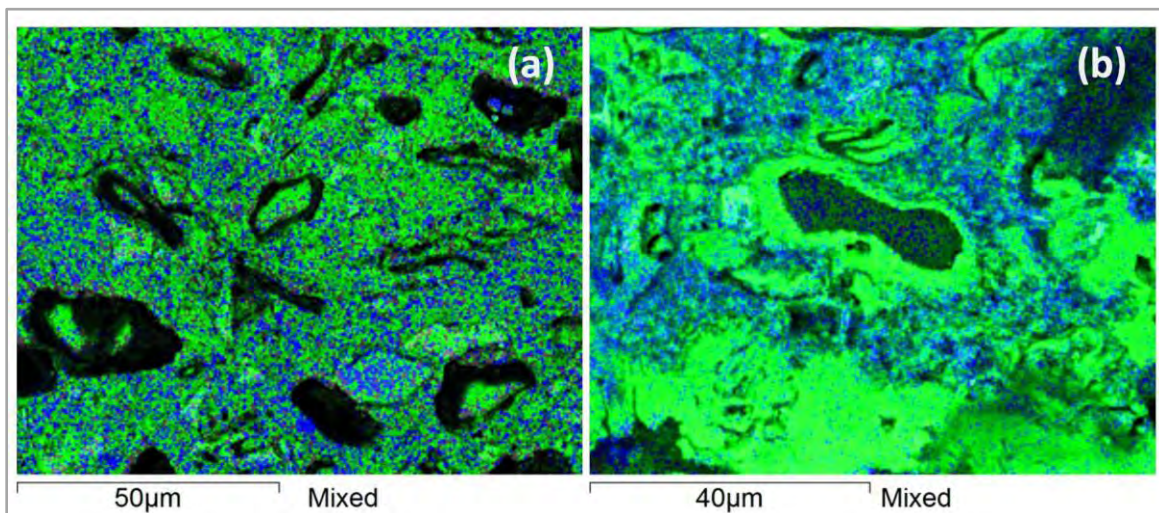
In the zoomed region (Figure 27), high portlandite concentration regions are found in the surroundings of the fibres. This may be justified, in contrast to what happens for bleached pulps, by pine pulps nature. The pine fibres used in these samples are unbleached and thereby the presence of lignin could act as a hydrophobic barrier for water not to accede to the interior of the fibres (TONOLI et al., 2012). However an adsorption phenomenon takes place and together with the water release of the fibres with time generates regions with high content in water in the vicinity of the reinforcing elements. This provokes the dissolution and precipitation of the $\text{Ca}(\text{OH})_2$ on the surface of the fibres, which may explain the decay of the mechanical performance after accelerated ageing (MELO FILHO; SILVA; TOLEDO FILHO, 2013; TOLEDO FILHO et al., 2009; WEI; MEYER, 2014). However it is possible to notice that the mineralization of the fibre, as in the case of eucalyptus fibre, is more destructive (based on loss of both MOR and SE) than the degradation provoked by portlandite in the external surface of the fibre (as in the case of Pine).

Figure 25- SEM images of polished surfaces of a composite made out of Portland cement and reinforced with eucalyptus microfibrils after 200 cycles of accelerated ageing. In (a), white dashed lines encircle microfibrils with the lumen filled with hydration products. Black square stands for a zoomed region depicted in (b). (b) represents a zoomed region of (a), where the lumens of the fibres are clearly mineralized and filled with hydration products after 200 cycles of accelerated ageing



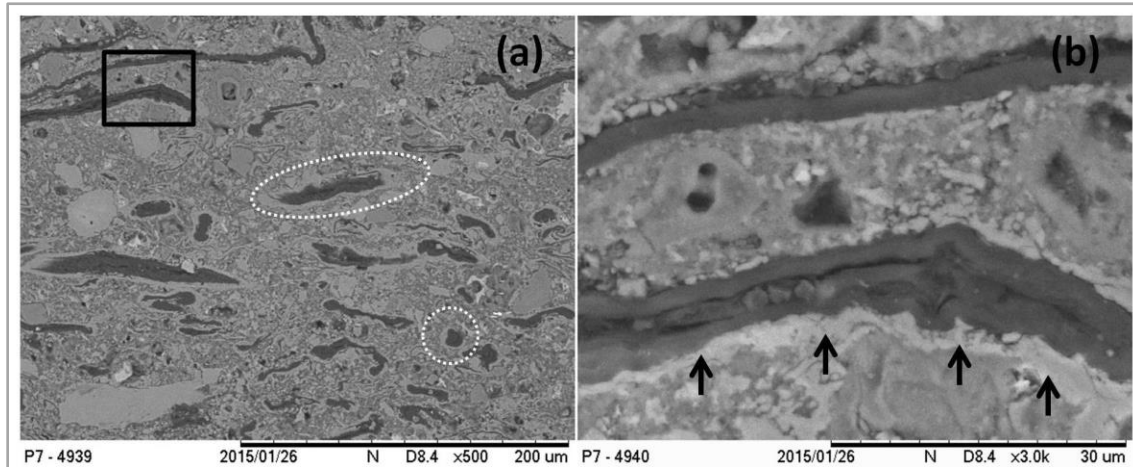
Source: Own creation

Figure 26- EDS mapping of a composite made out of Portland cement and reinforced with eucalyptus (a) and pine (b) microfibrils after 200 cycles of accelerated ageing. Green dots represent Ca mapping. Blue dots represent Si mapping



Source: Own creation

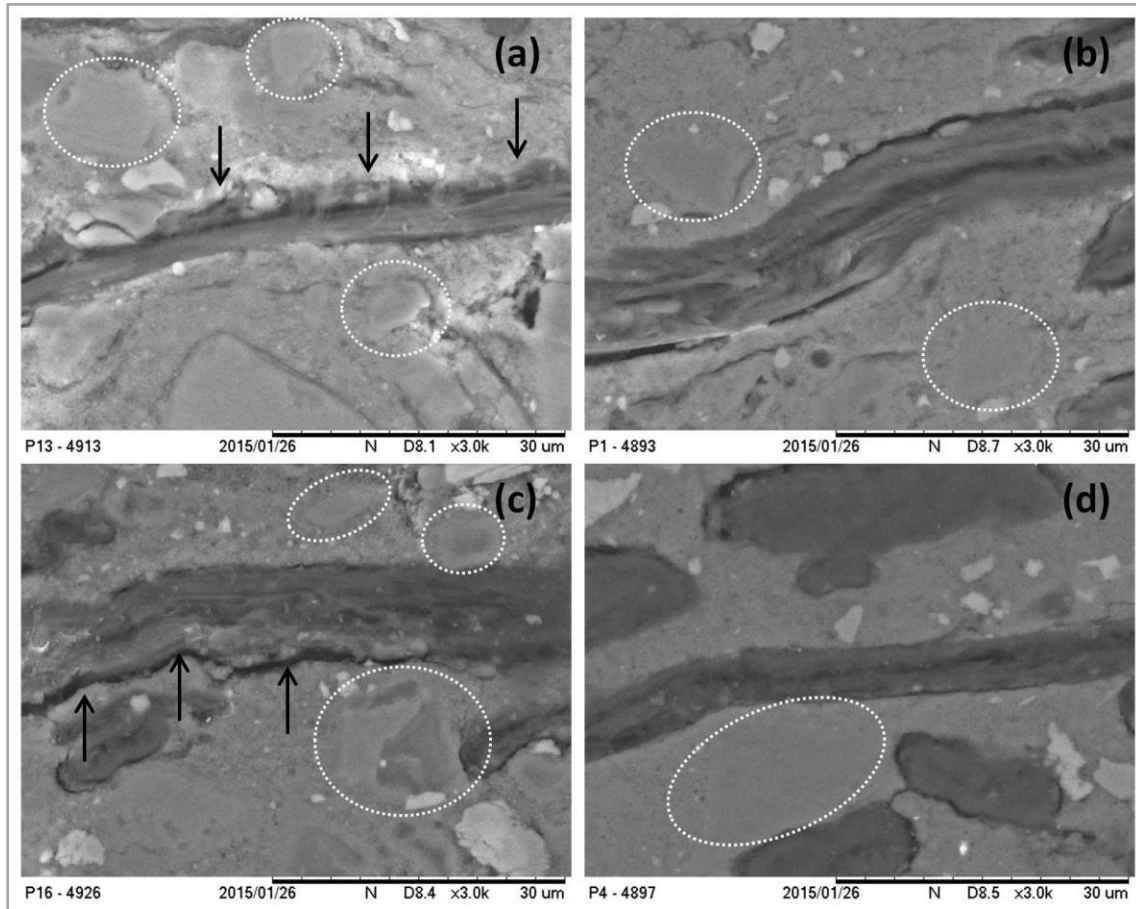
Figure 27- SEM image of a polished surface of a composite made out of Portland cement and reinforced with pine microfibres after 200 cycles of accelerated ageing. In (a), white dashed lines encircle microfibres surrounded by hydration products. Black square stands for a zoomed region depicted in (b). (b) represents a zoomed region of (a), where black arrows are pointing to the fibre-matrix interface where higher concentrations of $\text{Ca}(\text{OH})_2$ are present (light grey areas surrounding the fibres) after 200 cycles of accelerated ageing



Source: Own creation

Regarding samples where MgO-SiO_2 cement is used a different behaviour can be appreciated. In Figure 27, the surrounding area of a reinforcement fibre is displayed and it is possible to distinguish clearly the presence of $\text{Mg}(\text{OH})_2$ crystals at 28 days of age (encircled in white). Compared to samples after 200 aac, a remarkable difference is observable. It is possible to detect that the amount of $\text{Mg}(\text{OH})_2$ crystals after 200 acc is reduced. This may be a consequence of the evolution of the hydration reaction with time, where $\text{Mg}(\text{OH})_2$ particles react with anhydrous SiO_2 to form additional M-S-H gel. An effect of the continuity of the reaction over time is the densification of the matrix after ageing which would explain the reduction of the SE after ageing (Table 18) although no morphological evidence of degradation of the fibres can be observed. At 28 days, Figure 28 shows noticeably regions where matrix and fibre are debonded (black arrows). After 200 cycles of accelerated ageing (JIN; AL-TABBAA, 2014; SZCZERBA et al., 2013), fibre-matrix interface is modified and the gap between the cement matrix and the reinforcement is considerably reduced. Another outcome from matrix densification is the reduction of the water absorption and porosity of the samples for both types of reinforcement (Table 19).

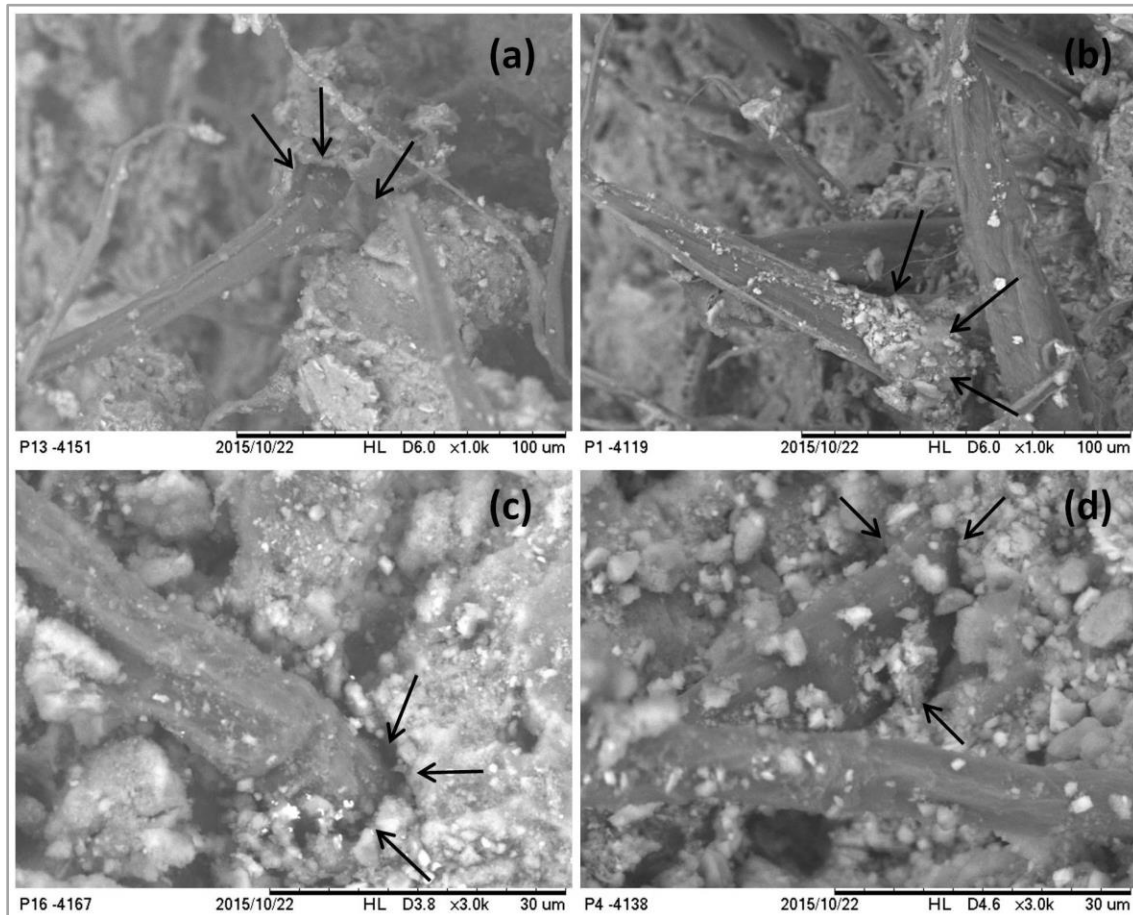
Figure 28- SEM images of polished surfaces of composites made out of MgO-SiO₂ cement and reinforced with pine microfibres at 28 days (a) and after 200 accelerated ageing cycles (b) and eucalyptus microfibres at 28 days (c) and after 200 accelerated ageing cycles (d). White dashed lines encircle brucite crystals. Black arrows point to debonded regions of fibre-matrix interface



Source: Own creation

Also in Figure 29 it is possible to see how matrix densening affects the fracture mechanism. From Figure 29a, where a surface of fracture is depicted from a MgO-SiO₂ composite sample reinforced with pine pulp at 28 days, it is present an obvious space between hydration products and reinforcement element. However after accelerated ageing, Figure 29b, hydration products are totally attached to the surface of the fibre.

Figure 29- Surface of fracture of composites made out of MgO-SiO₂ cement and reinforced with pine microfibres at 28 days (a) and after 200 accelerated ageing cycles (b) and eucalyptus microfibres at 28 days (c) and after 200 accelerated ageing cycles (d). Black arrows point to the fibre-matrix interface



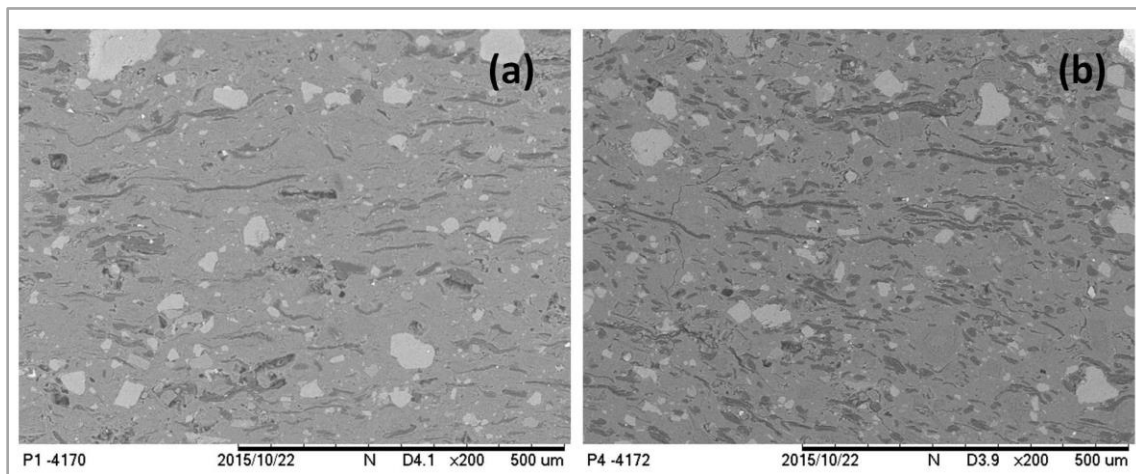
Source: Own creation

This phenomenon is not important for samples reinforced with eucalyptus fibre (Figure 29c and Figure 29d). The reduction in the space between fibre and matrix is not as relevant as it is for samples reinforced with pine pulp, probably due to the lower water/cement associated to the lower water retention of the eucalyptus fibres. At 28 days, Figure 29c, the surface of fracture does not present a clear debonding of the fibre, generating energy dissipation by pull-out, showing no matrix damage. This behavior is also present after ageing, Figure 29d, in preserving fibre-matrix interface.

From SEM analysis, another aspect that can be explained is the different reinforcement behavior related to the different types of pulp. According to Figure 10 it can be deduced that for the same mass of reinforcement, a greater amount of eucalyptus reinforcement elements is present when compared to pine fibres since eucalyptus pulp has shorter and thinner microfibres. This is in

accordance to Figure 30, where polished surfaces of samples reinforced with pine and eucalyptus. From these images it can be seen how the composite reinforced with eucalyptus pulp Figure 30b presents greater number of reinforcing elements than the corresponding ones reinforced with pine pulp, Figure 30a. This may explain the different SE presented for both types of reinforcement (Table 18). Consequently, the higher number of reinforcing elements implies higher energy dissipation (at least in the initial ages).

Figure 30- SEM image of a polished surface of a composite made out of MgO-SiO₂ cement and reinforced with pine (a) and eucalyptus (b) microfibres



Source: **Own creation**

4.3 BLOCK 3

4.3.1 XRD analysis

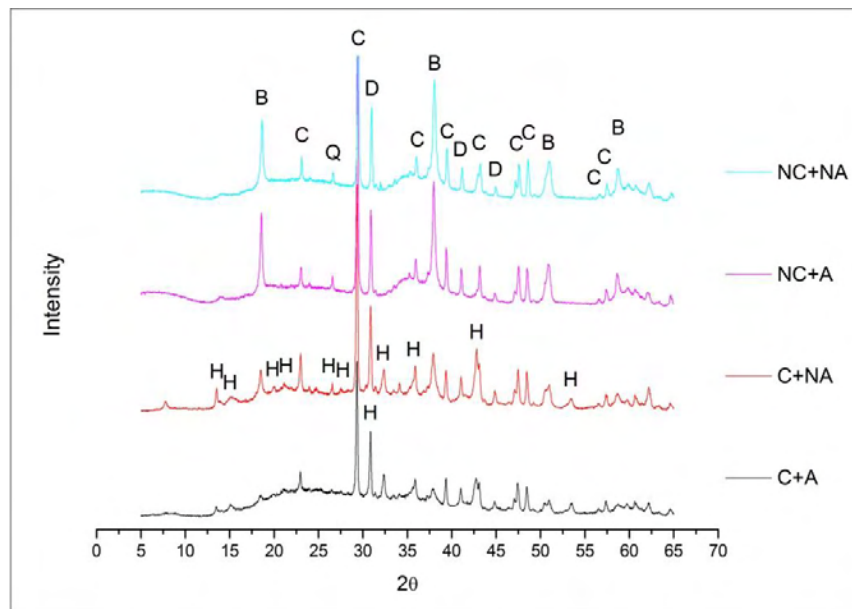
Carbonation curing effectiveness is confirmed by XRD tests. In Figure 31, it is shown for uncarbonated treatments, both non-aged (NC+NA) and aged (NC+A) that the main crystalline phase, apart from calcite (limestone), is brucite whose peaks are clearly detected at around 18, 38 and 58° 2θ. However, those brucite peaks for carbonated samples, non-aged (C+NA) and aged (C+A), present a lessened intensity while new crystalline phases corresponding to hydromagnesite are present [1–6]. Although many of the characteristic peaks corresponding to hydromagnesite XRD patterns are overlapped with either dolomite or calcite peaks (30.9, 35.8 and 43° 2θ), there are other peaks in Figure 31 very characteristic from hydromagnesite only present in carbonated samples (at 13.7, 15,

20 and 26.5° 2θ). It is expected that under the carbonation curing conditions (20% of CO₂, 45°C and 90% RH) hydromagnesite is formed following this reaction:



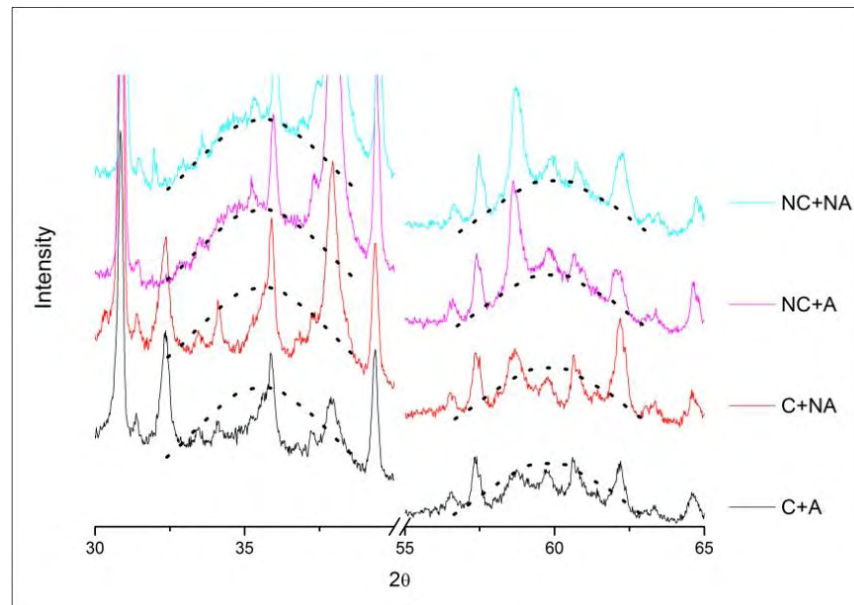
The lowering of the brucite peaks is even more significant for carbonated samples after accelerated ageing (C+A). Since the drying stage of the accelerated cycles is carried out at 60°C, this temperature promotes the formation of more hydromagnesite crystals over time once the process is started, even at atmospheric CO₂ concentration. Another consequence is the partial carbonation of the M-S-H gels under higher CO₂ concentration curing. According to several studies, in the intervals between 32-39° and 53-63° 2θ a hump corresponding to M-S-H gels (LI et al., 2014; LOTHENBACH et al., 2015; SZCZERBA et al., 2013; WALLING et al., 2015) is expected. The presence of this hump is confirmed for non-carbonated samples (NC+NA and NC+A) (Figure 32). Nonetheless for carbonated samples (C+NA and C+A) the expected hump is plainly reduced in these regions confirming the reduction of the gel content.

Figure 31- XRD diffractograms of the different formulations studied: Uncarbonated-Unaged (NC+NA), Uncarbonated-Aged (NC+A), Carbonated-Unaged (C+NA) and Carbonated-Aged (C+A). Peaks marked are brucite (B), calcite (C), quartz (Q), Dolomite (D) and hydromagnesite (H). Smaller peaks are not marked since they correspond to traces of reinforcing elements



Source: Own creation

Figure 32- XRD diffractograms of the different formulations studied: Uncarbonated-Unaged (NC+NA), Uncarbonated-Aged (NC+A), Carbonated-Unaged (C+NA) and Carbonated-Aged (C+A) for the regions where broad bumps due to M-S-H gels are expected to appear. Dotted curves in black represent the gel bumps



Source: Own creation

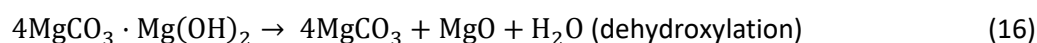
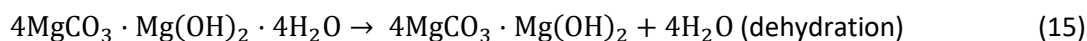
4.3.2 TG and DTG analysis

From TG curves displayed in Figure 33, the effect of carbonation curing is proved by an increased mass loss of the formulations with high CO_2 concentration curing, both unaged and aged (C+NA and C+A) compared to the non-carbonated samples (NC+NA and NC+A). This augment in mass loss may be linked to the decomposition of the hydrated products formed during the curing at high CO_2 concentration.

Carbonated samples show similar DTG curves (Figure 34) to uncarbonated samples, presenting 4 well defined peaks for both treatments at around 105-135, 410-422, 450-459 and 777-786°C. Those last two peaks, centred at around 455 and 780°C, correspond to polypropylene and limestone filler decomposition respectively. Polypropylene thermal disintegration is a single process that initiates at about 334°C and it ends at 493°C, achieving its maximum degree at 452°C, with a mass loss about 99.3 wt %, and an insignificant residual mass of 0.7 wt % (PĂRPĂRIȚĂ et al., 2014). The almost complete disintegration of polypropylene justifies the presence of a peak in spite of its low weight in the formulation (2 wt %). Thermal decomposition of calcite single crystals, is produced

in the following reaction, $\text{CaCO}_3(\text{s}) \rightarrow \text{CaO}(\text{s}) + \text{CO}_2(\text{g})$, starting at $T \sim 600^\circ\text{C}$ and completed at around 850°C ; after losing 44 wt% matching to the stoichiometric CO_2 amount in CaCO_3 (RODRIGUEZ-NAVARRO et al., 2009). Cellulose decomposition, main component of the unbleached pine pulp, is not well defined since it is decomposed at a single stage about 363°C (SHEN et al., 2013) which is overlapped with a major peak. Cellulose also has a mass loss of 56 wt % and a reduced presence in the formulation (3 wt %) that makes difficult to quantify its disintegration from Figure 33.

The effect of accelerated carbonation curing is clearly observed by differential thermogravimetry analysis. Comparing carbonated and uncarbonated samples DTG curves (Figure 34) two clear new peaks appear for the carbonated samples at around 260 and 520°C , corresponding to decomposition of hydromagnesite (BOTHÁ; STRYDOM, 2001; HAURIE et al., 2007; HOLLINGBERY; HULL, 2010a, 2010b, 2012; VÁGVÖLGYI et al., 2008), which is the main product obtained as a consequence of the carbonation reactions. The temperature range in which hydromagnesite decomposition takes place varies from 220 and 550°C and it can be divided in three different stages, according to equations (15-17): (15) release of lattice water in the temperatures range of 220 – 290°C , (16) dehydroxylation occurred in the range of 375 – 470°C and (17) decarbonation from 470 to 550°C . Thus the observed peak at 260°C may be associated to the first stage while the peak observed at 520°C corresponds to the third step.



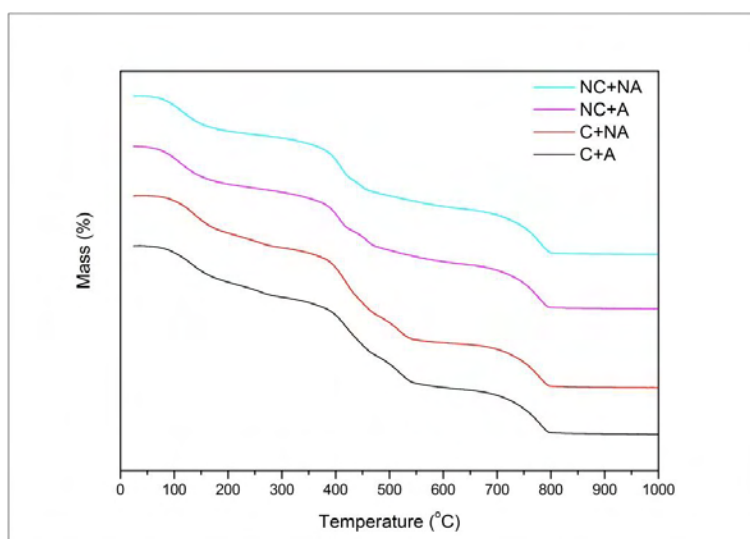
Apart from these new peaks, the displacement of the peaks at around 110 and 410°C for uncarbonated samples may be attributed to carbonation curing. The dislocation of the peak from 410 to 425°C can be related to the transfer of part of the OH^- groups from $\text{Mg}(\text{OH})_2$ to hydromagnesite, since main brucite dehydroxylation happens at around 400°C (WANG et al., 2014) while dehydroxylation for hydromagnesite occurs at around 430°C (BEALL et al., 2013; HAURIE et al., 2007). Regarding the peak centred at 110°C , attributable to the loss of loosely bound interlayer water in M-S-H gels (LI et al., 2014; LOTHENBACH et al., 2015; SZCZERBA et al., 2013; WALLING et al., 2015), it is possible to conclude that it has been displaced up to higher temperatures due to a partial carbonation of the gel induced by the high CO_2 concentration. This phenomenon has also been reported for Portland cement pastes (ROSTAMI et al., 2012), where C-S-H phase is disarranged

by carbonates and C-S-H containing relatively high carbon content is detected by Energy Dispersive Spectroscopy (EDS). Though unusually present in nature, it is possible to find carbonate-altered serpentine rocks (listwanite), from a natural CO₂ sequestration process through minerals carbonation (HANSEN et al., 2005). This process of carbonation of the serpentine crystals has been backed by experimental studies on a similar but simpler (MgO-SiO₂-H₂O-CO₂) system (BJERGA; KONOPÁSEK; PEDERSEN, 2015; KLEIN; GARRIDO, 2011; KLEIN; MCCOLLOM, 2013). A possible explanation for this occurrence is the formation of a serpentine-carbonate crystal from M-S-H gel, analogue to talc-carbonates described in (BJERGA; KONOPÁSEK; PEDERSEN, 2015).

On the other hand, no evidences of MgCO₃ are confirmed by the thermogravimetry in this study. During magnesite decomposition a large endothermic peak centred at around 630–660°C occurs, yet it does not appear for none of the formulations studied (Figure 34). Only tiny traces of magnesite are noticed in this study and they come from the decarbonation of dolomite present in limestone filler.

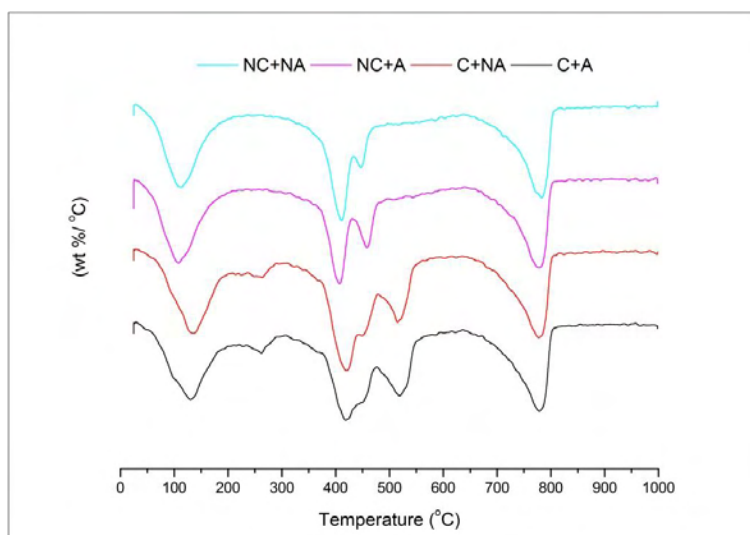
Comparing samples before and after accelerated ageing, no significant mass loss variations are identified by the thermogravimetry tests (Figure 33). Thus, hydration phases for both carbonated and uncarbonated samples are stable. This is especially relevant for carbonated products, given that after 100 accelerated ageing cycles the mass loss remains the same as immediately after curing.

Figure 33- TG curves of the different formulations studied: Uncarbonated-Unaged (NC+NA), Uncarbonated-Aged (NC+A), Carbonated-Unaged (C+NA) and Carbonated-Aged (C+A)



Source: Own creation

Figure 34- DTG curves of the different formulations studied: Uncarbonated-Unaged (NC+NA), Uncarbonated-Aged (NC+A), Carbonated-Unaged (C+NA) and Carbonated-Aged (C+A)



Source: **Own creation**

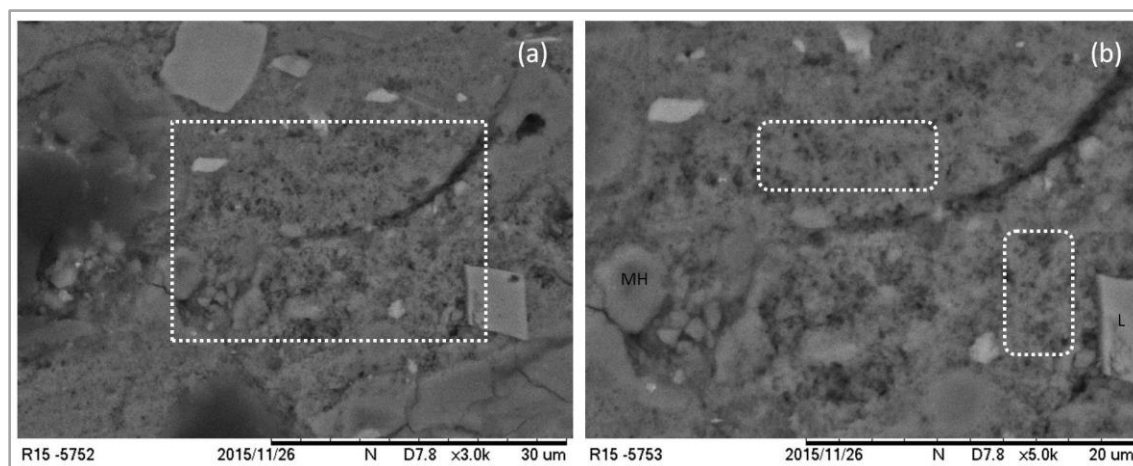
4.3.3 SEM

By means of SEM analysis, it is also possible to establish the effectiveness of the high CO_2 concentration curing. Figure 35 shows an image of a fractured surface of a non-carbonated sample after ageing, where it is possible to find the typical hydrated phases of the system $\text{MgO-SiO}_2\text{-H}_2\text{O}$: Mg(OH)_2 and M-S-H gels (JIN; AL-TABBAA, 2014; LI et al., 2014; SZCZERBA et al., 2013; ZHANG; CHEESEMAN; VANDEPERRE, 2011; ZHANG; VANDEPERRE; CHEESEMAN, 2014). Particles of polypropylene and limestone are also present in Figure 35. M-S-H gels are clearly observed (encircled in white), showing a mesoporous (gel and capillary pores) poorly crystallized structure with a resemblance with Calcium Silicate Hydrate(C-S-H) gels produced during Portland cement hydration.

However, carbonated samples after 100aac present additional structures unnoticed before carbonation curing (Figure 36). Apart from Mg(OH)_2 and M-S-H gels, rosette shaped crystals are evident (encircled in yellow). In line with different authors (BEALL et al., 2013; CHEN et al., 2015; GAUTIER et al., 2014; LI et al., 2003; SUTRADHAR et al., 2011), this crystals morphology is in accordance to hydromagnesite shape which is described as rosette-like microstructure with crystalline walls interconnected to each other (Figure 36). Also, the hydromagnesite used by Chen

et al. (CHEN et al., 2015) for the synthesis of forsterite matches the exhibited dimensions to those presented by the crystals of hydromagnesite in Figure 36, with extremely thin sheets of around 20 nm in thickness and less than 1 μm inside length.

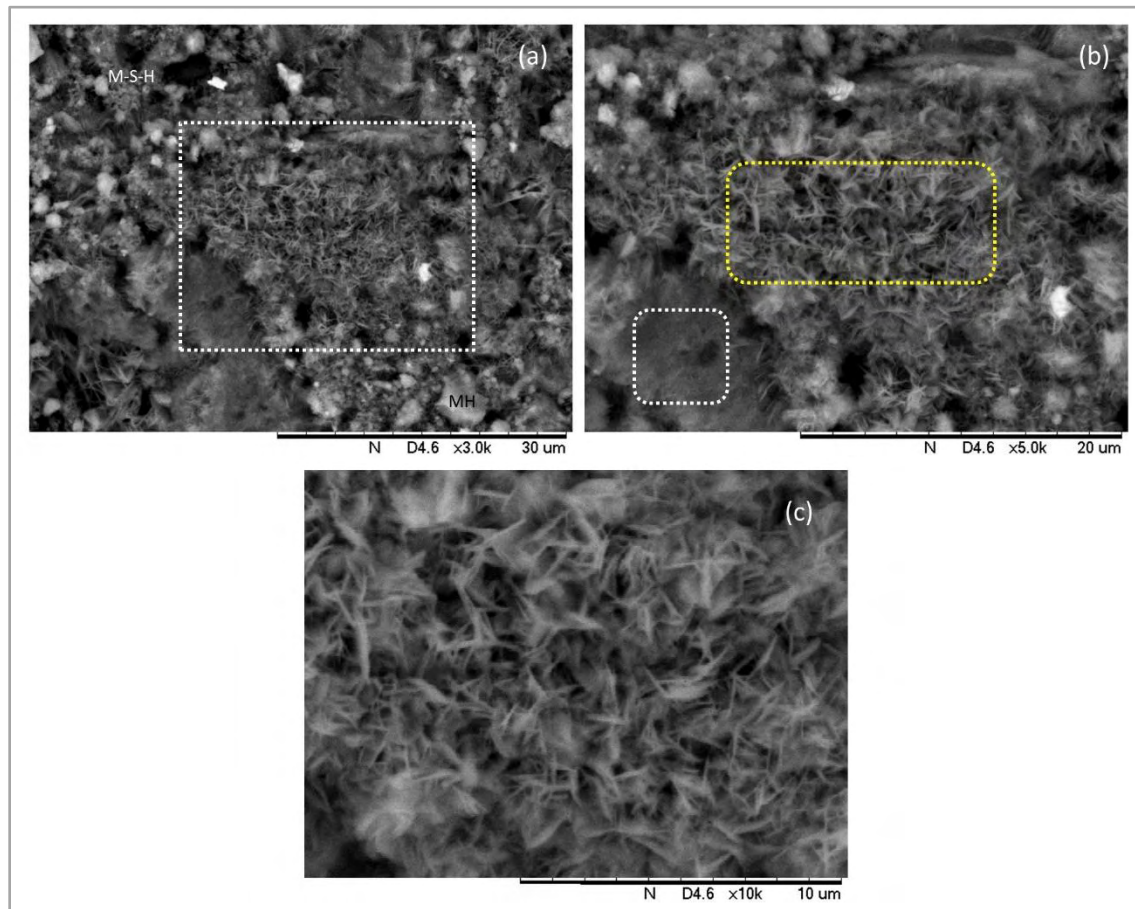
Figure 35- (a) is a SEM of a fractured surface of uncarbonated samples. The white dashed line square is the zoomed area depicted in (b). MH, L and PP stand for $\text{Mg}(\text{OH})_2$, limestone and polypropylene respectively. The white dashed lines show M-S-H gels. All images are for aged composites after accelerated aging test



Source: **Own creation**

From Figure 36, it is also possible to detect a more compacted amorphous structure (marked in white). This structure is visibly different from both hydromagnesite and bigger than the rest of hydrated magnesium silicate, typical from the reaction between MgO and amorphous SiO_2 in water. Although the unavailability of micrographic information in the literature, the presence of two different amorphous phases is in line with XRD results, where part of the M-S-H gel disappear in carbonated samples giving origin to new compounds. The existence of these new particles may be interpreted as the result of the carbonation of M-S-H gels, supporting the hypothesis constructed from XRD results.

Figure 36- (a) SEM of a fractured surface of carbonated samples. The white dashed line squares the zoomed are depicted in (b). The white dashed lines show crystals produced after M-S-H carbonation. The yellow dashed line is the zoomed area depicted in (c), exhibiting hydromagnesite crystals. All images are for aged composites after accelerated aging test



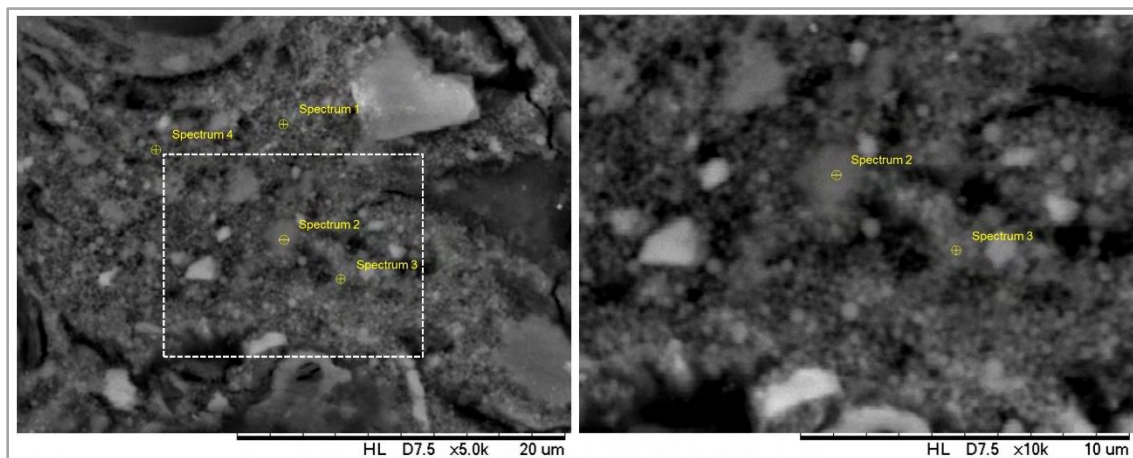
Source: Own creation

4.3.4 EDS analysis

EDS is carried out in order to better identify the effects of the of carbonation curing on M-S-H gels. Using this technique, the Mg/Si ratio of M-S-H gel areas is measured for both carbonated and non-carbonated samples in order to determine the chemical relation between Mg and Si of these compounds. In Figure 37 carbonated samples exhibit M-S-H gels with larger particles, such as Spectrum 2, compared to the rest of marked spectra. In Figure 37b, zoomed area from Figure 37a, the region around Spectrum 2 presents a clearly larger structure with a particle size between 1.5-2.5 μm, in contrast with the area around Spectrum 3, where smaller particles are observed (150-300 nm). Heeding the Mg/Si atomic ratio of the different considered spectra (Table 20), the value

for Spectrum 2 is 1.41, which is close to the value of lizardite or antigorite $[\text{Mg}_3(\text{Si}_2\text{O}_5)(\text{OH})_4]$, showing a higher magnesium concentration than the areas with presence of smaller particles of M-S-H gel (0.67-0.82).

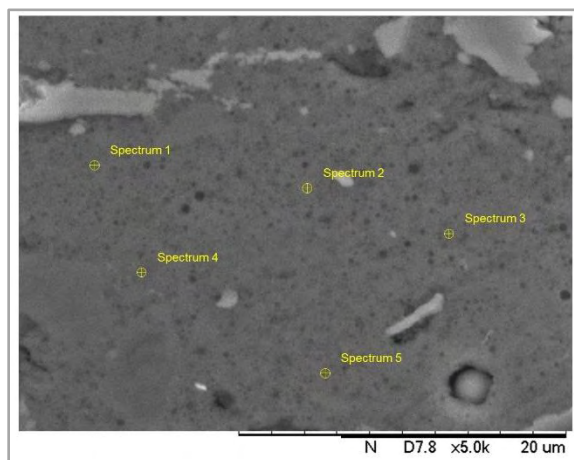
Figure 37- SEM image of a polished surface of a Carbonated composite after accelerated ageing with the different analyzed spectra. In (a), white dashed lines encircle zoomed in (b). (b) represents a zoomed region of (a), where different types of M-S-H gels are shown



Source: Own creation

From Figure 38, where non-carbonated samples are displayed, a more homogenous matrix is observed, and for any region of the matrix the range of gel composition lies between Mg/Si atomic ratio 1.31-1.47. This value matches the value of the bigger particles in carbonated samples (Figure 37). Therefore, it can be assumed that high CO_2 environments affect M-S-H particles composition, reducing their Mg/Si atomic ratio and, hence, releasing Mg^{2+} ions that, in presence of free water, are susceptible of being carbonated into hydromagnesite.

Figure 38- SEM image of a polished surface of a Non-carbonated composite after accelerated ageing with the different analyzed spectra



Source: Own creation

This decrease in Mg/Si ratio, from 1.31-1.47 to 0.67-0.82, involves an alteration in the chemical composition of the gels, changing from an arrangement like lizardite or antigorite to talc $[\text{Mg}_3\text{Si}_4\text{O}_{10}(\text{OH})_2]$ or sepiolite $[\text{Mg}_4\text{Si}_6\text{O}_{15}(\text{OH})_2 \cdot 6\text{H}_2\text{O}]$. This composition similar to sepiolite may account for the increase in temperature of the endothermic peak observed in DTG analysis from 110 to 135°C (Figure 34), since the loss of zeolitic and surface water of the sepiolite takes place up to 220°C, showing a peak centred about 125-135°C (BALCI, 1996; RUIZ et al., 1996; SHUALI, 1990). On the other hand, particles with lower Mg/Si values in Figure 37 show small structures, justifying the absence of large peaks in Figure 31, since the presence of sepiolite should result in an intense peak around 7.3°. The presence of small crystals also yields broader peaks in XRD. However, carbonated samples show a decrease of the intensity of the humps between 32-39° and 53-63° 2θ, there is an increase in the bump from 15 to 40° 2θ. This is in accordance to Cornejo and Hermosín (CORNEJO; HERMOSIN, 1988), who generated a structural alteration of sepiolite by grinding. This crushing causes a destruction of the original tetrahedral-octahedral linkage of the sepiolite and generates an amorphous material, which produced a pronounced bump from 15 to 40° 2θ. Besides, the alternation produced by grinding also increased the temperature of the endothermic peak from 105 to 135°C which is also confirmed in Figure 34.

Table 20-Average EDS values of the amorphous phases for the Uncarbonated and Carbonated samples after ageing. For Carbonated samples, EDS values are grouped considering the different compound sizes. 50 spectrums are considered for each average values

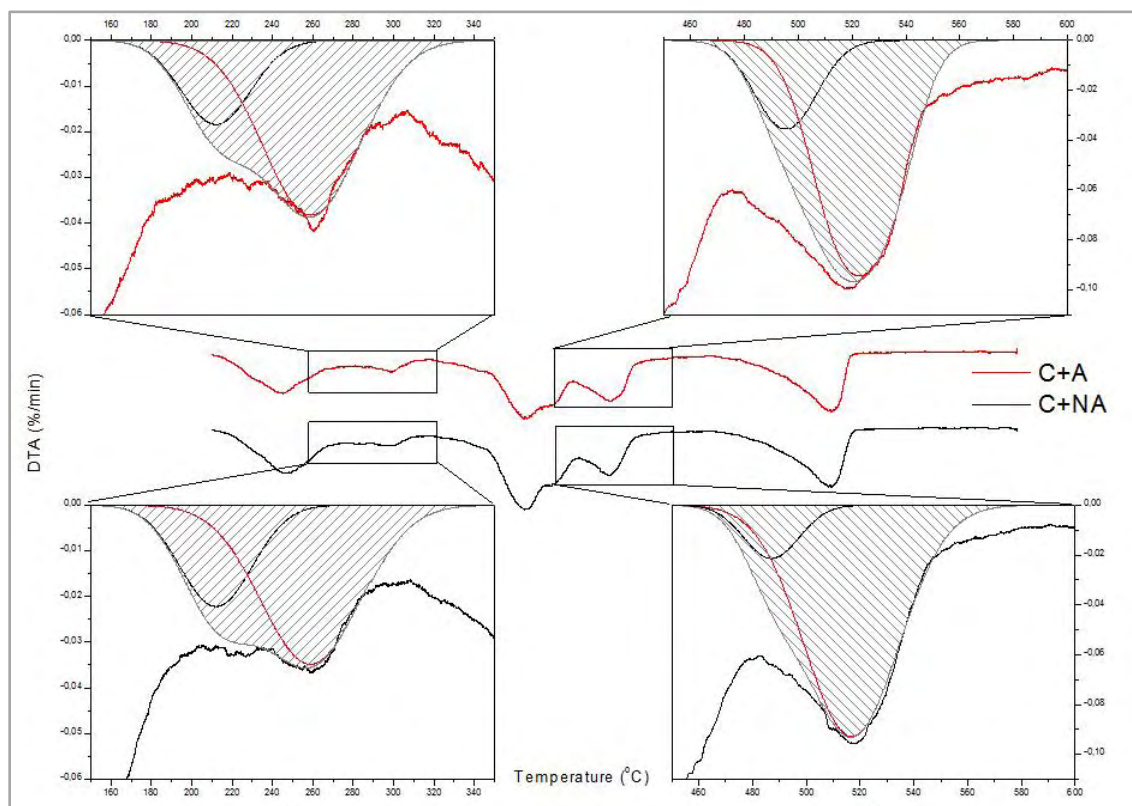
Uncarbonated + Aged Samples					
	Element	Weight %	Weight % σ	Atomic %	Mg/Si
M-S-H	Magnesium	16.391	0.344	11.490	1.45
	Silicon	13.076	0.302	7.935	
Carbonated + Aged Samples					
	Element	Weight %	Weight % σ	Atomic %	Mg/Si
Small particles	Magnesium	11.335	0.348	7.984	0.71
	Silicon	18.514	0.480	11.288	
Big particles	Magnesium	14.334	0.312	9.959	1.41
	Silicon	11.705	0.276	7.040	

Source: **Own creation**

4.3.5 Hydrated Magnesium Carbonates (HMC) thermodynamic stability

In order to study thermodynamic stability of the HMC formed after carbonation curing, DTG curves are analysed before (C+NA) and after ageing (C+A), according to Figure 39. In this figure, the two major peaks present only in carbonated samples are zoomed. These peaks are related to the dehydration and decarbonation of hydromagnesite. Based on the endothermic peaks from differential scanning calorimetry, the DTG peaks between 160-340°C and 450-580°C can be deconvoluted into two minor Gaussian curves that match the different stages of both dehydration and decarbonation. The combinations of these Gaussian curves fitted the area of the obtained DTG and are used to determine the mass loss in each process. Nevertheless, the mass loss associated to hydromagnesite dehydroxylation, in the range of 375-470°C, is difficult to be established since the loss of (OH)⁻ from hydromagnesite is overlapped with the mass loss of hydroxyl groups from Mg(OH)₂ (at around 410°C for non-carbonated samples) partially present in the matrix. Besides polypropylene decomposition occurs between 334 and 493°C, which hinders the intensity quantification of the peak for each component in the range of 400 and 450°C.

Figure 39- DTG peak analysis of carbonated samples after ageing (C+A) and non-aged (C+NA) on the specific regions where HMC dehydration and decarbonation occur



Source: Own creation

The quantification of the peak area for each decomposition stage is shown in Table 21. From these results no reduction is likely to take place for each peak after ageing. Although a tiny decrease in area is produced, from 3.14 to 3.05 (Table 21), in the dehydration peak for aged samples (C+A), the area obtained from HMC decarbonation for aged samples is higher than for non-carbonated samples, increasing from 4.68 to 5.04 (Table 21). Considering the total area corresponding to both decomposition processes, this value is also higher for aged samples which is in accordance with a reduction of $\text{Mg}(\text{OH})_2$ for carbonated samples after ageing (C+A), as proved by XRD (Figure 31). Considering that the ageing cycles used in this study simulates severe weather conditions, including intense temperature variations (from 20 to 60°C in 10 min), it is possible to affirm that no reverse reaction from carbonated to uncarbonated phase happens. Probably the reasonable explanation for this product stability is that the main HMC crystal found in this study keeps a major resemblance with hydromagnesite instead of nesquehonite, as stated by Unluer and Al-Tabbaa (UNLUER; AL-

TABBAA, 2014) and after discussed elsewhere (UNLUER; AL-TABBAA, 2016; WALLING; PROVIS, 2016).

Table 21- Parameters of the different Gaussian curves obtained to quantify the mass loss from dehydration and decarbonation processes of the HMC in both peaks. Xc, w, A and AT stand for center of the curve, full width at half maximum, area and total area. C+A and C+NA are the aged and unaged carbonated samples respectively

1 st range (160-340°C)							
1 st peak			2 nd peak				
	Xc (°C)	w (°C)	A (mass loss %)	Xc (°C)	w (°C)	A (mass loss %)	A _T (mass loss %)
C+A	212	40.07	0.78	259	55.76	2.27	3.05
C+NA	212	42.13	0.99	259	57.8	2.15	3.14
2 nd range (450-580°C)							
1 st peak			2 nd peak				
	Xc (°C)	w (°C)	A (mass loss %)	Xc (°C)	w (°C)	A (mass loss %)	A _T (mass loss %)
C+A	495	26.37	1.00	525	39.29	4.04	5.04
C+NA	487	24.24	0.55	517	41.76	4.13	4.68
Total mass loss %							
C+A							8.09
C+NA							7.82

Source: **Own creation**

4.3.6 Mechanical and physical tests

According to 4 points bending test results, carbonation has a plain influence on the mechanical properties. Although non-significant differences may be observed, both carbonated samples (unaged and aged) present higher MOR and lower SE values (Table 22). Concerning the matrix performance and, thus, the cement mechanical properties, the flexural parameters that offer the conclusive information are MOE and LOP (BENTUR; MINDESS, 2007). Regardless carbonation, both formulations suffer a statistical significant reduction of MOE after ageing: approximately 25% and 38% for carbonated and uncarbonated respectively. This loss of rigidity may be associated to the conversion of Mg(OH)₂, that is the result of the expansive reaction from MgO and H₂O, into other hydrated phases: M-S-H gels for uncarbonated samples (JIN; AL-TABBAA, 2014; LI et al., 2014; SZCZERBA et al., 2013; ZHANG; CHEESEMAN; VANDEPERRE, 2011; ZHANG; VANDEPERRE; CHEESEMAN, 2014) and magnesium carbonates for carbonated samples (BOTHÁ; STRYDOM, 2001, 2003; FERNÁNDEZ et al., 1999; NDUAGU et al., 2012; UNLUER; AL-TABBAA, 2014). In spite of the reduction of the stiffness in carbonated samples after ageing, carbonation has a positive effect on the matrix since LOP increases at the same age. The end of the elastic region (LOP) in fibre-cement composites is considered as the maximum load that is resisted mainly by the cementitious matrix

(BENTUR; MINDESS, 2007). Consequently, an increase in LOP can be related to an improvement of the mechanical strength of the matrix. In view of the results, carbonation of the MgO-SiO₂ systems in composites with vegetable fibres enhances the mechanical performance of the cement.

Compared to previous works where carbonation of Portland cement is used to improve and preserve the mechanical properties of cementitious products reinforced with vegetable fibre (ALMEIDA et al., 2013), MOR results obtained in this study are lower. These differences in MOR values may be due to lower short fibres content (3% in this study compared with 10% used by (ALMEIDA et al., 2013) which generates a different number of reinforcing elements. However, the values reported by Almeida et al. showed lower values of specific energy compared with those obtained in this work, which can be attributed to the content of long fibres, polypropylene, allowing greater energy dissipation by pull-out. In this study, the energy absorbed during bending test is conserved without loss of deformation and resistance. These results are consistent with those obtained by Khorami et al (KHORAMI; GANJIAN; SRIVASTAV, 2016) where samples reinforced with PP fibres experienced a large deformation due to the large tensile deformation of these fibres. However according to Khorami et al, PP fibres did not provide a satisfactory performance as reinforcing elements, since in spite of improving ductility and toughness, flexural strength declined.

In another work where PP fibres and pulp pine are used as reinforcement elements of fibre-cement (BEZERRA; JOAQUIM; SAVASTANO JR, 2004), mechanical results are lower than those obtained in this experiment, for both MOR and SE. This indicates the efficiency of the matrix used in this study and the viability to use PP as reinforcement fibres, which generally provide ineffective mechanical performance.

The parameter that decreases in a significant manner for both carbonated formulations is SD. This phenomenon is commonly associated to the modification of the interfacial transition zone (ITZ) between matrix and fibre. Though carbonation has been reported to have a positive filling effect and to reduce porosity in cement composites, it also densifies the ITZ (PIZZOL et al., 2014; SANTOS et al., 2015a). This fact is also reinforced by the significant reduction of the apparent porosity after carbonation (Table 24), achieving a decline of the porosity of up to 38%, and simultaneously increasing the bulk density of the whole composite. The densification of the ITZ is one of the causes of the fracture mechanism modification in fibre-reinforced cementitious products (TOLEDO FILHO et al., 2000; SAVASTANO; WARDEN; COUTTS, 2005), where less-dense interfaces are

prone to pull-out and thus energy absorption, while denser transition zones trend to higher fibre-matrix adherence, promoting the fibre collapse.

Another possible explanation for the reduction of SD is the first tension that fibre reinforcements begin to resist. Considering the statistical higher LOP values for carbonated samples, reinforcement elements within these formulations are initially loaded at superior levels than in the case of non-carbonated samples at the first cracking episode. Thus, the fact of beginning to resist higher tension values makes those fibres in carbonated samples do not elongate as much as fibres in non-carbonated samples. However, this ductility lessening does not affect the toughness of the carbonated samples since there is no significant difference between carbonated samples and uncarbonated samples for both aged and unaged samples.

Table 22- Modulus of rupture, specific energy (at MOR) and specific deflection (at MOR) values for the different studied formulations. $MOR = \frac{P_{max} \cdot L}{b \cdot h^2}$. $SE = \frac{\int F \cdot d\epsilon}{b \cdot h}$ and $= \frac{\epsilon}{L}$; where Pmax is the maximum load applied on the material, L is the major span between supports, b is the width of the sample, h is the thickness of the sample and ϵ is the registered deformation

		MOR (MPa)		SE (kJ/m ²)		SD (mm/mm)							
		Unaged	Aged	Unaged	Aged	Unaged	Aged						
Uncarbonated	\bar{x}	12.22	a, A	12.30	a, A	7.67	a, A	10.27	a, A	0.112	a, A	0.152	a, B
	σ	0.53		1.36		1.48		2.21		0.02		0.02	
Carbonated	\bar{x}	13.24	a, A	13.84	a, A	8.07	a, A	8.79	a, A	0.105	b, A	0.107	b, A
	σ	1.55		1.87		3.12		3.91		0.03		0.04	

Same lower case letters in the same column mean no statistical significant difference.
Same capital letters in the same row mean no significant statistical significant difference.

Source: **Own creation**

Table 23- Modulus of elasticity and limit of proportionality for the different studied formulations. $MOE = \frac{276 \cdot L^3}{1296 \cdot b \cdot h^3} \cdot m$ and $= \frac{P_{LOP} \cdot L}{b \cdot h^2}$; where PLOP is the maximum load applied in the elastic region, L is the major span between supports, b is the width of the sample, h is the thickness of the sample and m is the tangent of the curve (load vs. deflection) in the elastic region

		MOE (GPa)		LOP (MPa)	
		Unaged	Aged	Unaged	Aged
Uncarbonated	\bar{x}	5.529	3.418	7.31	4.76
	σ	0.29	0.99	0.87	1.07
Carbonated	\bar{x}	11.55	8.679	8.72	10.47
	σ	1.00	1.67	1.14	1.18

Same lower case letters in the same column mean no statistical significant difference.
Same capital letters in the same row mean no significant statistical significant difference.

Source: **Own creation**

According to physical tests, carbonation presents evident advantages for fibre-cement products (Table 24). The first benefit is the decrease of apparent porosity, which is especially important for fibre-cement elements reinforced with cellulosic fibres since products with less apparent pores are more effective against any chemical or biological attack (BENTUR; MINDESS, 2007). Another advantage is the decline of water absorption. This aspect is particularly useful for the main current application of fibre-cement products: roofing elements. Low water absorbent products are more resistant against freeze-thaw cycles (BENTUR; MINDESS, 2007) and water permeability, improving durability of building materials under direct exposure to the natural weather. Besides in this study by the application of accelerated ageing (100 soak-dry cycles), extremely aggressive environmental conditions are simulated, combining stages of high temperature (60°C) and low humidity (ventilated oven) with immersion (rainy) periods. The effect of carbonation of MgO-SiO₂ systems supposes an improvement that allows obtaining values of AP, BD WA and similar to those obtained with Portland cement composites (BEZERRA; JOAQUIM; SAVASTANO JR, 2004).

Table 24- Apparent porosity (AP), bulk density (BD) and water absorption (WA) values for the different formulations

		AP (% by volume)		BD (g/cm ³)		WA (% by mass)							
		Unaged	Aged	Unaged	Aged	Unaged	Aged						
Uncarbonated	\bar{x}	36.95	a, A	37.39	a, A	1.48	a, A	1.45	a, A	25.02	a, A	25.83	a, A
	σ	0.79		1.12		0.03		0.03		1.00		1.34	
Carbonated	\bar{x}	26.78	b, A	30.72	b, B	1.69	b, A	1.62	b, B	15.84	b, A	18.94	b, B
	σ	1.11		1.01		0.03		0.03		0.88		0.99	

Same lower case letters in the same column mean no statistical significant difference.

Same capital letters in the same row mean no significant statistical significant difference.

Source: **Own creation**

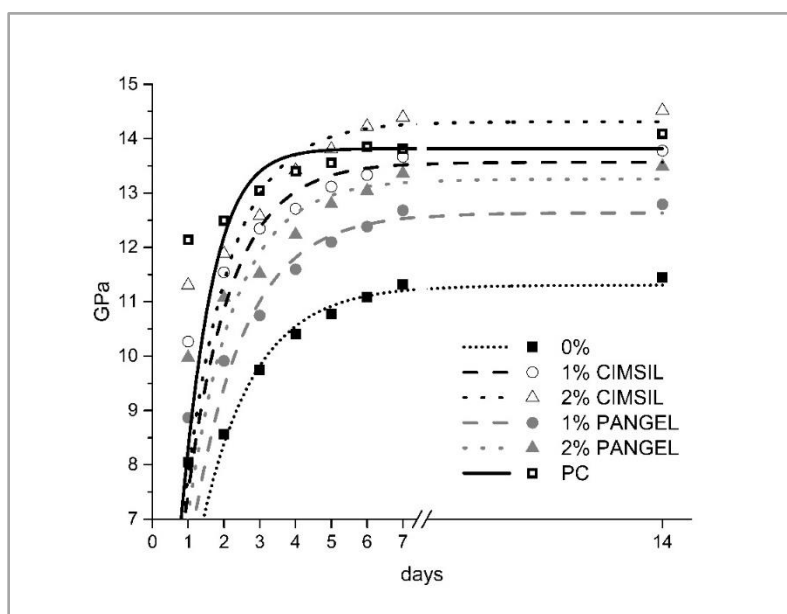
4.4 BLOCK 4

4.4.1 Paste tests

4.4.1.1 Hydration of the pastes and dynamic MOE results

From Figure 40, it is possible to observe how samples containing sepiolite increase MOE mean values regardless the amount and type of sepiolite. Comparing different types of sepiolite, samples with CIMSIL sepiolite present higher elastic modulus than samples with PANGEL. For both types of sepiolite samples the higher content in sepiolite the higher MOE values. PC samples have higher mean MOE values than MgO-SiO₂ samples but 2% CIMSIL is the treatment that presents higher values from day 5.

Figure 40- Evolution of hydrated pastes Dynamic Flexural Young Modulus over time with a steam curing at 55°C depending on the sepiolite replacement. 0% stands for MgO-SiO₂ samples with no sepiolite replacement. PC stands for PC cement samples used as a control samples. The rest of the samples indicate the percentage and type of sepiolite replacement.



Source: Own creation

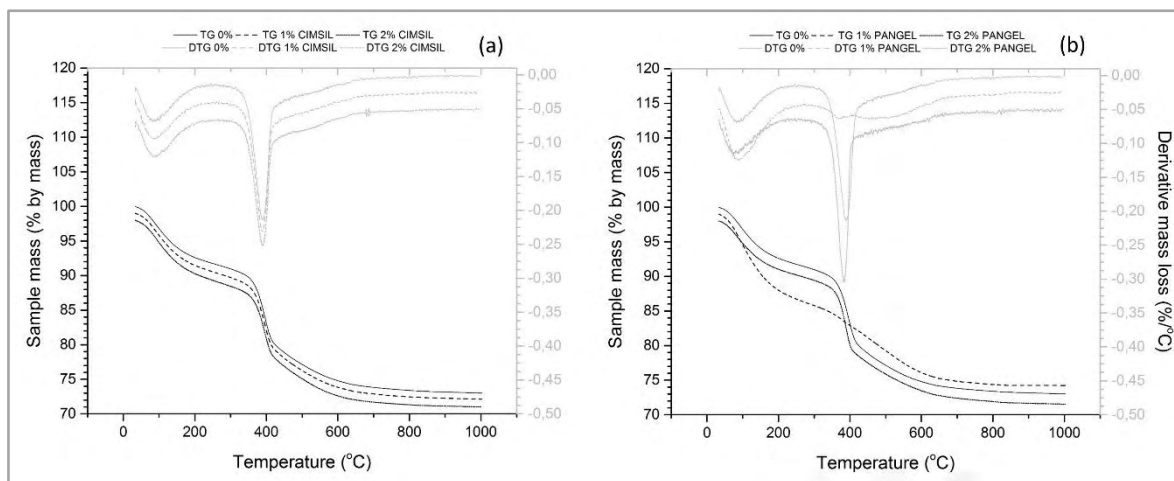
Regarding the hydration degree by comparing TG and DTG curves and XRD spectra (Figure 41 and Figure 42), samples containing CIMSIL sepiolite does not modify significantly the amount of hydrated phases compared to samples without sepiolite, though little reduction of unreacted MgO and MH is perceived and M-S-H gel content slightly increases. Although, the mechanical improvement of the pastes, the little chemical effect of CIMSIL sepiolite on the paste hydration confirms its inactivity as pozzolanic material (HE; MAKOVICKY; OSBÆCK, 1996).

Samples containing PANGEL sepiolite, however, clearly decreases the amount of unreacted MgO and MH with a well-defined increase in the M-S-H gel content. This is especially remarkable for 1% PANGEL samples, which does not show any trace of unreacted MgO in its spectrum and shows little peaks corresponding to MH, displaying an almost identical XRD spectra pattern and TG curve of M-S-H synthesized gel (BREW; GLASSER, 2005; LI et al., 2014; ZHANG; CHEESEMAN; VANDEPERRE, 2011; ZHANG; VANDEPERRE; CHEESEMAN, 2014). This may be explained because of the greater water demand either of PANGEL samples or due to the lower anionic charge. According to (ZHANG; VANDEPERRE; CHEESEMAN, 2014), where magnesium silicate hydrate (M-S-H) cement

pastes are obtained using sodium hexametaphosphate as deflocculant, samples with higher w/c ratio are expected to show a greater hydration degree at the same age. In this case, since its large specific surface, finer sepiolite provides wet condition that favors the magnesia-silica reaction, as happens with pozzolanic reaction (ANDREJKOVICŔVÁ, 2011).

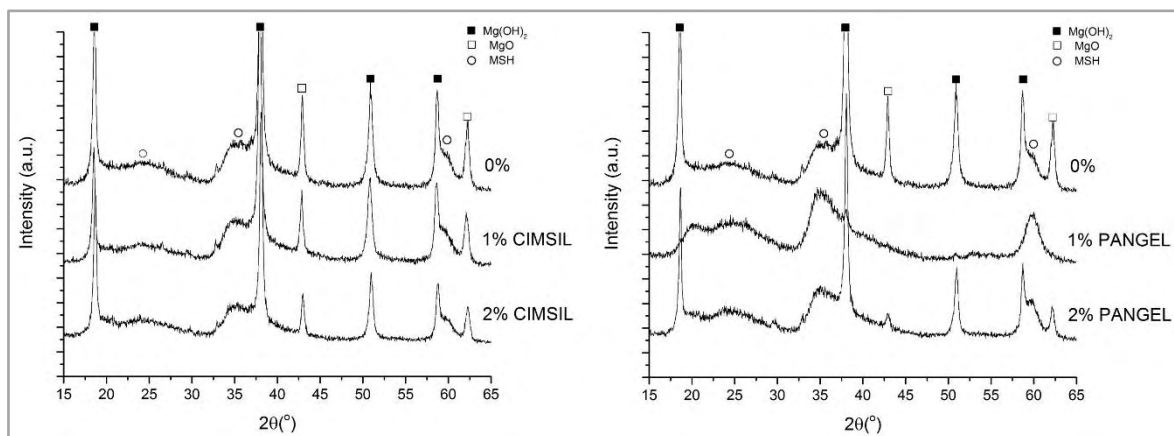
Also, the higher zeta-potential of CIMSIL has an electrostatic stabilizing effect upon the cement paste, thus reducing the hydration rate of these samples (NÄGELE; SCHNEIDER, 1989). Given the greater specific surface of PANGEL sepiolite (Table 10), this could act as a stronger nucleation seeding effect resulting in a faster hydration as it can be seen in Figure 43c, where needle-shaped particles of PANGEL sepiolite are tightly adhered on the surface of well-packed particles of M-S-H gels. This is also supported by (KAVAS; SABAH; ÇELIK, 2004) that reported the capability of sepiolite to absorb more alkaline compounds since its higher surface area. However, in the case of CIMSIL samples (Figure 43b), sepiolite microfibrils are linking loose M-S-H particles which suggests a prior gel growth and later physical attachment with the fibres.

Figure 41- TG and DTG results of the hydrated pastes depending on the type of sepiolite addition used: (a) CIMSIL (b) PANGEL. 0% stands for MgO-SiO₂ samples with no sepiolite replacement. The rest of the samples indicate the percentage and type of sepiolite replacement



Source: Own creation

Figure 42- XRD diffractograms of the hydrated pastes depending on the type of sepiolite addition used: (a) CIMSIL (b) PANGEL. 0% stands for MgO-SiO₂ samples with no sepiolite replacement. The rest of the samples indicate the percentage and type of sepiolite replacement



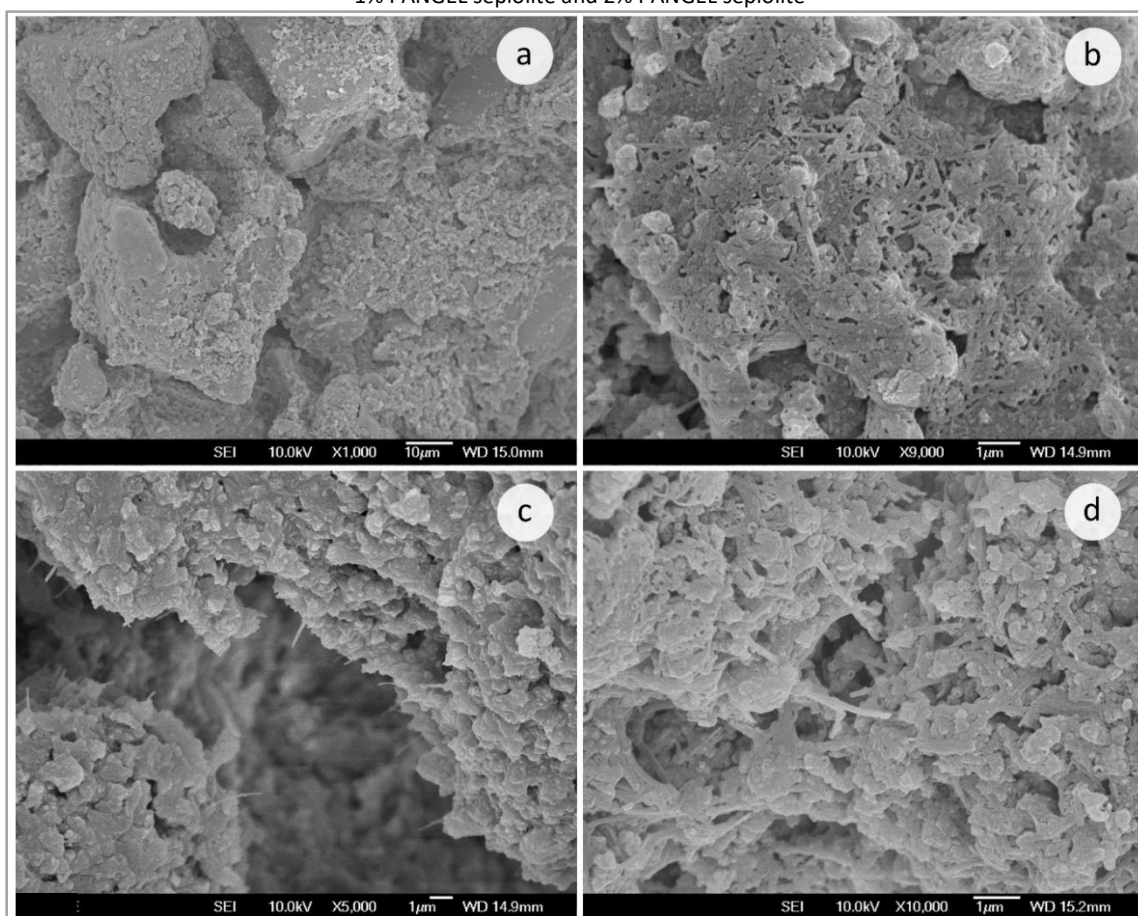
Source: Own creation

4.4.1.2 Paste micrographs

Figure 43a displays a MgO-SiO₂ sample with no sepiolite addition. In this image, a crust of M-S-H gel is surrounding bigger Mg(OH)₂ crystal particles (MH). These compounds are also displayed

in the rest of the images in Figure 43. In Figure 43b, where MgO-SiO₂ samples are dosed with 1% of CIMSIL sepiolite, plenty of needle shaped particles interconnect M-S-H gel particles and MH crystals. These acerosse particles match perfectly the size of sepiolite, 1-2 μm length and 0.2 μm width. It is also shown that hydrated products cover acicular particles. Figure 43c, referring to pastes where 1% PANGEL sepiolite is used, shows different sides of a fractured surface packed with M-S-H particles and sepiolite particles springing out in between. Figure 43d exhibits MgO-SiO₂ samples with 2% of PANGEL sepiolite, where M-S-H gel particles are interconnected with a 3D net created by sepiolite particles. Part of these sepiolite needles are covered by hydrated products while some others are not. This area with high concentration of sepiolite is openly porous in contrast with areas with more M-S-H particles.

Figure 43- SEM images of hydrated MgO-SiO₂ systems without sepiolite addition (a), with 1% of CIMSIL sepiolite (b), with 1% PANGEL sepiolite and 2% PANGEL sepiolite



Source: Own creation

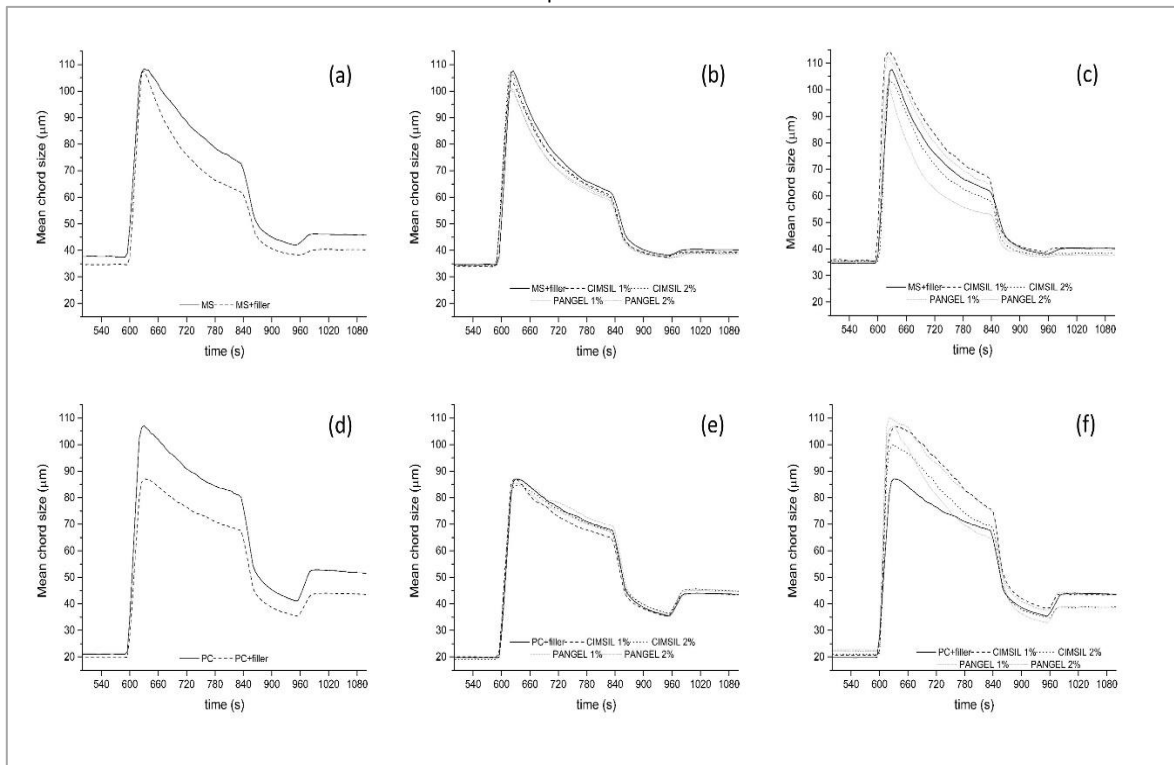
4.4.2 Composite tests

4.4.2.1 Flocculation tests

In Figure 44a, the chord size evolution of MgO-SiO₂ powder suspension is exhibited, revealing a mean size of 38 μm before flocculant addition and 109 μm after flocculant addition, which is the maximum mean chord size. Adding CaCO₃ to MgO-SiO₂ mixture slightly decreases the chord size before flocculant addition, and does not affect the chord size after flocculant addition and decreases floc stability, reducing chord size at deflocculation stage beginning (840 s). When undelaminated sepiolite is added to MgO-SiO₂ suspension (Figure 44b), chord size at every stage for every mix design slightly decreases, being further reduced for CIMSIL samples and 2% sepiolite content samples.

Figure 44- Evolution of the mean chord size of 18.4 g of powder suspensions in 400 mL of water according to Table 11.

Flocculation evolution is displayed in (a) for MgO-SiO₂ powder is displayed with and without filler addition, in (b) for MgO-SiO₂ powder with filler addition and undelaminated sepiolite replacements, in (c) for MgO-SiO₂ powder with filler addition and delaminated sepiolite replacements, (d) for PC is displayed with and without filler addition, in (e) for PC with filler addition and undelaminated sepiolite replacements and in (f) for PC with filler addition and delaminated sepiolite replacements

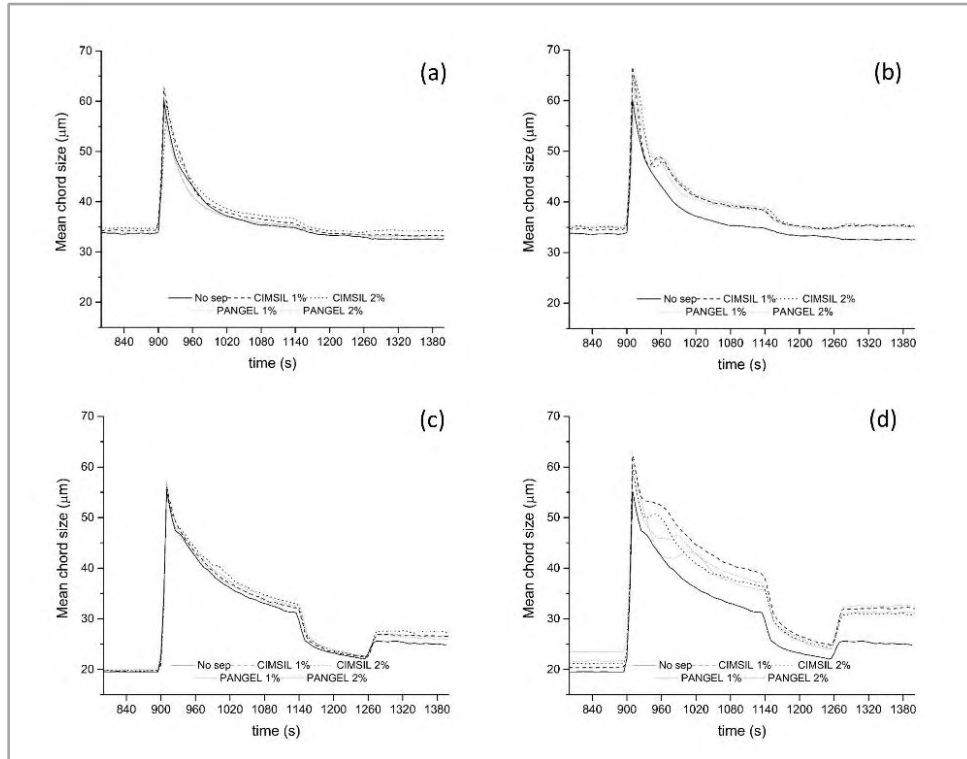


Source: Own creation

The addition of delaminated sepiolite to MgO-SiO₂ powder (Figure 44c) increases the chord size at the flocculation stage for 1% sepiolite gel content samples, while it is reduced for 2% sepiolite gel content samples. Shorter chord size is obtained when PANGEL sepiolite is used. When PC suspension is analyzed (Figure 44d), a mean chord size of 22 μm before flocculant addition and 108 μm after flocculant addition (max. chord size) is shown. Adding CaCO₃ to PC powder slightly decreases the chord size before flocculant addition (to 18 μm) and at every stage. In contrast to MgO-SiO₂ samples, undelaminated sepiolite in PC suspension (Figure 44e) does not significantly affect the chord size at any stage. However, when sepiolite is delaminated (Figure 44f), PC suspensions chord size is strongly increased at flocculation stage, boosted immediately after flocculant addition. More chord floc stability is achieved for 1% sepiolite gel content samples, keeping longer chord size even at the beginning of the deflocculation stage. Only 1% sepiolite gel content samples, both CIMSIL and PANGEL, retain higher chord size during deflocculation and keep it as high as control samples during reflocculation stages.

The addition of undelaminated sepiolite to MgO-SiO₂ powder dispersed in a pine pulp suspension is displayed in Figure 45a. Undelaminated sepiolite does not significantly affects the chord size after flocculant addition, however somewhat increases floc stability, yielding rather longer flocs after both deflocculation and reflocculation. Further chord size increase is achieved by CIMSIL samples. Contrarily to undelaminated sepiolite, delaminated sepiolite (Figure 45b) intensely rises chord size at every stage and shows similar performance for every formulation regardless sepiolite type and content. It also causes a reflocculation event during flocculation stage, after a faster floc size reduction and slight floc size regrowth. Considering the addition of undelaminated sepiolite to PC powder dispersed in a pine pulp suspension (Figure 45c), no significant effect is observed after flocculant addition, still slightly increases floc stability, yielding rather longer flocs during reflocculation. Little further chord size increase is displayed by CIMSIL samples and 2% sepiolite content samples. In the case of delaminated sepiolite in PC powder dispersed in a pine pulp suspension (d), chord size at every stage is intensely raised, regardless sepiolite type and content. As happened with MgO-SiO₂ suspension, a reflocculation event during flocculation stage, after a faster floc size reduction and slight floc size regrowth takes place.

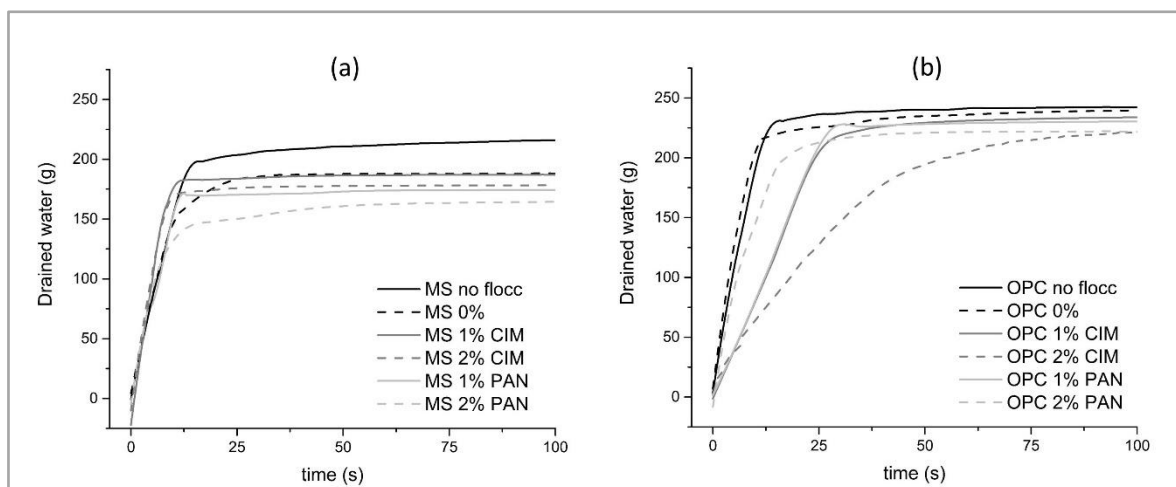
Figure 45- Evolution of the mean chord size of 18.4 g of powder + 1.6 g of pine pulp suspensions in 400 mL of water according to Table 11. Flocculation evolution is displayed in (a) in for MgO-SiO₂ powder with filler addition, undelaminated sepiolite replacements and cellulose pulp, in (b) for MgO-SiO₂ powder with filler addition and delaminated sepiolite replacements and cellulose pulp, in (c) for PC with filler addition, undelaminated sepiolite replacements and cellulose pulp and in (d) for PC with filler addition, delaminated sepiolite replacements and cellulose pulp



Source: Own creation

4.4.2.2 Drainage tests

Figure 46- Drainage curves displayed by the different fibre–cement slurries: (a) using MgO-SiO₂ powder and (b) using Ordinary Portland cement (PC)



Source: Own creation

Drainage curves for suspensions with both types of binder systems (Figure 46) display similar trend, with an initial rapid drainage where most of the water is drained, a transition zone from fast to low drainage and residual drainage, where horizontal asymptote is shown, keeping stable the drained water values over time. Comparing drainage curves of MgO-SiO₂ (a) and PC (b) suspensions, MgO-SiO₂ samples drain less water (ranging from 41-54%) compared to PC samples (55-60.5%), so MgO-SiO₂ matrices retain more water for every formulation. When flocculant to the suspensions, the amount of final drained water for both types of suspension is reduced, from 60.5 to 59.75 % for PC samples and from 54 to 47g for MgO-SiO₂ samples. However, it increases the drainage speed, rising the percentage of drained water after 10s from 79 to 85% for PC samples and from 71 to 78% for MgO-SiO₂ samples.

Considering the addition of delaminated sepiolite to MgO-SiO₂ mixture dispersed in a pine pulp suspension (Figure 46a) it is observed that it decreases the amount of drained water from the samples but for samples with 1% CIMSIL. The amount of drained water is mainly reduced by samples containing PANGEL sepiolite, where the greatest reduction is shown by 2% PANGEL sepiolite content. However, it increases the drainage speed, rising the amount of drained water after 10 s for every sample. When delaminated sepiolite is added to PC suspensions (Figure 46b), the amount of

drained water for every sample is reduced. Further drainage reduction is shown by 2% sepiolite content samples. Sepiolite in PC suspensions also reduces the drainage speed, dropping the amount of drained water after 10 s for every sample. 1% sepiolite content samples have similar drainage values (230 g aprox. after 100 s) and drainage speed after 10 s (35% aprox.). 2% PANGEL sepiolite content samples present faster drainage (65% after 10 s) compared to the rest of the samples with sepiolite addition, although the total amount of water (220 g after 100 s) is similar of the 2% CIMSIL sepiolite content samples, which have the slowest drainage at 10 s (29%).

4.4.2.3 Flexural tests

According to flexural tests, when MgO-SiO₂ cement is replaced in 1% by mass of CIMSIL sepiolite, all the mechanical parameters are increased except MOE. The rest of the replacements do not improve any parameter. The addition of sepiolite reduces the coefficient of variation for every studied parameter in most of the studied compositions. This is closely related to a more homogeneous composite. The only composition that is not in accordance with this trend is the one with 1% of PANGEL sepiolite. The properties related to the binder matrix rigidity (LOP and MOE) are more variable for this composition. The addition of PANGEL sepiolite yields lower flexural performance than CIMSIL sepiolite. Even at 2% by mass replacement, CIMSIL samples offer higher flexural properties compared to PANGEL samples.

Table 25 - Flexural results of every formulation after 5 days curing at 55°C. Modulus of rupture, limit of proportionality, specific energy (at MOR and 50% MOR), specific deflection (at MOR and 50% MOR) and modulus of elasticity values for the different studied formulations. $MOR = \frac{P_{max} \cdot L}{b \cdot h^2}$, $LOP = \frac{P_{LOP} \cdot L}{b \cdot h^2}$, $SE = \frac{\int F \cdot d\epsilon}{b \cdot h}$, $MOE = \frac{276 \cdot L^3}{1296 \cdot b \cdot h^3} \cdot m$ and $= \frac{\epsilon}{L}$; where P_{max} is the maximum load applied on the material, P_{LOP} is the maximum load applied in the elastic region, L is the major span between supports, b is the width of the sample, h is the thickness of the sample, ϵ is the registered deformation and m is the tangent of the curve (load vs. deflection) in the elastic region. 0% stands for MgO-SiO₂ samples with no sepiolite replacement. PC stands for PC cement samples used as a control samples. The rest of the samples indicate the percentage and type of sepiolite replacement

Sample		MOR (MPa)	LOP (MPa)	SE at MOR (J/m ²)	SE at 50% MOR (J/m ²)	Total SE (J/m ²)	MOE (MPa)	SD (mm/mm)	SE at 50% MOR (mm/mm)
PC	mean	9.47	5.13	3501	4599	5194	6389	0.077	0.101
	std dev	2.651	1.562	471	1409	1858	1946	0.013	0.017
	var coef (%)	22.46	23.44	13	29	33	22	20.64	20.66
0%	mean	9.36	4.29	2741	4316	4613	6105	0.060	0.094
	std dev	1.13	0.91	1143	1402	1391	1029	0.018	0.021
	var coef (%)	12.11	21.21	42	32	30	17	30.20	22.01
1% CIMSIL	mean	9.78	4.27	3471	5088	5544	5835	0.073	0.106
	std dev	0.75	0.48	713	1221	1182	743	0.013	0.023
	var coef (%)	7.67	11.30	21	24	21	13	18.30	21.78
2% CIMSIL	mean	9.22	4.57	2279	3595	4027	5513	0.053	0.082
	std dev	1.08	0.89	538	767	692	948	0.011	0.015
	var coef (%)	11.69	19.43	24	21	17	17	21.68	18.57
1% PANGEL	mean	8.56	3.52	2176	3396	3881	4942	0.053	0.082
	std dev	1.19	1.02	494	810	821	844	0.007	0.008
	var coef (%)	13.96	29.04	23	24	21	17	13.45	10.10
2% PANGEL	mean	9.00	3.84	2022	3288	3856	5715	0.047	0.076
	std dev	0.91	0.71	584	786	926	632	0.012	0.015
	var coef (%)	10.14	18.57	29	24	24	11	25.13	20.28

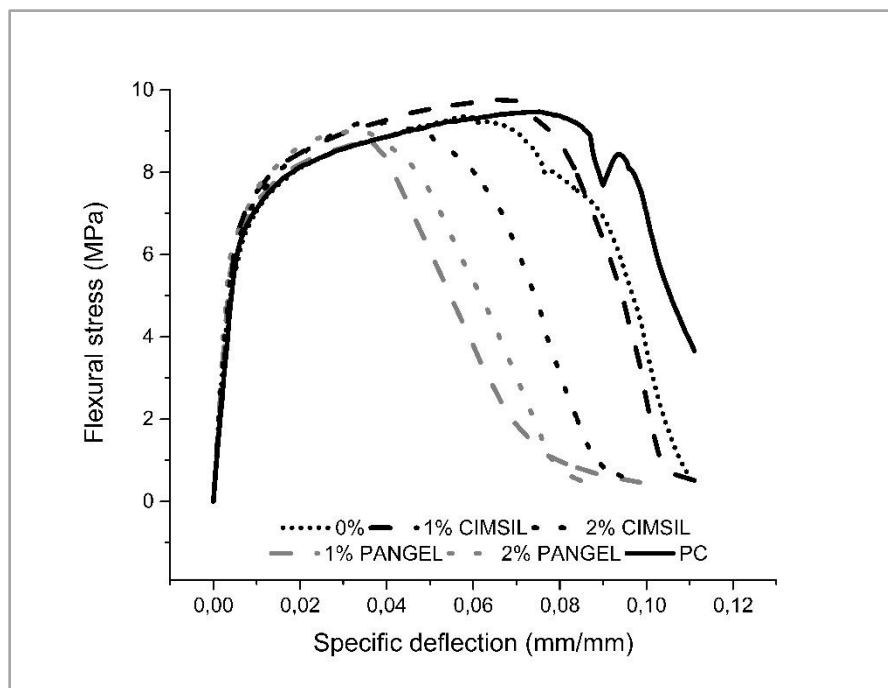
Source: Own creation

Considering the water retention after drainage (Figure 46), samples with 1% of CIMSIL sepiolite does not affect the drainage capacity of the composite compared to samples with no sepiolite in the composition. Since hydraulic compaction is alike for every sample, for 1% CIMSIL samples, water to cement ratio stays at the same level and simultaneously present more reinforcing elements within the matrix. However, samples with 2% of CIMSIL sepiolite retain more water after drainage which leads to a higher w/c ratio and therefore to lower composite properties. This greater water retention is also reproduced by PANGEL samples, with both 1 and 2% replacement, which promotes lower performance composites.

Regarding the flocculation of the samples (Figure 45), samples with 2% of PANGEL sepiolite present a superior chord size than 1% PANGEL samples. Bigger flocs are related to better connected fibre nets so samples with larger flocs also offer better properties related to the binder rigidity. This factor explains the superior flexural performance of samples with 2% of PANGEL despite of having

a higher w/c ratio than 1% PANGEL samples. Besides, the larger floc size may be linked to the greater bending capacity of the 1% CIMSIL samples compared to the MgO-SiO₂ samples with no sepiolite added.

Figure 47- Stress-deflection curves of the most representative sample of each composite composition. 0% stands for MgO-SiO₂ samples with no sepiolite replacement. PC stands for PC cement samples used as a control samples. The rest of the samples indicate the percentage and type of sepiolite replacement



Source: **Own creation**

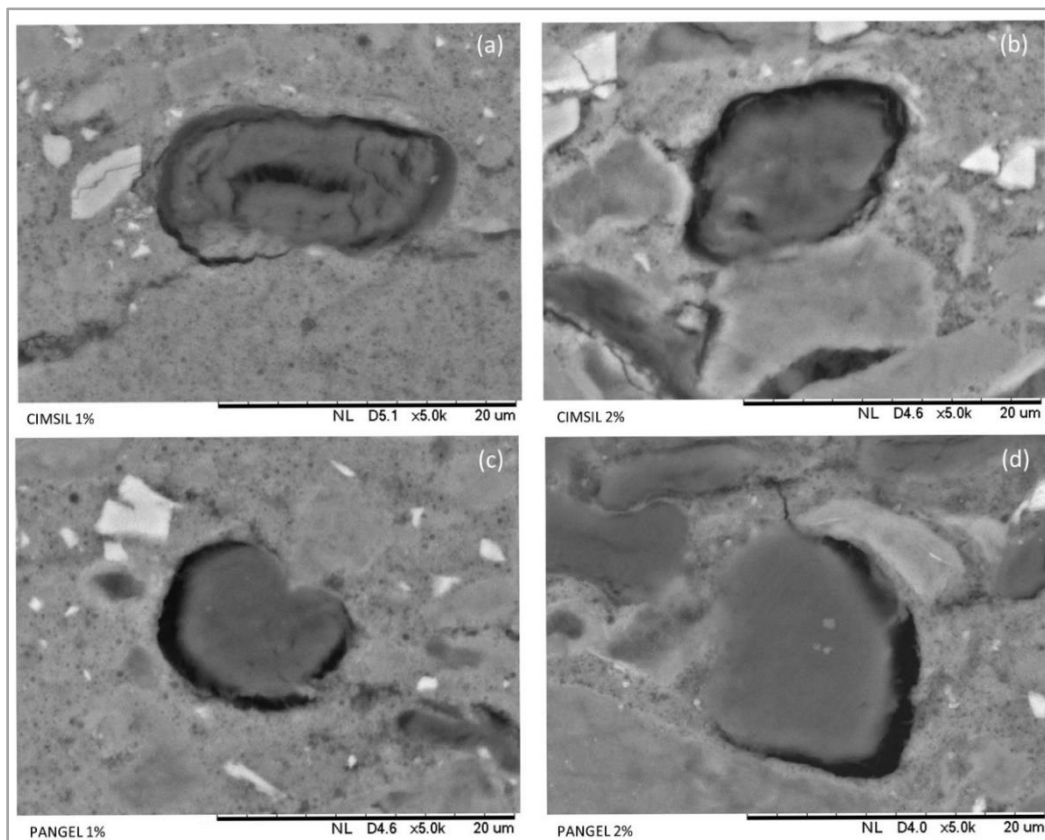
From Figure 47 and Table 25, MgO-SiO₂ samples with no addition of sepiolite (0%) have similar MOR as PC samples and also present similar characteristics related to the matrix performance (MOE and LOP). Nevertheless, properties related to the efficiency of the reinforcing elements are slightly lower for MgO-SiO₂ samples. This may be attributed to a worse fibre-matrix interface, since water retention is higher for MgO-SiO₂ samples which promotes more porous areas in the interface transition zone (ITZ). A clear example of porous ITZ is exhibited with the addition of sepiolite to the MgO-SiO₂ binding systems, excluding 1% CIMSIL samples. Samples with sepiolite show similar trend to PC and 0% samples at the initial stages of the flexural test. In the beginning, when stresses are mainly resisted by the matrix, all samples behave in an identical manner, yet when loads exceed LOP and are transferred to the fibres, samples with sepiolite reach earlier their MOR and are quickly deflected at lower flexural stresses. Considering that the main difference between the samples is the retained water, this lack of toughness shown by sepiolite formulated samples in

the plastic zone of the curve may be attributed to an extra porosity in the ITZ that disturbs the proper transmission of loads from matrix to fibres.

4.4.2.4 Composite images

In Figure 48, where fibres are centered in the middle of SEM images taken from every sample with sepiolite replacement, it is observed how the reinforcing fibre in 1% CIMSIL samples (a) presents failures, even exposing the lumen, in contrast to what happens with the rest of the samples (b, c and d), that show an intact fibre. The rest of the samples also show higher emptiness between matrix and fibre, as a consequence of the larger porosity of these samples. Imperfections in the fibre observed in 1% CIMSIL sample (a) comes from necking episodes in the fibre after larger deflections. For this reason, effects on the fibre related to necking events generate higher SE performance of the composite, since the fibre requires more energy to be pulled out from the matrix.

Figure 48- SEM images of the surroundings of reinforcing fibres for each composition with sepiolite: (a) CIMSIL 1%, (b) CIMSIL 2%, (c) PANGEL 1% and (d) PANGEL 2%



Source: **Own creation**

4.4.2.5 Physical tests

Physical tests performed on samples after flexural tests (Table 26), results confirm the trends observed with mechanical results, indicating that PC samples are denser and less porous due to the lower water retention values compared to MgO-SiO₂ samples. Greater porosity is observed in samples with lower mechanical performance, which is consistent with a more porous ITZ.

Table 26- Physical characterization of the composites for every formulation after 5 days curing at 55°C. 0% stands for MgO-SiO₂ samples with no sepiolite replacement. PC stands for PC cement samples used as a control samples. The rest of the samples indicate the percentage and type of sepiolite replacement

Sample		Bulk density (g/cm ³)	Water absorption (%)	Permeable void volume (%)
PC	Mean (std dev)	1.43 (0.03)	27.26 (1.58)	39.07 (1.46)
	Var coef (%)	2.02	5.79	3.74
0%	Mean (std dev)	1.42 (0.06)	29.61 (3.03)	41.82 (2.55)
	Var coef (%)	4.00	10.25	6.10
1% CIMSIL	Mean (std dev)	1.42 (0.44)	29.37 (1.92)	41.50 (1.50)
	Var coef (%)	2.86	6.53	3.62
2% CIMSIL	Mean (std dev)	1.38 (0.04)	30.91 (1.86)	42.66 (1.52)
	Var coef (%)	2.59	6.03	3.57
1% PANGEL	Mean (std dev)	1.37 (0.05)	31.32 (2.67)	42.90 (2.12)
	Var coef (%)	3.59	8.51	4.93
2% PANGEL	Mean (std dev)	1.38 (0.04)	31.52 (2.02)	43.29 (1.54)
	Var coef (%)	3.05	6.41	3.55

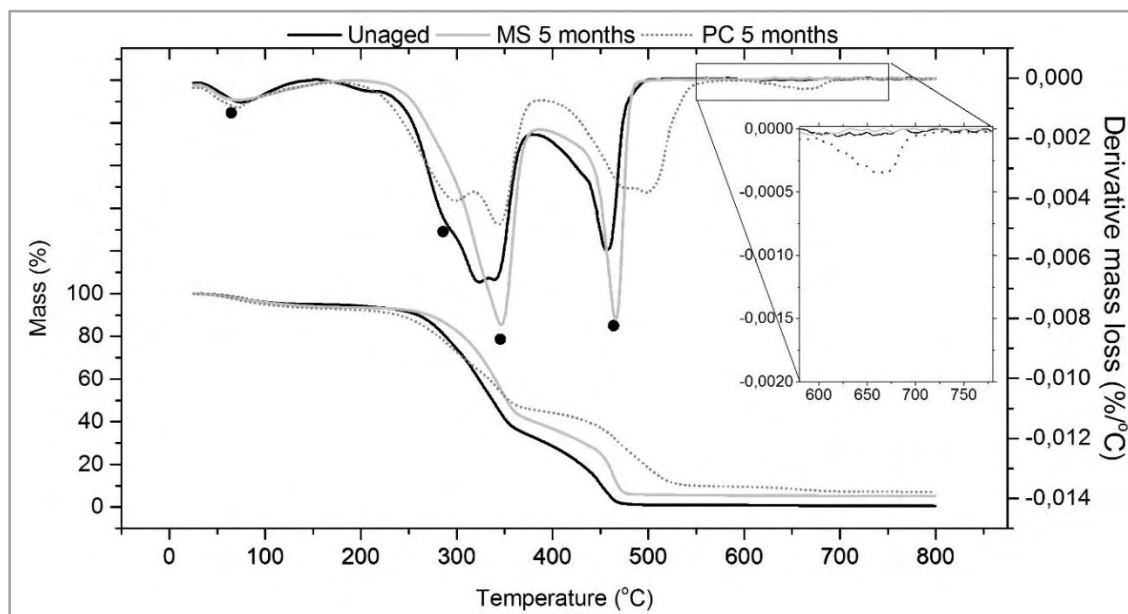
Source: **Own creation**

4.5 BLOCK 5

4.5.1 TG and DTG analysis

In order to study natural fibres degradation, the same way it is commonly performed when applied in polymer composites during the processing at elevated temperatures, the thermal behaviour of cellulosic fibres is conventionally assessed. Thus, TGA was carried out to analyse the thermal decomposition of sisal fibres after different ageing conditions. In Figure 49, TG and DTG curves of sisal are displayed and it is possible to observe different decomposition behaviours according to the different ageing situations.

Figure 49- TG/DTG thermograms of sisal fibres both unaged and aged, both in MgO-SiO₂ (MS) and Portland cement (PC), for 5 months. Circles match the different peaks obtained in DTG curves



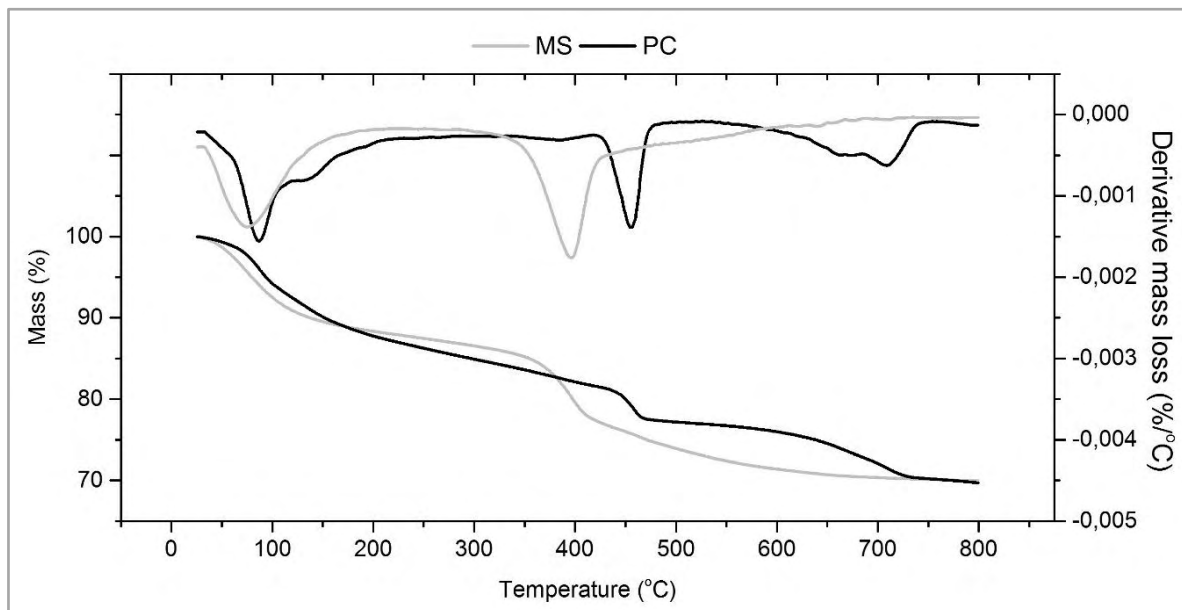
Source: Own creation

Raw sisal fibres DTG curve reveals two major peaks and a minor one at around 75°C, resulting from the loss of absorbed water in the fibre (intra and intermolecular dehydration reactions) (FAIRBRIDGE; ROSS; SOOD, 1978). From the major peaks, the first one is attributed to hemicellulose and cellulose degradation (between 200 to 400°C). The second peak is related to the decomposition of the char (between 425 and 530°C) produced during the pyrolysis of the previous components in an oxidative environment (FAIRBRIDGE; ROSS; SOOD, 1978; MARTIN et al., 2010). Sisal fibre degradation approximately started at around 195°C and took place rapidly with the temperature increase until 385°C. In the range of 320-345°C a maximum value of the DTG is observed (Figure 49), attributable to the decomposition of cellulose (Figure 52). In addition, during this degradation process, DTG curve displays a shoulder at around 295°C due to the hemicellulose degradation. This shoulder suggests that two different thermal decomposition steps are overlapped. Regarding lignin degradation, it is not possible to infer any conclusion since lignin content in sisal fibres is reduced compared with holocellulose content and this process of degradation takes place evenly from 180 to 344°C. Also lignin DTG maximum peak is produced at 205°C according to

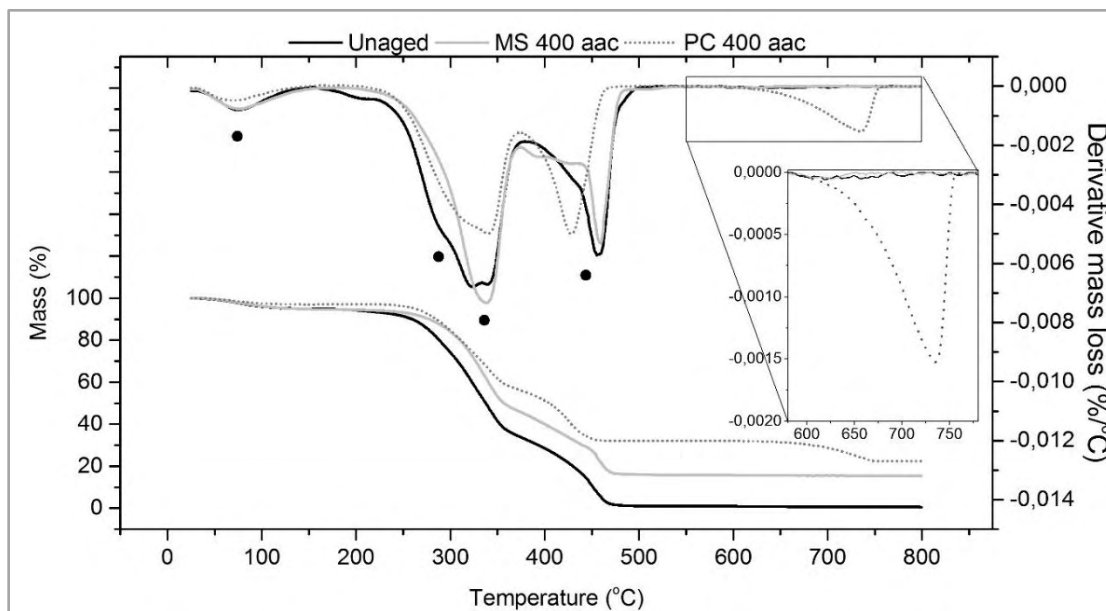
(BENÍTEZ-GUERRERO et al., 2014), which is overlapped in between the maximum of both hemicellulose (286.8°C) and cellulose (325.4°C) as seen in Figure 52.

Exposing sisal fibre to MgO-SiO₂ cement for 5 months changes the thermal decomposition of the fibres. The intensity of the DTG maximum peak is increased, which is related to cellulose fraction increase. Along with that, the shoulder at about 295°C vanishes. This behaviour is similar to sisal fibres when are treated with NaOH solution (ZHOU; CHENG; JIANG, 2014). In this alkali environment, pectin and hemicellulose are reduced.

However, in fibres submitted to PC environment all the peaks decrease their intensity and shoulder remains. This reduction in the hemicellulose and cellulose decomposition is associated to their content reduction, as consequence of alkaline hydrolysis of amorphous holocellulose and lignin (WEI; MEYER, 2014). Also, considering Figure 50, where both PC and MgO-SiO₂ samples are analysed by thermogravimetry, PC samples after 5 months show a peak between 520-760°C, which matches the DTG peak shown by fibres after 5 months in PC curve around that temperature. This peak in Portland cement, at 520-760°C, is due to the CO₂ released during calcium carbonate decomposition (DWECK et al., 2000). However, CaCO₃ is not a direct product from cement hydration reactions and comes instead from the reaction between Ca(OH)₂ and environmental CO₂ (ARANDIGOYEN; ÁLVAREZ, 2006). Moreover, since CaCO₃ has less solubility than Ca(OH)₂, the presence of CaCO₃ in the fibres is explained by the mineralization in the lumen of the fibre from the Ca²⁺ ions absorbed by the fibres in an aqueous suspension. The mineralization of the fibres is even more developed after 400 accelerating ageing cycles exposure, since fibres exposed in PC present a bigger CaCO₃ peak. This process in sisal fibres in PC environments is avoided by using MgO-SiO₂ instead, where no traces of hardened pasted is registered in the fibres.

Figure 50- TG/DTG thermograms of MgO-SiO₂ (MS) and Portland cement (PC) after 5 months

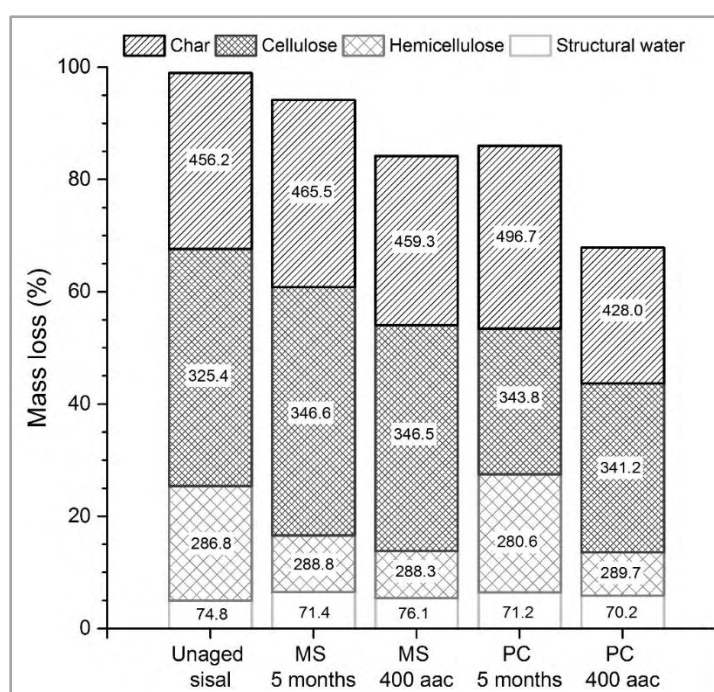
Source: Own creation

Figure 51- TG/DTG thermograms of sisal fibres both unaged and after 400 accelerated ageing cycles in, both MgO-SiO₂ (MS) and Portland cement (PC). Circles match the different peaks obtained in DTG curves

Source: Own creation

In Figure 51 and Figure 52 it is displayed a higher mass loss reduction of the lignocellulosic components after 400 accelerated ageing cycles compared to samples after 5 months exposure for both treatments. Exposing fibres to MgO-SiO₂ environment reduces hemicellulose content while cellulose remains at higher concentration than unaged sisal fibres. However, PC exposure initially (5 months ageing) affects amorphous cellulose and after 400 accelerated ageing cycles both hemicellulose and cellulose are further reduced.

Figure 52- Mass loss of each component of sisal fibres both unaged and after ageing (5 months and 400 accelerated ageing cycles) in MgO-SiO₂ (MS) and Portland cement (PC). Circles match the different peaks obtained in DTG curves

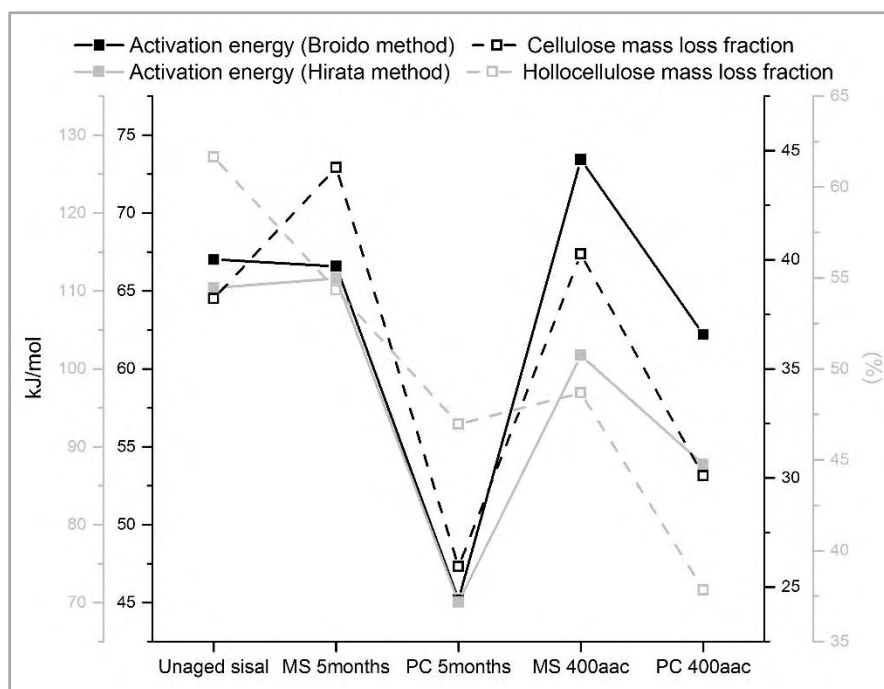


Source: Own creation

According to activation energy (Figure 53) results obtained from thermogravimetric analysis, it is possible to observe a relationship between fibre composition and the energy required to decompose the fibre. Even though holocellulose is considered a two-step decomposition process, hemicellulose first and then cellulose, activation energy is strongly influenced by the cellulose content rather than by the holocellulose. Figure 53 displays how the higher cellulose content samples present the higher activation energy for aged samples. Thus, samples aged in MgO-SiO₂

cement keep high activation energy even after 400aac since cellulose content is increased and most of the amorphous components are removed. Contrary to this, when fibres are exposed to PC, they present the lower activation energy. However, this difference in activation energy is not enough to explain the decay of the mechanical performance of the fibres after ageing previously reported when cellulosic pulps were applied in fibre-cement composites in Block 2 or (MÁRMOL; SAVASTANO, 2017).

Figure 53- Quadruple axis diagram with activation energy results according to the different methods used in thermograms (left axis) and mass loss fraction of cellulose and holocellulose (right axis)



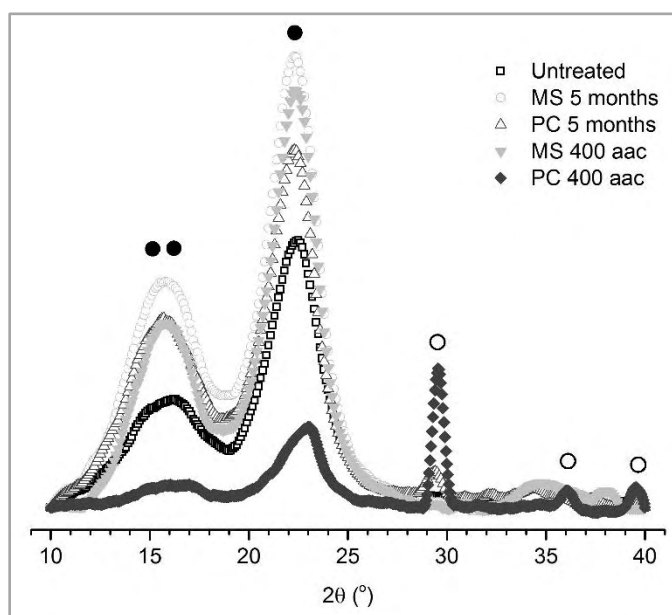
Source: Own creation

4.5.2 XRD analysis

X-ray spectrograms in Figure 54 display the effect of the different cement environment exposure on the sisal fibres crystallography. XRD patterns of untreated and aged fibres after 5 months and 400 accelerated ageing cycles for both Portland and MgO-SiO₂ cement are shown. In every sample, three bumps are marked with full black circles at around 14.8, 16.4 and 22.6 °, matching the (110), (1-10) and (200) diffraction planes of cellulose I_β polymorphism respectively (BARRETO et al., 2011). Contrary to what happens in crystalline cellulose samples, as hemp fibres

(OUAJAI; SHANKS, 2005), sisal fibres spectra show one broad peak that unifies the two diffraction peaks around 14.8° and 16.4° . The spectra are alike for most of the samples but the samples covered with Portland cement for 400 accelerated ageing cycles. The rest of the samples embedded in cement show higher peaks. This increase in intensity proves that amorphous phases of the fibres were removed and cellulose remains in higher concentration. Only fibres in Portland cement after accelerated ageing present a reduced cellulose concentration. Also higher holocellulose degradation is registered by thermogravimetric techniques.

Figure 54- X-ray diffraction patterns of untreated and aged sisal fibres, after 5 months and 400 accelerated ageing cycles, in both MgO-SiO₂ (MS) and Portland cement (PC)



Source: Own creation

Regarding cellulose crystallinity (**iError! No se encuentra el origen de la referencia.**), it was increased for every sample surrendered by alkaline matrices. When sisal fibres are exposed to alkaline atmospheres, crystalline cellulose fraction increases since amorphous cellulose is also eliminated (FERNANDES; MANO; REIS, 2013). Even after 400 accelerated ageing cycles in Portland cement, crystallinity is higher than unaged fibres, which suggests that cellulose crystallinity after ageing is preserved. However in PC samples, after 400 cycles, cellulose crystallinity is lower than samples after 5 months of ageing, indicating a decay of crystallinity over time. This increase in

cellulose crystallinity for samples aged in MgO-SiO₂ cement is considered to be beneficial for sisal fibres, since it ensures high strength and durability of fibres in cementitious materials (WEI; MEYER, 2014).

	Crystallinity Index, I _c		Crystallite size parameters		
	Peak height (%)	Amorphous subtraction (%)	2q (°)	FWHM (°)	τ (Å)
Untreated	80,63	52,54	22,40	2,69	33,43
Sisal MS 5	82,69	57,41	22,35	2,59	34,72
Sisal PC 5	82,25	62,07	22,28	2,47	36,40
Sisal MS400	84,37	61,25	22,41	2,47	36,41
Sisal PC 400	81,81	58,26	22,48	2,45	36,71

Source: **Own creation**

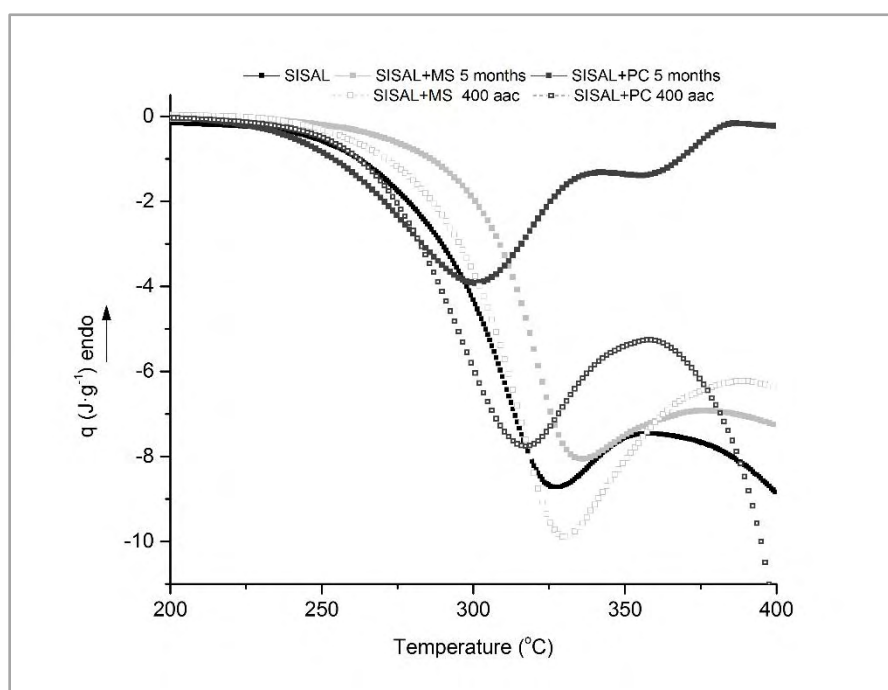
According to Figure 54, every sample increases crystallite size values. This is in contrast to what is reported to happen when cellulosic fibres are submitted to high alkaline solutions, where crystallite size is reduced (LING et al., 2017). Although crystallite size increase is not elevated, it is enough to assure that no decrease takes place. One of the mechanisms of degradation of sisal fibres proposed when used in cementitious materials is the alkaline hydrolysis (MELO FILHO; SILVA; TOLEDO FILHO, 2013), which yields breakdown of cellulose chains, so a reduction of crystallite size occurs. Based on TG and DTG results, when sisal fibres are aged in Portland cement, there is a reduction of cellulose content in the samples that is related to cellulose hydrolysis (BALLESTEROS et al., 2017). However, this reduction in cellulose fraction is not related to a reduction of the crystallite size, showing that crystallinity of cellulose is not affected after ageing. On the other hand, this increment in crystallite size may be explained by the swelling reaction between alkalis and cellulose fibres, during which a relaxation of the cellulose crystalline structure occurs. Another reason for this crystallite size increment is the immobilization of alkalis due to their mineralization and deposition on the fibre surface after reacting with the rest of fibre components such as hemicellulose and lignin.

According to different authors (MELO FILHO; SILVA; TOLEDO FILHO, 2013; MOHR; BIERNACKI; KURTIS, 2006), another factor for cellulose degradation that is also confirmed by XRD is the crystallization of lime in the fibres. For samples embedded in Portland cement, a different peak is noticeable on the diffractogram after 5 months of ageing and plainly recognizable after 400

accelerated ageing cycles at around 29.5° , as well as minor peaks 36.1 and 39.6° . These peaks present only in sisal fibres when aged in Portland cement match calcite diffractogram (CaCO_3) formed by the carbonation of $\text{Ca}(\text{OH})_2$. In addition, another calcite peak is overlapped with (2 0 0) cellulose diffraction plane at around (29.5). CaCO_3 sharpens this peak and, therefore, reduces its FWHM, so crystallite size is increased even after accelerated ageing. However, samples aged in MgO-SiO_2 cement do not present any extra peaks from those original present in unaged sisal fibres. Consequently, mineralization process is avoided by using this new type of cement.

4.5.3 DSC analysis

Figure 55- DSC curves of sisal fibres both unaged and after 5 months ageing and 400 accelerated ageing cycles in both MgO-SiO_2 (MS) and Portland cement (PC)



Source: **Own creation**

Figure 55 displays DSC trends of sisal as received and aged in both MgO-SiO_2 and PC. Temperature scale is set in the $200\text{-}400^\circ\text{C}$ range since previous to 200°C only dehydration process takes place from moisture, according to (CHAND et al., 1987), and energy involved is also related to cement decomposition process. For every sample, there is a well-defined exothermic peak from

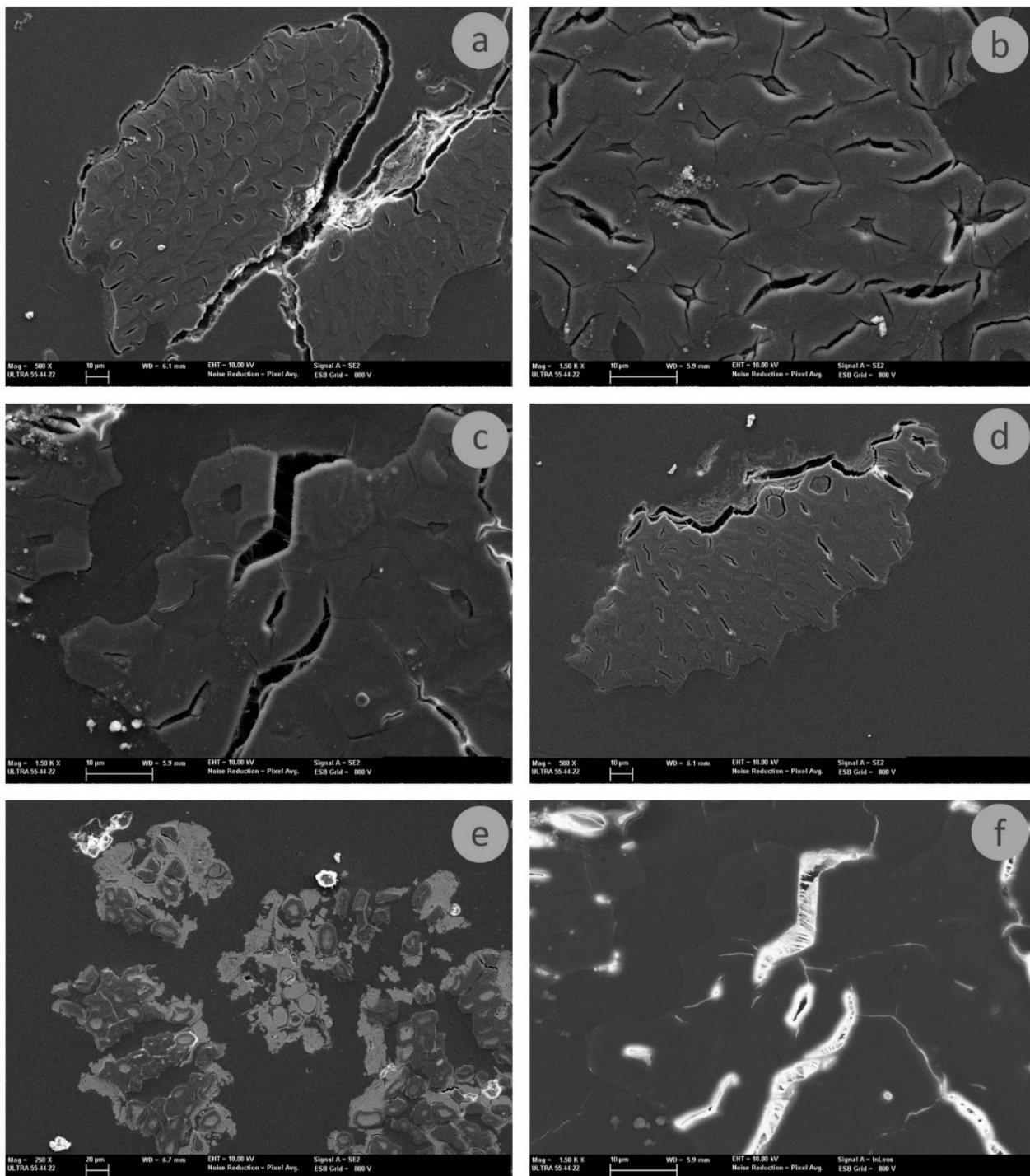
cellulose degradation process. Dehydration of holocellulose molecules at lower temperatures (CHAND et al., 1987) is followed by splitting of hydroxyl groups in oxidative atmosphere (SHAFIZADEH; BRADBURY, 1979). From 400°C onwards, char from oxidation is produced. Unaged sisal peak is centred at around 327°C (Figure 55). When ageing in MgO-SiO₂ is applied, exothermic peak is slightly increased to higher temperatures, to 330 and 335°C after 400 aac and 5 months respectively (Figure 55). Since hemicellulose and lignin degradation starts before cellulose (YANG et al., 2007; ZHOU; CHENG; JIANG, 2014), increasing temperatures of the peak centre indicates a higher cellulose content.

When sisal fibres are aged in PC for 5 months, energy intensity as well as peak centre temperature are decreased. This indicates that the lower the cellulose content, the lower the enthalpy energy. However, after accelerated ageing (400 cycles), both peak intensity and temperature at the centre are increased (Figure 55). Thus, cellulose fraction is recovered since amorphous materials are removed and crystallinity is preserved, as previously stated from TG, DTG and DRX results.

4.5.4 SEM and EDS analysis

Samples exposed to MgO-SiO₂ for 5 months, shown in Figure 56a, present a well preserved structure compared to unaged sisal fibres (Figure 56d). Neither cell walls nor lamella are damaged in contrast to fibres embedded in PC for 5 months (Figure 56b), where cracks start from the lumen and are spread outwards through the cell walls. This breakage of cell tissues (cellulose mainly) after 5 months in PC is in accordance to TG results where a decrease of cellulose is reported and it is clearly related to lower activation energy. Besides, samples in PC at this same age (Figure 56c and f) reveal that lignin and hemicellulose microfibrils suffer a breakage so a debonding process between microfibrils is initiated.

Figure 56- SEM images of sisal fibres embedded in epoxy resin after ageing. (a) 5 months in MgO-SiO₂ aged fibre backscattered secondary electrons (BSE) SEM, (b) 5 months in PC aged fibre BSE SEM, (c) enlarged view of sisal fibre in the same conditions as (b), (d) unaged fibre BSE SEM, (e) 400 aac in PC aged fibre BSE SEM and (f) SEM image from (c)

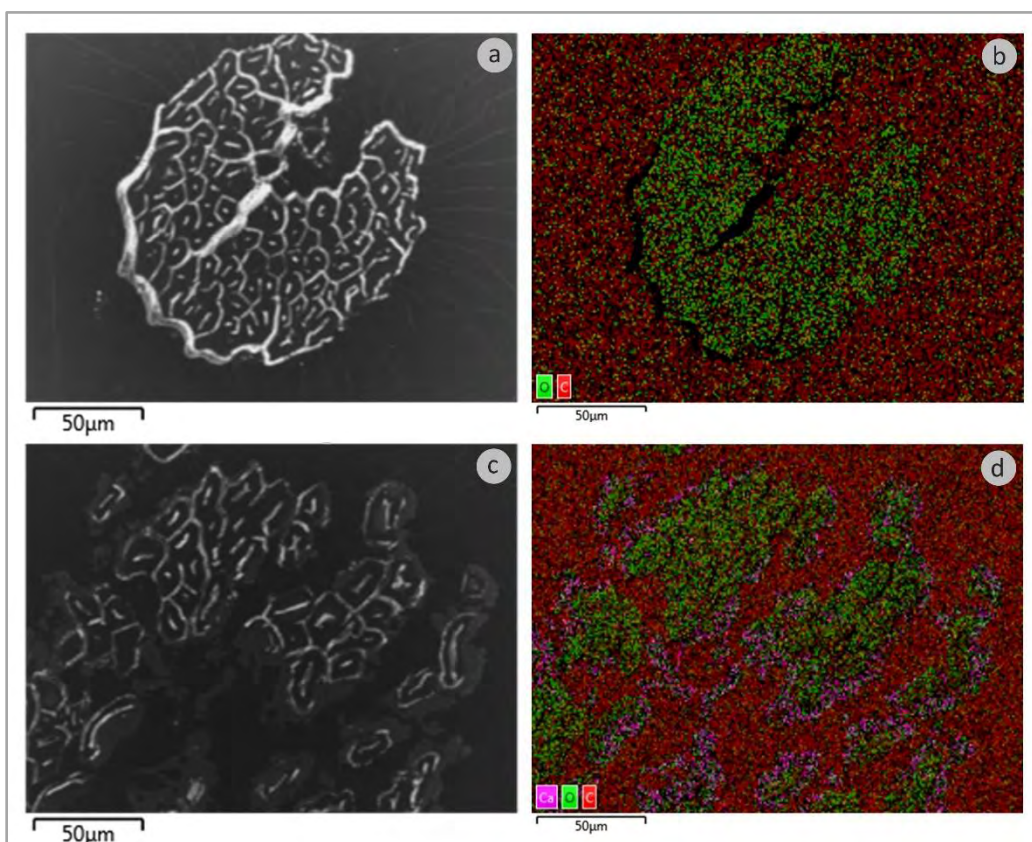


Source: Own creation

Although in PC after 5 months of ageing fibres preserve their integrity and no deposits of hydrated phases of cement are present on the surface (Figure 56a and b), after 400 ageing cycles fibres are disaggregated (Figure 56e). This disaggregation goes along with by the precipitation of compounds from the cement matrix between the microfibrils (Figure 57c). By EDS mapping (Figure 57d) it is inferred that those compounds are Ca rich so this precipitation, matches perfectly with the XRD results, where CaCO_3 is identified. EDS results also reveal another important detail since Ca rich zones match C poor zones which can be related with the presence of other compounds with no C. These compounds, also reported by other authors as portlandite [$\text{Ca}(\text{OH})_2$], undergo a carbonation process to form CaCO_3 . Fibre fragilization is attributed to these Ca compounds, so mechanical performance thereof is severely decrease. The embrittlement of the fibres due to the presence of Ca-based combinations is responsible for the lack of long term reinforcing capacity of sisal fibres in cementitious components.

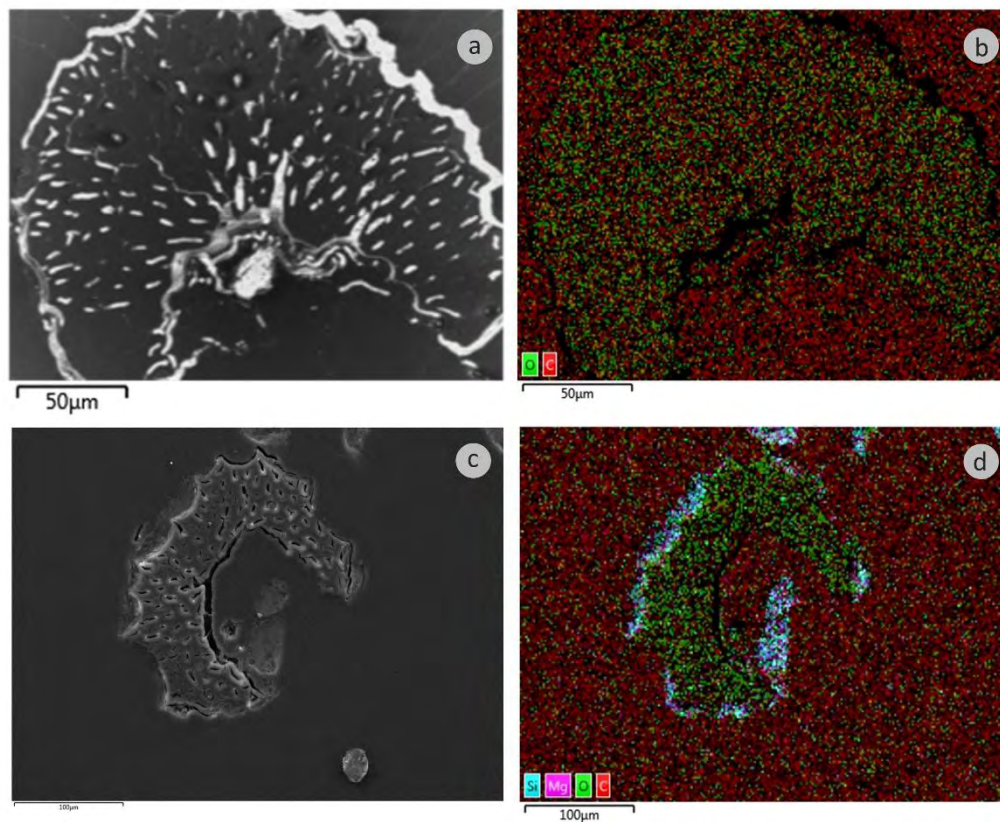
In the case of samples aged for 400 accelerated ageing cycles in MgO-SiO_2 cement (Figure 58c and d) no sign of disaggregation is observed and no compounds are precipitated between the microfibrils, which may be related to a preservation of the mechanical properties of the fibres and, therefore, a maintenance of their reinforcing capacity. Despite no presenting any traces of hydrated phases bonded to surface at 5 months (Figure 58a and b), in samples after 400 aac by EDS mapping it is displayed the presence of Mg particles bonded to the surface of the fibres. This may be explained by the evolution of the hydration reaction of the cement over time, that generates more hydrated compounds after 400aac (MÁRMOL et al., 2016). However, it is important to notice that these compounds are also rich in Si, which suggest the presence of M-S-H gel particles surrounding the fibres. This is of relevance, since it proves a good adherence between M-S-H gel, that are the main responsible for the good mechanical performance of MgO-SiO_2 cement, and lignocellulosic fibres, with no signs of degradation even after 400 accelerated ageing.

Figure 57- SEM images and EDS mapping of sisal fibres embedded in epoxy resin at different ageing times exposed to PC. (a) SEM of samples after 5 months in PC, (b) EDS mapping of samples after 5 months in PC, (c) SEM of samples after 400 accelerated ageing cycles in PC and (d) EDS mapping of samples after 400 accelerated ageing cycles in PC



Source: Own creation

Figure 58- SEM images and EDS mapping of sisal fibres embedded in epoxy resin at different ageing times exposed to MgO-SiO₂ cement. (a) SEM of samples after 5 months in MgO-SiO₂ cement, (b) EDS mapping of samples after 5 months in MgO-SiO₂ cement, (c) SEM of samples after 400 accelerated ageing cycles in MgO-SiO₂ cement and (d) EDS mapping of samples after 400 accelerated ageing cycles in MgO-SiO₂ cement



Source: Own creation

5 CONCLUSIONS

5.1 General Conclusions

As intended initially, production of FRCC with MgO based cement and lignocellulosic fibres was successfully achieved. Clinker-free cement, made out of a blend of MgO (60% w.t.) and SiO₂ (40% w.t.) powder was used as hydraulic binder matrix for FRCC. This cement presents higher compressive strength compared to Portland cement for a 0.5 water to binder ratio after 28 days of curing under saturated environment conditions. It also has lower pH values from the first hydration stages (pH=11.09 after mixing in water) and it decreases over time (pH=9.91 after 28 days). Thin sheets of FRCC with the new cement were bending tested and good mechanical properties were achieved and well preserved after ageing. Contrary to what happens in samples made out of Portland cement, with MgO based cement samples, no degradation mechanisms are noticed after ageing. Specific energy does not decrease and bending strength is improved along with time due to the ongoing hydration of the MgO-SiO₂-H₂O systems. Also carbonation curing has been proved to improve FRCC stability. New Hydrate Magnesium Carbonated phase is obtained, which yields to more rigid materials due to the higher volume of hydrates in the matrix. Partial cement replacement by sepiolite improves flocculation stability of the fibre-cement suspensions, particles retention and FRCC homogeneity since the variation coefficient of the mechanical parameters and physical properties is reduced for samples with sepiolite. Sisal fibres were embedded in MgO-based cement and submitted to longer accelerated ageing curing and no signs of damage were perceived on the fibres. While sisal fibres in Portland show symptoms of degradation (cracking of the cells, breakage of the linking cell tissues and CaCO₃ depositions), fibres in MgO-SiO₂ cement preserve their integrity and both their cellulose content and crystallinity.

5.2 BLOCK 1

In systems where MgO and SiO₂ are mixed with water, the hydration products obtained are Mg(OH)₂ and M-S-H gels for all the formulations studied regardless of age (7 and 28 days). From TG tests on samples 100% Mg(OH)₂ and M-S-H gels is possible to determine the amount of Mg(OH)₂ in the blended samples, whereas the mass loss produced between 300 and 550°C in blended samples is due to the dehydroxylation of Mg(OH)₂. So it is noted that for formulations with higher MgO content higher content of Mg(OH)₂ is obtained as hydration product.

EDS results indicate that the M-S-H gels obtained both at 7 and 28 days have a Mg/Si ratio gain with increasing MgO content. Similarly, for all samples the Mg/Si ratio increases over time, which can be interpreted as a change in the gel structure over time because the reaction is still not complete after 28 days. This can also be detected by SEM studies, where particles of $\text{Mg}(\text{OH})_2$ are surrounded by areas of high concentration of Si, which is interpreted as a region where there has been a great dissolution of SiO_2 to form $[\text{Si}(\text{OH})_4]$. This in turn facilitates the dissociation Mg^{2+} and $(\text{OH})^-$, promoting the formation of laminar structures of silicates which subsequently form part of the structure of the MSH gels. Also FTIR spectra obtained for all samples exhibit a strong resemblance to the spectra corresponding to the layered hydroxides which are similar to chain and laminar silicates, as well as the basic units forming the structures of layered double hydroxide minerals.

Despite initially pursuing the maximum content of M-S-H gels in samples in order to achieve the maximum mechanical performance, it is observed that this does not necessarily increase mechanical performance of the samples. Conversely, at 7 days there is a correlation between the content of $\text{Mg}(\text{OH})_2$ and the compressive strength of the samples, indicating that the mechanical properties are not influenced exclusively by the M-S-H gel content. This is corroborated even at 28 days wherein the formulation with highest mechanical strength is not the one with a highest M-S-H gel content. There seems to be a clear correlation between the amount of pores associated with the free presence in the matrix after the hydration reactions, and the compressive strength.

In view of the results of pH tests, samples with less MgO content have lower values. According to compression tests, the formulations 60% MgO-40% SiO_2 and 70% MgO-30% SiO_2 have the highest values at 28 days, with no statistical difference. 60% MgO-40% SiO_2 is chosen as optimal for the development of fibre-cement composites since is the most mechanical resistant and is less alkaline compared with 70% MgO-30% SiO_2 .

5.3 BLOCK 2

The use of Magnesia-Silica (MgO-SiO_2) cement is presented as an excellent solution to produce fibre-cement products reinforcement exclusively with lignocellulosic fibres since this new type of binder preserves cellulosic fibres integrity after ageing, so composites made out of MgO-

SiO₂ exhibit significant higher properties after 200 cycles of accelerated ageing than Portland cement composites. According to flexural tests MgO-SiO₂ fibre-cement composites:

Increase or maintain Modulus of Rupture, Limit of Proportionality and Modulus of Elasticity values after 200 cycles of accelerated ageing for both types of reinforcement (pine and eucalyptus fibres), contrarily to what happens for Portland cement samples that suffer a significant loss on Modulus of Rupture after ageing.

Present the highest values of Specific Energy and Specific Deflection for both types of reinforcement at the two tested ages. The preservation of the Specific Energy after 200 aac of the MgO-SiO₂ samples reinforced with eucalyptus pulp is remarkable, while PC samples drastically lose their initial toughness.

Offer better properties when reinforced with eucalyptus fibres rather than samples with pine fibres. This can be associated to the reduced water retention of the eucalyptus pulps during molding process, allowing lower water to binder ratio and thus a less porous matrix. Another factor to explain the best mechanical performance of the samples reinforced with eucalyptus is their shorter length and width, thus obtaining a higher number of reinforcing elements by mass. Hence, a more homogeneous distribution of the reinforcement is achieved.

In addition, with the aid of the SEM images, the preservation of the cellulosic fibres is confirmed and flexural performance is explained when reinforcing MgO-SiO₂ matrices, observing that:

No significant evidences of mineralization are observed, as occurs with PC samples that suffer lumen mineralization (eucalyptus fibres) and fibre-matrix interface mineralization (pine fibres), suggesting that no apparent damage is caused to the fibres.

A better fibre-matrix adherence is produced due to a matrix densification result of an ongoing hydration reaction. This evolution of the hydration reaction also helps to improve the composite rigidity and physical properties since a significant reduction of the water absorption and apparent porosity is achieved after accelerated ageing.

Better distribution of eucalyptus fibres in comparison to pine fibres, reducing the unreinforced regions within the matrix and therefore resulting in a better mechanical performance.

In view of all the experimental results, the use of MgO-SiO₂ is presented as a suitable alternative to cementitious products reinforced with cellulosic pulps with potential application in civil construction in view of acceptable performance under binding solicitations and since no appreciable degradation of the fibres takes place after 200 soak & dry accelerated ageing cycles.

5.4 BLOCK 3

According to XRD results, for uncarbonated samples, Mg(OH)₂ and M-S-H gels are present in the samples before and after ageing, remaining as the main hydration products. However, for carbonated samples, Mg(OH)₂ peaks are clearly lowered, arising new peaks matching hydromagnesite [Mg₅(CO₃)₄(OH)₂·4H₂O]. Another particular feature for carbonated samples is the reduction of the humps corresponding to M-S-H gel, suggesting that this phase is also carbonated. These effects of carbonation may be extended even after carbonation curing conditions are present, when samples are submitted to high temperatures (60°C).

From TG curves, it is possible to observe the effectiveness of carbonation curing since samples submitted to carbonation present a higher mass loss due to the decomposition of carbonated products. From DTG curves, two specific peaks centred at around 260 and 520°C are present for carbonated samples, matching the dehydroxylation and decarbonation of hydromagnesite, main product obtained from carbonation curing process. These two peaks remain for carbonated samples after accelerated ageing cycles, confirming the thermodynamic stability of the carbonated phases over time. Another effect of carbonation is the dislocation of the peaks that are centred at around 110 and 410°C when non-carbonation curing is applied. Thus, this displacement may be attributed to carbonation of brucite and M-S-H respectively.

Furthermore, SEM confirms the presence of hydromagnesite crystals when carbonation curing is applied as well as different crystalline phases not noticed for uncarbonated samples that can be associated to the carbonation of the M-S-H gel in the paste. This process of carbonation may produce modify the chemical composition of MgO-SiO₂-H₂O systems to form compounds with a sepilolite-like composition.

Regarding flexural performance, excellent strength is achieved, with values over 12 MPa, confirming the suitability of both cement and polypropylene fibres to produce apt fibre-cement

products. Besides, extraordinary toughness performance is attained, with specific energy values over 7.5 kJ/m^2 . Carbonation affects positively to mechanical strength and physical properties with no deleterious effects after ageing since it increases matrix rigidity. These flexural values are higher than those reported on the literature where polypropylene fibres are unable to offer a good reinforcement effect due to its low density that generates a poor distribution within the matrix and the possible formation of clumps. An increment in the amount of cellulosic reinforcement would help to resist higher flexural loads without decreasing the toughness of the composites.

5.5 BLOCK 4

Sepiolite addition increases MOE of hydrated MgO-SiO_2 pastes regardless sepiolite type and replacement amount. The lower the sepiolite replacement the higher elastic modulus. Since most of the formulations do not affect the $\text{MgO-SiO}_2\text{-H}_2\text{O}$ system reactivity, this improvement in MOE is related to a better interlinking between hydrated particles created by sepiolite particles. When sepiolite addition improves the formation of more M-S-H gel, it is also associated to a higher specific surface of this type of sepiolite (PANGEL). This also affect to the water retention of the samples and therefore it can be concluded that the presence of more hydrated compounds is a consequence of a higher amount of water within the system.

Regarding flocculation, the addition of sepiolite to MgO-SiO_2 systems increases the floc size of the fibre-cement suspensions in an aqueous liquid compared to PC samples. This improves the DPM process in terms of fines retention. The higher fines retention would be a very positive effect in an upscaled production process due to the reduced amount of tiny particles susceptible of being stack and block industrial machinery.

The introduction of sepiolite in suspensions where both cement and fibres are dispersed hampers water removal in MgO-SiO_2 systems compared to PC systems. However the addition of sepiolite increases drainage speed, this is that most of the water is removed faster than in samples containing PC. Once again, this factor would suppose an advantage in a larger production scale since it makes more efficient the DPM process with regard to energy saving in the dewatering step. Samples with higher specific surface sepiolite retain more water than those with lower specific surface. This phenomenon is also reported for hydrated pastes.

Since sepiolite induces a higher water retention with no reactive effect, it decreases flexural and physical performances of the FRCC. Nevertheless, this increase in retain water may be counterbalanced with the interlocking effect of the sepiolite particles that can improve flexural performance and physical properties when dosed in reduced amounts (1%). This is very important since it allows the combination with carbonation curing techniques since the greater amount of water in the samples enhances the carbonation process in Mg-based cements.

The most interesting effect of adding sepiolite into FRCC with MgO-SiO₂ systems is the increase of the composite homogeneity. This is specially remarkable in the case of physical properties, which is undeniably desired as it makes possible the achievement of a more reliable material. It would also be important to optimise this type of composites in the future, since the use of sepiolite would reduce the amount of material to obtain reliable test results.

5.6 BLOCK 5

Thermal tests reveal that sisal fibres, even after 400 accelerated ageing cycles do not suffer a significant reduction in cellulose content when exposed to MgO-SiO₂ cement. The mass loss reported is in accordance with alkali treatments applied for polymeric composites applications, where amorphous fractions are undesired. In addition, from thermal tests, activation energy and enthalpy is well preserved for fibres in MgO-SiO₂ regardless ageing treatment.

From XRD tests is deduced that cellulose crystallinity and crystallite size is well preserved and slightly increased due to the removal of amorphous compounds of the fibres. This is in contrast with samples embedded in PC, which after 400aac it is noticed a little decrease of crystallinity due to the chemical degradation of cellulose. Besides, samples in MgO-SiO₂ do not present extra peaks in their respective diffractograms corresponding to compounds migrated from cement hydration. This suggests that no mineralization is produced.

According to SEM techniques, it is possible to see the integrity of the whole fibre with no detachment between microfibrils neither after 5 months nor after 400aac when submitted to MgO-SiO₂ environment. In addition to the intact aspect of the cross section of the fibres, it is displayed after 400aac that compounds from cement hydration, in spite of no penetrating to the inner parts of the fibres, are perfectly bonded to the surface thereof. Besides, this cement compounds are both

Mg and Si rich, which suggests that not only $\text{Mg}(\text{OH})_2$ is formed in the surrounding of the fibres. This is an important aspect since it assures the presence of strong phases in the ITZ, which could promote a good adherence between fibre and matrix when sisal fibres are applied in this type of FRCC.

6 POSSIBLE FUTURE WORKS

This thesis is an introduction of lower-alkalinity Mg-based FRCC with lignocellulosic fibres. In view of the efficiency of this type of cement for preserving composites performance over time, it seems possible to develop a new technology for the production of cementitious materials totally reinforced with cellulose-based materials. However, this work is an initial contact with several limitations. Consequently, a sequence of further research has to be performed in order to evaluate the authentic possibilities of this new technique. Several studies are exposed to give a continuity to the present study:

- Evaluation of the dimensional stability of the exposed composites with the optimization techniques explored in previous chapters implemented separately or combined.
- Study at longer times and under different ageing conditions of the hydration evolution with complimentary techniques to the methods used in this work.
- Analysis of the Interface Transition Zone to understand properly the phenomena in this region of the composites and to assess the adherence between lignocellulosic fibres and Mg-based cement.
- Study of the structure of the M-S-H gels and evaluation of methods to improve flowability thereof to adopt different moulding procedures.
- Evaluation of different FRCC moulding techniques, assessment of their technical properties and establishment of possible alternative applications for these building materials.
- Study of the introduction of alternative pozzolans to the system as a source of amorphous SiO₂ to replace the use of silica fume by agricultural ashes. The use of pozzolans has been successfully applied and standardised in PC applications. Pozzolan use would contribute to the settlement of new industries in rural areas.
- Exploring Novacem route to produce MgO-SiO₂-H₂O systems since this cement would result in a great opportunity to reduce the cost of reinforcing elements of the current construction industry. Nowadays, Novacem technology and Intellectual Property belongs to Calix, an Australian chemical company that is currently heading the vanguard of CO₂ intake in materials. The development of this knowledge would be an opportunity to for new entrepreneurship.
- Life Cycle Assessment of this technology compared to different alternatives and the current FRCC used in the construction industry.

REFERENCES

- AKERS, S. A. S.; STUDINKA, J. B. Ageing behaviour of cellulose fibre cement composites in natural weathering and accelerated tests. **International Journal of Cement Composites and Lightweight Concrete**, Kidlington, v. 11, n. 2, p. 93–97, May. 1989.
- ALEXANDER, G. B.; HESTON, W. M.; ILER, R. K. The solubility of amorphous silica in water. **The Journal of Physical Chemistry**, Washington, v. 58, n. 6, p. 453–455, June. 1954.
- ALI, I. M.; KOTP, Y. H.; EL-NAGGAR, I. M. Thermal stability, structural modifications and ion exchange properties of magnesium silicate. **Desalination**, Amsterdam, v. 259, n. 1–3, p. 228–234, Sept. 2010.
- ALMEIDA, A. E. F. S. et al. Improved durability of vegetable fiber reinforced cement composite subject to accelerated carbonation at early age. **Cement and Concrete Composites**, Kidlington, v. 42, p. 49–58, Sept. 2013.
- ÁLVAREZ, A. et al. Current industrial applications of palygorskite and sepiolite. In: GALÁN, E.; SINGER, A. (Ed.). **Developments in clay science**. Amsterdam: Elsevier, 2011. v. 3, p. 281–298.
- ANDREJKOVICĚOVÁ, S. et al. Air lime mortars with incorporation of sepiolite and synthetic zeolite pellets. **Acta Geodynamica et Geomaterialia**, Prague, v. 9, n. 165, p. 79–81, Feb. 2012.
- ANDREJKOVICĚOVÁ, S. Fine sepiolite addition to air lime-metakaolin mortars. **Clay Minerals**, Berlin, v. 46, n. 4, p. 621–635, 1 Dec. 2011.
- ANTIOHOS, S. K.; PAPADAKIS, V. G.; TSIMAS, S. Rice husk ash (RHA) effectiveness in cement and concrete as a function of reactive silica and fineness. **Cement and Concrete Research**, Kidlington, v. 61–62, p. 20–27, July. 2014.
- ARANDIGOYEN, M.; ÁLVAREZ, J. I. Proceso de carbonatación en pastas de cal con distinta relación agua/conglomerante. **Materiales de Construcción**, Madrid, v. 56, n. 281, p. 5-18, Mar. 2006.
- ARDANUY, M.; CLARAMUNT, J.; TOLEDO FILHO, R. D. Cellulosic fiber reinforced cement-based composites: a review of recent research. **Construction and Building Materials**, Amsterdam, v. 79, p. 115–128, Mar. 2015.
- ASOKAN, P.; OSMANI, M.; PRICE, A. D. F. Assessing the recycling potential of glass fibre reinforced plastic waste in concrete and cement composites. **Journal of Cleaner Production**, Amsterdam, v. 17, n. 9, p. 821–829, June. 2009.
- AMERICAN SOCIETY FOR TESTING AND MATERIALS - ASTM. **ASTM C150/C150M - Standard Specification for Portland Cement**. West Conshohocken, PA, USA: ASTM International, 2012. .
- _____. **ASTM C1185-08 - Test Methods for Sampling and Testing Non-Asbestos Fiber-Cement Flat Sheet, Roofing and Siding Shingles, and Clapboards**. West Conshohocken, PA, USA: ASTM International, 2012.

_____. **ASTM C1548 - 02 - Standard Test Method for Dynamic Young's Modulus, Shear Modulus, and Poisson's Ratio of Refractory Materials by Impulse Excitation of Vibration**. West Conshohocken, PA, USA: ASTM International, 2007.

BAEZA, F. J. et al. Effect of aspect ratio on strain sensing capacity of carbon fiber reinforced cement composites. **Materials & Design**, London, v. 51, p. 1085–1094, Oct. 2013.

BALCI, S. Thermal decomposition of sepiolite and variations in pore structure with and without acid pre-treatment. **Journal of Chemical Technology & Biotechnology**, v. 66, n. 1, p. 72–78, May 1996.

BALLESTEROS, J. E. M. et al. Evaluation of cellulosic pulps treated by hornification as reinforcement of cementitious composites. **Construction and Building Materials**, Amsterdam, v. 100, p. 83–90, Dec. 2015.

BARCELO, L. et al. Cement and carbon emissions. **Materials and Structures**, Dordrecht, v. 47, n. 6, p. 1055–1065, June. 2014.

BARRA, B. et al. Effects of methane cold plasma in sisal fibers. **Key Engineering Materials**, Pfaffikon, v. 517, p. 458–468, June. 2012.

BARRETO, A. C. H. et al. Properties of sisal fibers treated by alkali solution and their application into cardanol-based biocomposites. **Composites Part A: Applied Science and Manufacturing**, Kidlington, v. 42, n. 5, p. 492–500, May 2011.

BEALL, G. W. et al. Rapid fabrication of nanostructured magnesium hydroxide and hydromagnesite via microwave-assisted technique. **Powder Technology**, Amsterdam, v. 234, p. 26–31, Jan. 2013.

BELGACEM, M. N.; GANDINI, A. The surface modification of cellulose fibres for use as reinforcing elements in composite materials. **Composite Interfaces**, Leiden, v. 12, n. 1–2, p. 41–75, Jan. 2005.

BENÍTEZ-GUERRERO, M. et al. Comparison of thermal behavior of natural and hot-washed sisal fibers based on their main components: cellulose, xylan and lignin. TG-FTIR analysis of volatile products. **Thermochimica Acta**, Amsterdam, v. 581, p. 70–86, Apr. 2014.

BENTUR, A.; MINDESS, S. **Fibre reinforced cementitious composites**. 2nd ed. London: Taylor & Francis, 2007.

BEZERRA, E. M. et al. The effect of different mineral additions and synthetic fiber contents on properties of cement based composites. **Cement and Concrete Composites**, Kidlington, v. 28, n. 6, p. 555–563, July. 2006.

BEZERRA, E. M.; JOAQUIM, A. P.; SAVASTANO JR, H. Some properties of fiber-cement composites with selected fibers. In: CONFERÊNCIA BRASILEIRA DE MATERIAIS E TECNOLOGIAS NÃO-CONVENCIONAIS - NOCMAT, 2004, Pirassununga. **Anais...** Pirassununga: FZEA-USP, 2004. 14 p.

BJERGA, A.; KONOPÁSEK, J.; PEDERSEN, R. B. Talc-carbonate alteration of ultramafic rocks within the leka ophiolite complex, central norway. **Lithos**, Amsterdam, v. 227, p. 21–36, June. 2015.

- BODROS, E.; BALEY, C. Study of the tensile properties of stinging nettle fibres (*Urtica Dioica*). **Materials Letters**, Amsterdam, v. 62, n. 14, p. 2143–2145, May. 2008.
- BOTHA, A.; STRYDOM, C. A. Preparation of a magnesium hydroxy carbonate from magnesium hydroxide. **Hydrometallurgy**, Amsterdam, v. 62, n. 3, p. 175–183, Dec. 2001.
- BOTHA, A.; STRYDOM, C. A. DTA and FT-IR analysis of the rehydration of basic magnesium carbonate. **Journal of Thermal Analysis and Calorimetry**, Budapest, v. 71, n. 3, p. 987–996, 2003.
- BOURMAUD, A. et al. Relationships between micro-fibrillar angle, mechanical properties and biochemical composition of flax fibers. **Industrial Crops and Products**, Amsterdam, v. 44, p. 343–351, Jan. 2013.
- BRATERMAN, P. S. Vibrational spectroscopy of brucite: a molecular simulation investigation. **American Mineralogist**, Chantilly, v. 91, n. 7, p. 1188–1196, July. 2006.
- BREW, D. R. M.; GLASSER, F. P. Synthesis and characterisation of magnesium silicate hydrate gels. **Cement and Concrete Research**, Kidlington, v. 35, n. 1, p. 85–98, Jan. 2005.
- CÉLINO, A. et al. The hygroscopic behavior of plant fibers: a review. **Frontiers in Chemistry**, Lausanne, v. 1, art. 43, 2014.
- CHAND, N. et al. Structural and thermal studies on sisal fibre. **Journal of Thermal Analysis**, Budapest, v. 32, n. 2, p. 595–599, Mar. 1987.
- CHEN, L.; YE, G. et al. Low Temperature synthesis of forsterite from hydromagnesite and fumed silica mixture. **Ceramics International**, Kidlington, v. 41, n. 2, p. 2234–2239, Mar. 2015.
- CHEN, X.; WU, S. Influence of water-to-cement ratio and curing period on pore structure of cement mortar. **Construction and Building Materials**, Amsterdam, v. 38, p. 804–812, Jan. 2013.
- CORNEJO, J.; HERMOSIN, M. C. Structural alteration of sepiolite by dry grinding. **Clay Minerals**, Berlin, v. 23, n. 4, p. 391–398, Dec. 1988.
- COUTTS, R. S. P. A review of Australian research into natural fibre cement composites. **Cement and Concrete Composites**, Kidlington, v. 27, n. 5, p. 518–526, May. 2005.
- DIAS, C. M. R.; SAVASTANO JR., H.; JOHN, V. M. Exploring the potential of functionally graded materials concept for the development of fiber cement. **Construction and Building Materials**, Amsterdam, v. 24, n. 2, p. 140–146, Feb. 2010.
- DWECK, J. et al. Hydration of a portland cement blended with calcium carbonate. **Thermochimica Acta**, Amsterdam, v. 346, n. 1–2, p. 105–113, Mar. 2000.
- EN 494:2012+A1:2015**. Fibre-cement profiled sheets and fittings. Product specification and test methods. Brussels: European Committee for Standardization, 2012. (CEN-CENELEC Management centre: Avenue Marnix 17, B-1000).
- ENCYCLOPÆDIA BRITANNICA. **Composite material**. 2013. (Nota técnica).

FAIRBRIDGE, C.; ROSS, R. A.; SOOD, S. P. A kinetic and surface study of the thermal decomposition of cellulose powder in inert and oxidizing atmospheres. **Journal of Applied Polymer Science**, Hoboken, v. 22, n. 2, p. 497–510, Feb. 1978.

FAKIROV, S.; BHATTACHARYYA, D. (Ed.). **Handbook of engineering biopolymers: homopolymers, blends, and composites**. Munich: Cincinnati, 2007.

FARUK, O. et al. Biocomposites reinforced with natural fibers: 2000–2010. **Progress in Polymer Science**, London, v. 37, n. 11, p. 1552–1596, Nov. 2012.

FEITKNECHT, W.; BRAUN, H. Der Mechanismus der Hydratation von Magnesiumoxid mit Wasserdampf. **Helvetica Chimica Acta**, Zuerich, v. 50, n. 7, p. 2040–2053, Oct. 1967.

FERNANDES, E. M.; MANO, J. F.; REIS, R. L. Hybrid Cork–polymer composites containing sisal fibre: morphology, effect of the fibre treatment on the mechanical properties and tensile failure prediction. **Composite Structures**, London, v. 105, p. 153–162, Nov. 2013.

FERNÁNDEZ, A. I. et al. Kinetic study of carbonation of MgO Slurries. **Hydrometallurgy**, Amsterdam, v. 53, n. 2, p. 155–167, Aug. 1999.

FRÍAS, M.; GOÑI, S. Accelerated carbonation effect on behaviour of ternary portland cements. **Composites Part B: Engineering**, Kidlington, v. 48, p. 122–128, May. 2013.

FRUHWIRTH, O. et al. Dissolution and hydration kinetics of MgO. **Surface Technology**, Lausanne, v. 24, n. 3, p. 301–317, Mar. 1985.

FUENTE, E. et al. Effect of Sepiolite on retention and drainage of suspensions of fiber–reinforced cement. **Construction and Building Materials**, Amsterdam, v. 24, n. 11, p. 2117–2123, Nov. 2010.

GARTNER, E. Industrially interesting approaches to “low-CO₂” cements. **Cement and Concrete Research**, Kidlington, v. 34, n. 9, p. 1489–1498, Sept. 2004.

GARTNER, E.; HIRAO, H. A Review of alternative approaches to the reduction of CO₂ emissions associated with the manufacture of the binder phase in concrete. **Cement and Concrete Research**, Kidlington, v. 78, p. 126–142, Dec. 2015.

GAUTIER, Q. et al. Hydromagnesite solubility product and growth kinetics in aqueous solution from 25 to 75°C. **Geochimica et Cosmochimica Acta**, Kidlington, v. 138, p. 1–20, Aug. 2014.

GOLDSCHMIDT, V. M. **Geochemistry**. Clarendon Press, 1954.

GOMES, C. E. M.; CAMARINI, G. Magnesium oxysulfate fibercement. **Key Engineering Materials**, Pfaffikon, v. 600, p. 308–318, Mar. 2014.

GOÑI, S. et al. Quantitative study of hydration of C₃S and C₂S by thermal analysis: evolution and composition of C–S–H gels formed. **Journal of Thermal Analysis and Calorimetry**, Budapest, v. 102, n. 3, p. 965–973, Dec. 2010.

GRAM, H. E. Durability of natural fibres in concrete. (Stockholm: Swedish Cement and Concrete Research Institute, 1983a).

- GRAM, H. E. Methods for reducing the tendency towards embrittlement in sisal fibre concrete. **Nordic Concrete Research**, Oslo, v. 2, n. 4, p. 62-71, 1983b.
- GRAM, H. E. Durability studies of natural organic fibres in concrete, mortar or cement. In: SWAMY, R. M.; WAGSTAFFE, R. L.; OAKLEY, D. R. (Ed.). **Developments in fibre reinforced cement and concrete**. Cachan Cedex: Rilem Publications, 1986.
- GUPTA, T.; CHAUDHARY, S.; SHARMA, R. K. Mechanical and durability properties of waste rubber fiber concrete with and without silica fume. **Journal of Cleaner Production**, Amsterdam, v. 112, p. 702–711, Jan. 2016.
- HAN, T. Y. et al. Influence of polyolefin fibers on the engineering properties of cement-based composites containing silica fume. **Materials & Design**, London, v. 37, p. 569–576, May. 2012.
- HANNA, R. Infrared properties of magnesium oxide. **Journal of the American Ceramic Society**, Malden, v. 48, n. 7, p. 376–380, July. 1965.
- HANSEN, L. D. et al. Carbonated serpentinite (Listwanite) at Atlin, British Columbia: a geological analogue to carbon dioxide sequestration. **The Canadian Mineralogist**, Quebec, v. 43, n. 1, p. 225–239, 1 Feb. 2005.
- HAURIE, L. et al. Effects of milling on the thermal stability of synthetic hydromagnesite. **Materials Research Bulletin**, Kidlington, v. 42, n. 6, p. 1010–1018, June. 2007.
- HE, C.; MAKOVICKY, E.; OSBÆCK, B. Thermal treatment and pozzolanic activity of sepiolite. **Applied Clay Science**, Okayama, v. 10, n. 5, p. 337–349, Jan. 1996.
- HOLLINGBERY, L. A.; HULL, T. R. The Thermal Decomposition of Huntite and hydromagnesite: a review. **Thermochimica Acta**, Amsterdam, v. 509, n. 1–2, p. 1–11, Sept. 2010a.
- HOLLINGBERY, L. A.; HULL, T. R. The Fire retardant behaviour of huntite and hydromagnesite – a review. **Polymer Degradation and Stability**, London, v. 95, n. 12, p. 2213–2225, Dec. 2010b.
- HOLLINGBERY, L. A.; HULL, T. R. The Thermal decomposition of natural mixtures of huntite and hydromagnesite. **Thermochimica Acta**, Amsterdam, v. 528, p. 45–52, Jan. 2012.
- IKAI, S. et al. Asbestos-free technology with new high toughness polypropylene (PP) fibers in air-cured Hatschek process. **Construction and Building Materials**, Amsterdam, v. 24, n. 2, p. 171–180, Feb. 2010.
- JARABO, R. et al. Effect of sepiolite on the flocculation of suspensions of fibre-reinforced cement. **Cement and Concrete Research**, Kidlington, v. 40, n. 10, p. 1524–1530, Oct. 2010.
- JARABO, R. et al. Effect of sepiolite on mechanical and physical properties of fiber cement. **ACI Materials Journal**, v. 111, n. 4, p. 355-362, Aug. 2014.
- JIANGXIONG, W.; YIMIN, C.; YONGXIN, L. The reaction mechanism between MgO and microsilica at room temperature. **Journal of Wuhan University of Technology-Material Science**, Wuhan, v. 21, p. 88–91, June. 2006.

- JIN, F.; AL-TABBAA, A. Strength and hydration products of reactive MgO–silica pastes. **Cement and Concrete Composites**, Kidlington, v. 52, p. 27–33, Sept. 2014.
- JOHN, V. M. et al. Durability of slag mortar reinforced with coconut fibre. **Cement and Concrete Composites**, Kidlington, v. 27, n. 5, p. 565–574, May. 2005.
- KAMATH, P. V.; ANNAL THERESE, G. H.; GOPALAKRISHNAN, J. On the existence of hydrotalcite-like phases in the absence of trivalent cations. **Journal of Solid State Chemistry**, Maryland Heights, v. 128, n. 1, p. 38–41, Jan. 1997.
- KANG, H. J.; SONG, M. S.; KIM, Y. S. The Effects of sepiolite on the properties of portland cement mortar. **Journal of the Korean Ceramic Society**, Seoul, v. 45, n. 8, p. 443–452, 31 Aug. 2008.
- KAVAS, T.; SABAH, E.; ÇELIK, M. S. Structural properties of sepiolite-reinforced cement composite. **Cement and Concrete Research**, Kidlington, v. 34, n. 11, p. 2135–2139, Nov. 2004.
- KHORAMI, M.; GANJIAN, E.; SRIVASTAV, A. Feasibility study on production of fiber cement board using waste kraft pulp in corporation with polypropylene and acrylic fibers. **Materials Today: Proceedings**, Amsterdam, v. 3, n. 2, p. 376–380, 2016.
- KLEIN, F.; GARRIDO, C. J. Thermodynamic constraints on mineral carbonation of serpentinized peridotite. **Lithos**, Amsterdam, v. 126, n. 3–4, p. 147–160, Oct. 2011.
- KLEIN, F.; MCCOLLOM, T. M. From Serpentinization to carbonation: new insights from a CO₂ injection experiment. **Earth and Planetary Science Letters**, Amsterdam, v. 379, p. 137–145, Oct. 2013.
- KRYSZTAFKIEWICZ, A. et al. Amorphous magnesium silicate - synthesis, physicochemical properties and surface morphology. **Advanced Powder Technology**, Amsterdam, v. 15, n. 5, p. 549–565, 2004.
- KUMAR, R.; BHATTACHARJEE, B. Porosity, pore size distribution and in situ strength of concrete. **Cement and Concrete Research**, Kidlington, v. 33, n. 1, p. 155–164, Jan. 2003.
- LACKNER, K. S. et al. Carbon dioxide disposal in carbonate minerals. **Energy**, London, v. 20, n. 11, p. 1153–1170, 1995.
- LANAS, J.; ALVAREZ, J. I. Dolomitic lime: thermal decomposition of nesquehonite. **Thermochimica Acta**, Amsterdam, v. 421, n. 1–2, p. 123–132, Nov. 2004.
- LANGFORD, J. I.; WILSON, A. J. C. Scherrer after sixty years: a survey and some new results in the determination of crystallite size. **Journal of Applied Crystallography**, Chichester, v. 11, n. 2, p. 102–113, Apr. 1978.
- LEA, F. M.; HEWLETT, P. C. **Lea's chemistry of cement and concrete**. Oxford: Elsevier, 2004.
- LI, Q. et al. Fabrication of light-emitting porous hydromagnesite with rosette-like architecture. **Solid State Communications**, Kidlington, v. 125, n. 2, p. 117–120, Jan. 2003.

- LI, Z. et al. Characterization of reaction products and reaction process of MgO–SiO₂–H₂O system at room temperature. **Construction and Building Materials**, Amsterdam, v. 61, p. 252–259, June. 2014.
- LIAO, J.; SENNA, M. Mechanochemical dehydration and amorphization of hydroxides of Ca, Mg and Al on grinding with and without SiO₂. **Solid State Ionics**, Amsterdam, v. 66, n. 3–4, p. 313–319, Nov. 1993.
- LING, Z. et al. Exploring crystalline-structural variations of cellulose during alkaline pretreatment for enhanced enzymatic hydrolysis. **Bioresource Technology**, Amsterdam, v. 224, p. 611–617, Jan. 2017.
- LISKA, M.; AL-TABBAA, A. Ultra-green construction: reactive magnesia masonry products. **Proceedings of the Institution of Civil Engineers - Waste and Resource Management**, London, v. 162, n. 4, p. 185–196, Nov. 2009.
- LOTHENBACH, B. et al. Magnesium and calcium silicate hydrates. **Cement and Concrete Research**, Kidlington, v. 77, p. 60–68, Nov. 2015.
- MADANDOUST, R. et al. Assessment of factors influencing mechanical properties of steel fiber reinforced self-compacting concrete. **Materials & Design**, London, v. 83, p. 284–294, Oct. 2015.
- MÁRMOL, G. et al. Mechanical and physical performance of low alkalinity cementitious composites reinforced with recycled cellulosic fibres pulp from cement kraft bags. **Industrial Crops and Products**, Amsterdam, v. 49, p. 422–427, Aug. 2013.
- MÁRMOL, G.; SAVASTANO, H. Study of the degradation of non-conventional MgO–SiO₂ cement reinforced with lignocellulosic fibers. **Cement and Concrete Composites**, Kidlington, v. 80, p. 258–267, Mar. 2017.
- MÁRMOL, G. et al. Optimization of the MgOSiO₂ binding system for fiber-cement production with cellulosic reinforcing elements. **Materials & Design**, London, v. 105, p. 251–261, Sept. 2016.
- MARTIN, A. R. et al. Studies on the thermal properties of sisal fiber and its constituents. **Thermochimica Acta**, Amsterdam, v. 506, n. 1–2, p. 14–19, July. 2010.
- MEHTA, P. K.; MONTEIRO, P. J. M. **Concrete: microstructure, properties, and materials**. 3rd ed. New York: McGraw-Hill, 2006.
- MELO FILHO, J. de A.; SILVA, F. de A.; TOLEDO FILHO, R. D. Degradation kinetics and aging mechanisms on sisal fiber cement composite systems. **Cement and Concrete Composites**, Kidlington, v. 40, p. 30–39, July. 2013.
- MO, L.; ZHANG, F.; DENG, M. Effects of carbonation treatment on the properties of hydrated fly Ash–MgO–portland cement blends. **Construction and Building Materials**, Amsterdam, v. 96, p. 147–154, Oct. 2015.

MOHR, B. J.; BIERNACKI, J. J.; KURTIS, K. E. Microstructural and chemical effects of wet/dry cycling on pulp fiber–cement composites. **Cement and Concrete Research**, Kidlington, v. 36, n. 7, p. 1240–1251, July. 2006.

MOHR, B. J.; BIERNACKI, J. J.; KURTIS, K. E. Supplementary Cementitious materials for mitigating degradation of kraft pulp fiber–cement composites. **Cement and Concrete Research**, Kidlington, v. 37, n. 11, p. 1531–1543, Nov. 2007.

MOHR, B. J.; NANKO, H.; KURTIS, K. E. Durability of kraft pulp fiber–cement composites to wet/dry cycling. **Cement and Concrete Composites**, Kidlington, v. 27, n. 4, p. 435–448, Apr. 2005.

MORANDEAU, A.; THIÉRY, M.; DANGLA, P. Impact of accelerated carbonation on OPC cement paste blended with fly ash. **Cement and Concrete Research**, Kidlington, v. 67, p. 226–236, Jan. 2015.

NÄGELE, E.; SCHNEIDER, U. From cement to hardened paste: an elektrokinetic study. **Cement and Concrete Research**, Kidlington, v. 19, n. 6, p. 978–986, Nov. 1989.

NDUAGU, E. et al. Production of magnesium hydroxide from magnesium silicate for the purpose of CO₂ mineralization – part 2: Mg extraction modeling and application to different mg silicate rocks. **Minerals Engineering**, Kidlington, v. 30, p. 87–94, Apr. 2012.

NOGUCHI, T. et al. A practical equation for elastic modulus of concrete. **ACI Structural Journal**, Farmington Hills, v. 106, n. 5, p. 690–696, 2009.

OCHI, S. Mechanical properties of kenaf fibers and kenaf/PLA composites. **Mechanics of Materials**, Amsterdam, v. 40, n. 4–5, p. 446–452, Apr. 2008.

OKSMAN, K.; SKRIFVARS, M.; SELIN, J. F. Natural fibres as reinforcement in polylactic acid (PLA) composites. **Composites Science and Technology**, Kidlington, v. 63, n. 9, p. 1317–1324, July. 2003.

ONUAGULUCHI, O.; BANTHIA, N. Plant-based natural fibre reinforced cement composites: a review. **Cement and Concrete Composites**, Kidlington, v. 68, p. 96–108, Apr. 2016.

OUAJAI, S.; SHANKS, R. A. Composition, structure and thermal degradation of hemp cellulose after chemical treatments. **Polymer Degradation and Stability**, London, v. 89, n. 2, p. 327–335, Aug. 2005.

OZTURK, A. U.; BARADAN, B. A Comparison study of porosity and compressive strength mathematical models with image analysis. **Computational Materials Science**, Amsterdam, v. 43, n. 4, p. 974–979, Oct. 2008.

PARK, S. et al. Cellulose crystallinity index: measurement techniques and their impact on interpreting cellulase performance. **Biotechnology for Biofuels**, London, v. 3, n. 1, art. 10, 2010.

PĂRPĂRIȚĂ, E. et al. TG/FT–IR/MS Study on thermal decomposition of polypropylene/biomass composites. **Polymer Degradation and Stability**, London, v. 109, p. 13–20, Nov. 2014.

- PEREIRA, C. L. et al. Use of highly reactive rice husk ash in the production of cement matrix reinforced with green coconut fiber. **Industrial Crops and Products**, Amsterdam, v. 49, p. 88–96, Aug. 2013.
- PIZZOL, V. D. et al. Mineralogical and microstructural changes promoted by accelerated carbonation and ageing cycles of hybrid fiber–cement composites. **Construction and Building Materials**, Amsterdam, v. 68, p. 750–756, Oct. 2014.
- PURNELL, P. et al. Super-critical carbonation of glass-fibre reinforced cement. Part 2: microstructural observations. **Composites Part A: Applied Science and Manufacturing**, Kidlington, v. 34, n. 11, p. 1105–1112, Nov. 2003.
- PURNELL, P.; SHORT, N.; PAGE, C. Super-critical carbonation of glass-fibre reinforced cement. Part 1: mechanical testing and chemical analysis. **Composites Part A: Applied Science and Manufacturing**, Kidlington, v. 32, n. 12, p. 1777–1787, Dec. 2001.
- RAMACHANDRAN, V. S. (Ed.). **Handbook of thermal analysis of construction materials**. Norwich: Noyes Publications, 2003.
- RASHID, I. et al. Characterization of chitin-metal silicates as binding superdisintegrants. **Journal of Pharmaceutical Sciences**, New York, v. 98, n. 12, p. 4887–4901, Dec. 2009.
- RODRIGUEZ-NAVARRO, C. et al. Thermal decomposition of calcite: mechanisms of formation and textural evolution of CaO nanocrystals. **American Mineralogist**, Chantilly, v. 94, n. 4, p. 578–593, 1 Apr. 2009.
- ROOSZ, C. et al. Crystal structure of magnesium silicate hydrates (M-S-H): the relation with 2:1 Mg–Si phyllosilicates. **Cement and Concrete Research**, Kidlington, v. 73, p. 228–237, July. 2015.
- ROSTAMI, V. et al. Microstructure of cement paste subject to early carbonation curing. **Cement and Concrete Research**, Kidlington, v. 42, n. 1, p. 186–193, Jan. 2012.
- ROY, D.; ARJUNAN, P.; SILSBEE, M. Effect of silica fume, metakaolin, and low-calcium fly ash on chemical resistance of concrete. **Cement and Concrete Research**, Kidlington, v. 31, n. 12, p. 1809–1813, Dec. 2001.
- RUIZ, R. et al. Reversible folding in sepiolite: study by thermal and textural analysis. **Thermochemica Acta**, Amsterdam, v. 279, p. 103–110, June. 1996.
- SANDBERG, B.; MOSBERG, T. **Ceramic transactions: advances in refractories technology**. Westerville, Ohio: American Ceramic Society, 1989.
- SANTOS, S. F. et al. Potential Use of colloidal silica in cement based composites: evaluation of the mechanical properties. **Key Engineering Materials**, v. 517, p. 382–391, June. 2012.
- SANTOS, S. F. et al. Supercritical carbonation treatment on extruded fibre–cement reinforced with vegetable fibres. **Cement and Concrete Composites**, Kidlington v. 56, p. 84–94, Feb. 2015a.

- SANTOS, S. F. et al. Compuestos cementantes no convencionales reforzados con fibras vegetales: Una revisión de estrategias para mejorar la durabilidad. **Materiales de Construcción**, Madrid, v. 65, n. 317, p. e041, Mar. 2015b.
- SAVASTANO, H.; WARDEN, P. G.; COUTTS, R. S. P. Microstructure and mechanical properties of waste fibre–cement composites. **Cement and Concrete Composites**, Kidlington v. 27, n. 5, p. 583–592, May. 2005.
- SAVASTANO JR., H.; SANTOS, S. F.; AGOPYAN, V. 3-Sustainability of vegetable fibres in construction. In: KHATIB, J. M. (Ed.). **Sustainability of construction materials**. Cambridge: Woodhead Publishing, 2009. p. 55–81.
- SAVASTANO JR., H.; WARDEN, P.; COUTTS, R. S. Brazilian waste fibres as reinforcement for cement-based composites. **Cement and Concrete Composites**, Kidlington, v. 22, n. 5, p. 379–384, Oct. 2000.
- SAVASTANO JR, H.; WARDEN, P.; COUTTS, R. S. Potential of alternative fibre cements as building materials for developing areas. **Cement and Concrete Composites**, Kidlington, v. 25, n. 6, p. 585–592, Aug. 2003.
- SEGAL, L. et al. An empirical method for estimating the degree of crystallinity of native cellulose using the X-Ray diffractometer. **Textile Research Journal**, London, v. 29, n. 10, p. 786–794, Oct. 1959.
- SENARATNE, S. et al. The costs and benefits of combining recycled aggregate with steel fibres as a sustainable, structural material. **Journal of Cleaner Production**, Amsterdam, v. 112, p. 2318–2327, Jan. 2016.
- SHAFIZADEH, F.; BRADBURY, A. G. W. Thermal degradation of cellulose in air and nitrogen at low temperatures. **Journal of Applied Polymer Science**, Hoboken, v. 23, n. 5, p. 1431–1442, Mar. 1979.
- SHAND, M. A. **The chemistry and technology of magnesia**. Hoboken: Wiley-Interscience, 2006.
- SHEN, D. et al. TG-MS Analysis for thermal decomposition of cellulose under different atmospheres. **Carbohydrate Polymers**, Kidlington, v. 98, n. 1, p. 514–521, Oct. 2013.
- SHU, X. et al. Hybrid effects of carbon fibers on mechanical properties of portland cement mortar. **Materials & Design**, London, v. 65, p. 1222–1228, Jan. 2015.
- SHUALI, U. Thermal Analysis of Sepiolite and Palygorskite Treated with Butylamine. **Clay Minerals**, v. 25, n. 1, p. 107–119, 1990.
- SILVA, F. de A.; MOBASHER, B.; TOLEDO FILHO, R. D. Cracking mechanisms in durable sisal fiber reinforced cement composites. **Cement and Concrete Composites**, Kidlington, v. 31, n. 10, p. 721–730, Nov. 2009.
- SINGH, S. M. Alkali resistance of some vegetable fibers and their adhesion with portland cement. **Research and Industry**, New Delhi, v. 15, p. 121–126, 1985.

- SUMMERSCALES, J. et al. A review of bast fibres and their composites. Part 1 – fibres as reinforcements. **Composites Part A: Applied Science and Manufacturing**, Kidlington, v. 41, n. 10, p. 1329–1335, Oct. 2010.
- SUTRADHAR, N. et al. Controlled synthesis of different morphologies of MgO and their use as solid base catalysts. **The Journal of Physical Chemistry C**, Washington, v. 115, n. 25, p. 12308–12316, June. 2011.
- SZCZERBA, J. et al. Influence of time and temperature on ageing and phases synthesis in the MgO–SiO₂–H₂O system. **Thermochimica Acta**, Amsterdam, v. 567, p. 57–64, Sept. 2013.
- TAYLOR, H. F. W. **Cement chemistry**. 2nd ed. London: T. Telford, 1997.
- TEMUUJIN, J.; OKADA, K.; MACKENZIE, K. J. D. Role of water in the mechanochemical reactions of MgO–SiO₂ systems. **Journal of Solid State Chemistry**, Maryland Heights, v. 138, n. 1, p. 169–177, June. 1998.
- TEMUUJIN, J.; OKADA, K.; MACKENZIE, K. J. D. Formation of layered magnesium silicate during the aging of magnesium hydroxide-silica mixtures. **Journal of the American Ceramic Society**, Malden, v. 81, n. 3, p. 754–756, Jan. 2005.
- THOMAS, J. J.; MUSSO, S.; PRESTINI, I. Kinetics and activation energy of magnesium oxide hydration. **Journal of the American Ceramic Society**, Malden, v. 97, n. 1, p. 275–282, Jan. 2014.
- TOLEDO FILHO, R. D. et al. Durability of alkali-sensitive sisal and coconut fibres in cement mortar composites. **Cement and Concrete Composites**, Kidlington, v. 22, n. 2, p. 127–143, Apr. 2000.
- TOLEDO FILHO, R. D. et al. Durability of compression molded sisal fiber reinforced mortar laminates. **Construction and Building Materials**, Amsterdam, v. 23, n. 6, p. 2409–2420, June. 2009.
- TONOLI, G. H. D. **Fibras curtas de eucalipto para novas tecnologias em fibrocimento**. 2010. 128 f. Tese (Doutorado) - Interunidades em Ciência e Engenharia de Materiais, Universidade de São Paulo, São Carlos, Brazil, 2010.
- TONOLI, G. H. D. et al. Impact of bleaching pine fibre on the fibre/cement interface. **Journal of Materials Science**, New York, v. 47, n. 9, p. 4167–4177, May. 2012.
- TONOLI, G. H. D. et al. Processing and dimensional changes of cement based composites reinforced with surface-treated cellulose fibres. **Cement and Concrete Composites**, Kidlington, v. 37, p. 68–75, Mar. 2013.
- TONOLI, G. H. D. et al. Effect of fibre morphology on flocculation of fibre–cement suspensions. **Cement and Concrete Research**, Kidlington, v. 39, n. 11, p. 1017–1022, Nov. 2009a.
- TONOLI, G. H. D. et al. Cellulose modified fibres in cement based composites. **Composites Part A: Applied Science and Manufacturing**, v. 40, n. 12, p. 2046–2053, Dec. 2009b.
- TONOLI, G. H. D. et al. Eucalyptus pulp fibres as alternative reinforcement to engineered cement-based composites. **Industrial Crops and Products**, Amsterdam, v. 31, n. 2, p. 225–232, Mar. 2010.

UNLUER, C.; AL-TABBAA, A. Impact of hydrated magnesium carbonate additives on the carbonation of reactive MgO cements. **Cement and Concrete Research**, Kidlington, v. 54, p. 87–97, Dec. 2013.

UNLUER, C.; AL-TABBAA, A. Enhancing the carbonation of MgO cement porous blocks through improved curing conditions. **Cement and Concrete Research**, Kidlington, v. 59, p. 55–65, May. 2014.

UNLUER, C.; AL-TABBAA, A. The role of brucite, ground granulated blastfurnace slag, and magnesium silicates in the carbonation and performance of MgO cements. **Construction and Building Materials**, Amsterdam, v. 94, p. 629–643, Sept. 2015.

UNLUER, C.; AL-TABBAA, A. Reply to the discussion of the papers “impact of hydrated magnesium carbonate additives on the carbonation of reactive mgo cements” and “enhancing the carbonation of MgO cement porous blocks through improved curing conditions”, by S.A. Walling and J.L. Provis. **Cement and Concrete Research**, Kidlington, v. 79, p. 427–430, Jan. 2016.

VÁGVÖLGYI, V. et al. Controlled rate thermal analysis of hydromagnesite. **Journal of Thermal Analysis and Calorimetry**, Budapest, v. 92, n. 3, p. 893–897, 2008.

VANDEPERRE, L. J.; AL-TABBAA, A. Accelerated carbonation of reactive MgO cements. **Advances in Cement Research**, London, v. 19, n. 2, p. 67–79, Apr. 2007.

VLASOPOULOS, N.; BERNEBEU, J. P. **Production of magnesium carbonate**. [s.l.]: Google Patents, 2014.

WALLING, S. A. et al. Structure and properties of binder gels formed in the system $\text{Mg}(\text{OH})_2 - \text{SiO}_2 - \text{H}_2\text{O}$ for immobilisation of magnox sludge. **Dalton Transactions**, v. 44, n. 17, p. 8126–8137, 2015.

WALLING, S. A.; PROVIS, J. L. A Discussion of the papers “Impact of hydrated magnesium carbonate additives on the carbonation of reactive MgO cements” and “Enhancing the carbonation of MgO cement porous blocks through improved curing conditions”, by C. Unluer & A. Al-Tabbaa. **Cement and Concrete Research**, Kidlington, v. 79, p. 424–426, Jan. 2016.

WANG, X. et al. Controllable fabrication of high purity $\text{Mg}(\text{OH})_2$ nanoneedles via direct transformation of natural brucite. **Materials Letters**, Amsterdam, v. 120, p. 69–72, Apr. 2014.

WEDEPHOL, K. H. **Handbook of geochemistry 1. 1**. Berlin; Heidelberg: Springer, 1969. v. 1

WEI, J.; MEYER, C. Improving degradation resistance of sisal fiber in concrete through fiber surface treatment. **Applied Surface Science**, Amsterdam, v. 289, p. 511–523, Enero. 2014.

WONG, H. S.; ABDUL RAZAK, H. Efficiency of calcined kaolin and silica fume as cement replacement material for strength performance. **Cement and Concrete Research**, Kidlington, v. 35, n. 4, p. 696–702, Apr. 2005.

YANG, H. et al. Characteristics of hemicellulose, cellulose and lignin pyrolysis. **Fuel**, Houston, v. 86, n. 12–13, p. 1781–1788, Aug. 2007.

ZELIĆ, J. et al. The Role of silica fume in the kinetics and mechanisms during the early stage of cement hydration. **Cement and Concrete Research**, Kidlington, v. 30, n. 10, p. 1655–1662, Oct. 2000.

ZHA, X. et al. Numerical modeling of supercritical carbonation process in cement-based materials. **Cement and Concrete Research**, Kidlington, v. 72, p. 10–20, June. 2015.

ZHANG, T.; CHEESEMAN, C. R.; VANDEPERRE, L. J. Development of low pH cement systems forming magnesium silicate hydrate (M-S-H). **Cement and Concrete Research**, Kidlington, v. 41, n. 4, p. 439–442, April 2011.

ZHANG, T.; VANDEPERRE, L. J.; CHEESEMAN, C. R. Formation of magnesium silicate hydrate (M-S-H) cement pastes using sodium hexametaphosphate. **Cement and Concrete Research**, Kidlington, v. 65, p. 8–14, Nov. 2014.

ZHOU, F.; CHENG, G.; JIANG, B. Effect of silane treatment on microstructure of sisal fibers. **Applied Surface Science**, Amsterdam, v. 292, p. 806–812, Feb. 2014.